NORTHWESTERN UNIVERSITY

Excitons, Photons, and Plasmons in Novel Material Structures

A DISSERTATION

SUBMITTED TO THE GRADUATE SCHOOL
IN PARTIAL FULFILLMENT OF THE REQUIREMENTS

for the degree

DOCTOR OF PHILOSOPHY

Field of Materials Science and Engineering

By

Mark A. Anderson

EVANSTON, ILLINOIS

December 2008

ABSTRACT

Excitons, Photons, and Plasmons in Novel Material Structures

Mark A. Anderson

Characterizing the interaction of light and matter has become increasingly important in recent decades, as devices scale down, data transfer speeds up, and the use of photon-based technology (photonics and optoelectronics) becomes widespread. Copper chloride (CuCl) thin films and zinc oxide (ZnO) inverse opal photonic crystals are the two material systems investigated herein, and they interact with light in very different ways.

CuCl is a nonlinear optical material with unique excitonic properties. CuCl thin films were fabricated by thermal evaporation and characterized by low temperature photoluminescence (PL) and angle-dependent second harmonic generation. Angle-dependent PL from CuCl films under resonant two-photon excitation revealed that the generated excitonic molecules have an angular dispersion along the laser direction, implying the creation of bipolaritons rather than biexcitons. A broad non-resonant two-photon excitation regime was discovered in CuCl pellets, but not for films. This regime is likely caused by the presence of surface and bulk defects that create an intermediate state for exciton generation. Measurements of second harmonic generation (SHG) from CuCl films revealed the strength of the SHG response is highly dependent on the stress, orientation, and quality of the growing films. The value of the second order nonlinear coefficient (d_{14}) was determined for a CuCl thin film and found to be lower than the bulk values.

Photonic crystals are metamaterials with periodic variations in the refractive index. The spacing and dimensions of the variations control how light interacts with the structure. Zinc oxide (ZnO) inverse-opal photonic-crystals with high filling-fraction and directional photonic pseudo-gaps in the visible

spectrum were fabricated. The effects of fabrication on optical quality were quantified via PL and reflectivity measurements. Angle- and polarization-dependent reflection and PL revealed strong enhancement of spontaneous emission from ZnO due to modification of the density of states by high-order photonic bands (frozen modes). Quantum dots were embedded into the inverse opals to examine how the frozen mode affected their emission. Similar enhancement was not seen, likely due to their position in the inverse opal and variations in the local density of states. Metal nanoparticles infiltrated into the inverse opals created a structure exhibiting both photonic and plasmonic responses. This preliminary work will bring about new and exciting results for inverse opal photonic crystals.

ACKNOWLEDGMENTS

I would like to express my gratitude to the many people here at Northwestern and elsewhere who have made this endeavor possible. Such an undertaking could never have been made alone. I would like to thank my advisor, Prof. R.P.H. Chang, for his support, guidance, and wisdom in science and life. I would also like to thank my committee, Prof. Scott Barnett, Prof. Michael Bedzyk, and Prof. John Ketterson for their valuable insight and support.

I would like to acknowledge the past and present members of the Chang Group with whom I have had the pleasure of working. Many thanks for making my time at the core of the volcano so very fun and exciting. I'd especially like to thank Haitao Zhang for teaching me to survive in the lab as I first joined the group, Michael Scharrer for guidance with the inverse opal project, Larry Aagesen for insightful discussions, a working ALD, and camaraderie, Anne Muller for helping out more times than I can recall, and Bruce Buchholz for teaching me a little something about everything.

I was fortunate to collaborate with two great physics research groups throughout the course of my research. I would like to thank Prof. John Ketterson, Byron Watkins, and Joon Jang for their contributions, guidance, and spirited discussions on the CuCl project. Also, many thanks go to Prof. Hui Cao and Heeso Noh for their insight, contributions, and enthusiasm on the inverse opal project. All were extremely generous with their time and facilities and exhibited remarkable patience when teaching this materials scientist about the wonderful world of physics.

My deepest thanks go to my friends and family for the love, support, and the occasional distractions from science that we all occasionally require. I am eternally grateful to Chris Booth-Morrison and Agatha Poraj-Kozminski for opening their home and making me welcome when I was the least tolerable. Thanks to my parents, Dave and Nancy, and my sister, Kelly, for their endless supply of love and support. Most of all I'd like to thank my wife, Deirdre, for taking this journey with me and always being there with endless love, patience, and encouragement.

TABLE OF CONTENTS

LIST OF FIGURES

LIST OF TABLES

INTRODUCTION

This thesis focuses on two specific material systems, (1) thin films of copper chloride and (2) zinc oxide inverse opal photonic crystals, which exhibit different interactions with light. Copper chloride (CuCl) is a wide band gap semiconductor that has been studied extensively due to its high exciton binding energy. CuCl is a system where light interacts directly with a material to create an excited state, in this case an electron-hole pair (exciton). Excitons (and biexcitons) in CuCl have long presented a model case for many interesting phenomena, including optical switching,[1] Bose-Einstein condensation,[2] superconducting,[3] and biexciton lasing.[4] In this work, CuCl thin films are examined as follows:

- Section I describes the background of CuCl, including the evolution of excitons and biexcitons and nonlinear optical properties. A review of CuCl thin film growth is included.
- Section 2 examines the fabrication of high quality CuCl thin films on several substrates. A discussion of the optical characterization techniques, including low temperature photoluminescence (PL) and second harmonic generation (SHG), are provided.
- Section 3 describes the results of the CuCl fabrication process, and the photoluminescence studies of propagating bipolaritons and non-resonant two-photon excitation. An analysis of SHG to determine the second order nonlinear optical coefficient in CuCl films is also presented.

ZnO inverse opal photonic crystals are the second material system studied herein. In recent years, the development of photonic crystal structures has allowed researchers to harness and control the flow of light. Photonic crystals are periodic dielectric structures that exhibit a photonic band gap, a range of frequencies that are forbidden to travel through the structure. Unlike CuCl films, the optical properties of ZnO photonic crystals are primarily determined by the structure. The level of dielectric contrast determines the position and strength of a photonic band gap. Photonic crystals can be found in all three dimensions and have a wide variety of potential applications including waveguides,[5] laser cavities,[6] solar

cells,[7] and sensors.[8] Three dimensional photonic crystals for use in the visible region have recently attracted much interest. Fabrication of these structures has proven to be especially challenging, as the required size scale of a photonic crystal is determined by its wavelength of operation. The fabrication and characterization of ZnO inverse opal photonic crystals is examined as follows:

- Section 4 covers the background, the theory of diffraction, and the band structure development of photonic crystals. Fabrication techniques for 3D photonic crystals, especially colloidal crystal-based photonic crystals, are described. Inverse opal fabrication by atomic layer deposition (ALD) is described.
- Section 5 details the methods used to fabricate ZnO inverse opals from colloidal crystal templates. Low temperature ALD of ZnO for infiltration is discussed. Techniques for infiltrating quantum dots (QDs) and metallic nanoparticles (NPs) into ZnO inverse opals are presented.
- Section 6 presents the results of ZnO inverse opal fabrication and the effects of processing parameters, such as firing and reactive ion etching, on the basic optical properties (reflectivity and PL). The impact of processing on ZnO PL is also examined.
- Section 6 continues with results of angle- and polarization-dependent reflectivity and PL measurements. Enhanced PL is observed, due to the modified density of states at a stationary inflection point. This treatment is also applied to QD-infiltrated ZnO inverse opals. Metallic NP-infiltrated ZnO inverse opals are examined, and the combined plasmonic-photonic response is shown.

Section 1: Copper Chloride Overview

1.1 Introduction

Copper (I) chloride (CuCl) has captured the interest of scientists for over a century. The optical properties of CuCl were first utilized in various photosensitive film applications[9] and in the 1960's scientists started probing its structure on the quantum level with low temperature optical absorption spectra.[10] The next fifty years saw a dramatic increase of study into the fundamental properties of CuCl via an astonishing variety of techniques. Ideas for applications included photocatalysts,[11] superconductors,[3] optical switches,[1] photonic crystals,[12] UV light emitting diodes,[13] Bose-Einstein condensation,[2] and quantum computing.[14]

Copper chloride is a nonlinear optical material possessing a unique exciton structure. Excitons have long been used as a diagnostic tool for semiconductors[15] and as a system of study for fundamental physical phenomena.[16] The nonlinear optical response of semiconductors is also a rich, long-established field of study. Indeed, the accomplishments of this field are widespread – seen today in the form of solid state lasers, detectors, and optical communications. A new wave in nonlinear optics focuses on developing the small and the quick: nanoscale, ultra-fast optical circuits for switching, modulation, quantum communications, and quantum computing.[17] This heralds a change in the standard sample for optical study, the bulk single crystal. These applications require a nanostructured material that is high quality and easily integrated with other optical or electrical components for an optoelectronic equivalent of lab-on-a-chip.

1.2 Properties of Copper Chloride

CuCl is an ionic solid ($f_i = 0.746$) containing Frenkel cation pairs (Cu_i^* and V'_{Cu}) in which interstitial copper ions exhibit the highest mobility.[18] Ionic conductivity remains the dominant transport mechanism up to 390 ^oC, approximately three orders of magnitude larger ($\sigma_i \sim 3.3x10^{-8}\ \Omega^{-1}cm^{-1}$)[18] than the p-type hole conductivity ($\sigma_h \sim 1x10^{-11}\ \Omega^{-1}cm^{-1}$)[19]. CuCl has been referred to as the "ideal gas of the solid electrolytes"

due to its low defect concentration and therefore low interaction and degree of trapping.[11] CuCl crystallizes in the cubic zincblende (γ-CuCl) structure up to 407 °C. Figure 1.1 is a schematic of the γ-CuCl unit cell, with a lattice parameter of a = 5.406 Å.

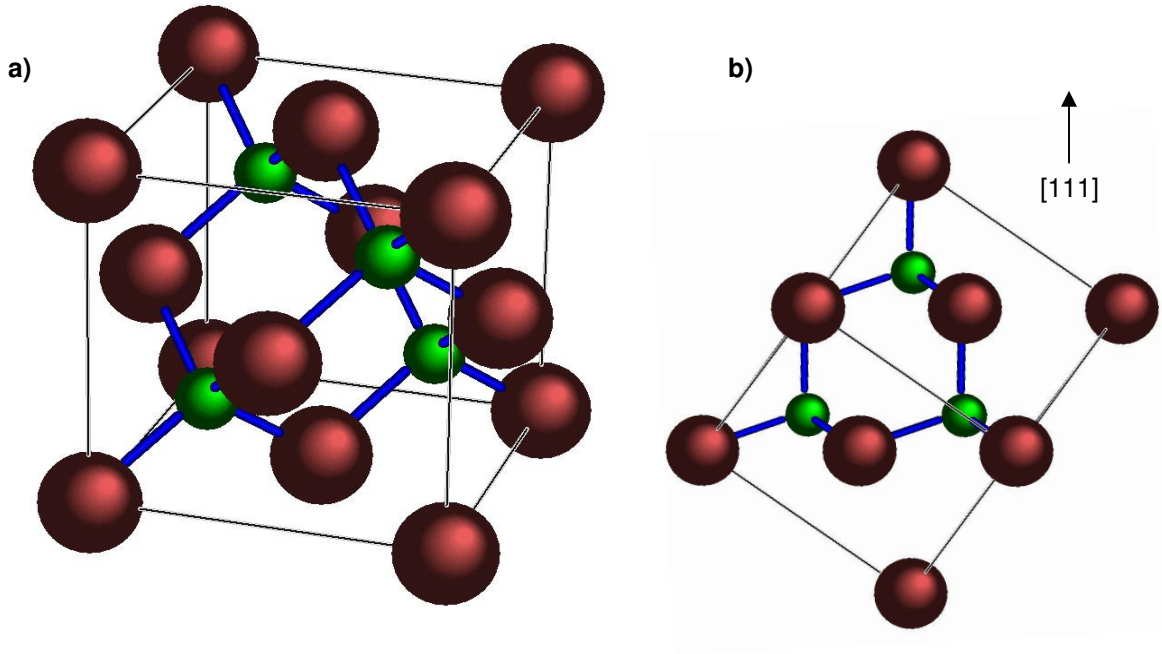

Figure 1.1: a) Schematic of a CuCl unit cell. Cu atoms are located at fcc positions (red) and Cl atoms at ¼,¼,¼ positions (green). b) View of alternating stacking of Cu and Cl atoms along the [111] direction.

At 407 °C, there is phase transition to a wurtzite structure (β-CuCl) before reaching the melting point at 422 °C. β-CuCl is a superionic conducting phase (σ_i ~ 0.1 $\Omega^{-1}cm^{-1}$).[20] At higher pressures there is a bcc structure, as well as several other high-pressure (>50 kbar) phases.[21] These were the focus of much debate as several anomalous properties such as a transition to a high-T_c superconducting state,[22,23] and an unexpected diamagnetic transition[24] have been attributed to these phases.

The case for superconductivity in CuCl has been debated since the late 1970's. The Si/CuCl system proved to be of particular interest.[25] Initial theories described this phenomenon in terms of electron-hole pairs generated at a narrow energy gap formed by pressure or metallic Cu precipitates; however, experiments later proved them to be erroneous.[26] Another theory suggested a piezoelectric

mechanism, again for Cu precipitates, but was never conclusively proven.[3] In recent years, Rhim *et al.* have studied the nature of interfaces in Si/CuCl superlattices and have proposed a mechanism for 2D metallicity and potential superconductivity at the CuCl/Si interface that depends on the bonding and structure of the first several layers of atoms.[27]

CuCl is a wide band gap semiconductor with four valence electrons per atom. Other members of this family include Group IV elemental, III-V, and II-VI semiconductors. CuCl has a dipole-allowed direct gap of 3.43 eV that *increases* with increasing temperature.[28] The unique band structure of CuCl has been developed through a combination of theory and experimentation.[28-33] In most tetrahedrally coordinated semiconductors the conduction and valence bands form from sp^3 hybridization of the atomic states.[28] CuCl is a notable exception. Copper 3*d* levels and chlorine *p*-levels occur at similar energies, leading to *p-d* hybridization that significantly affects the structure.[34] One consequence is that spin-orbit coupling in CuCl is reversed when compared to other zincblende semiconductors. The *d*-states contribute a negative spin-orbit term causing the valence bands to be flipped; the two-fold degenerate Γ_7 states are higher energy than the four-fold degenerate Γ_8 states.[35] Figure 1.2 shows how crystal structure and spin-orbit coupling affect the CuCl band structure. In Figure 1.2d, E_g is the direct band gap (3.43 eV), Δ_{so} is the split-off band energy (~60 meV), and $E_{\Gamma X}$ a small indirect band gap (0.41 eV) that have been found experimentally.[36] Of most interest in CuCl are the excitons that come from exciting an electron from the Γ_7 valence band up to the Γ_6 conduction band.

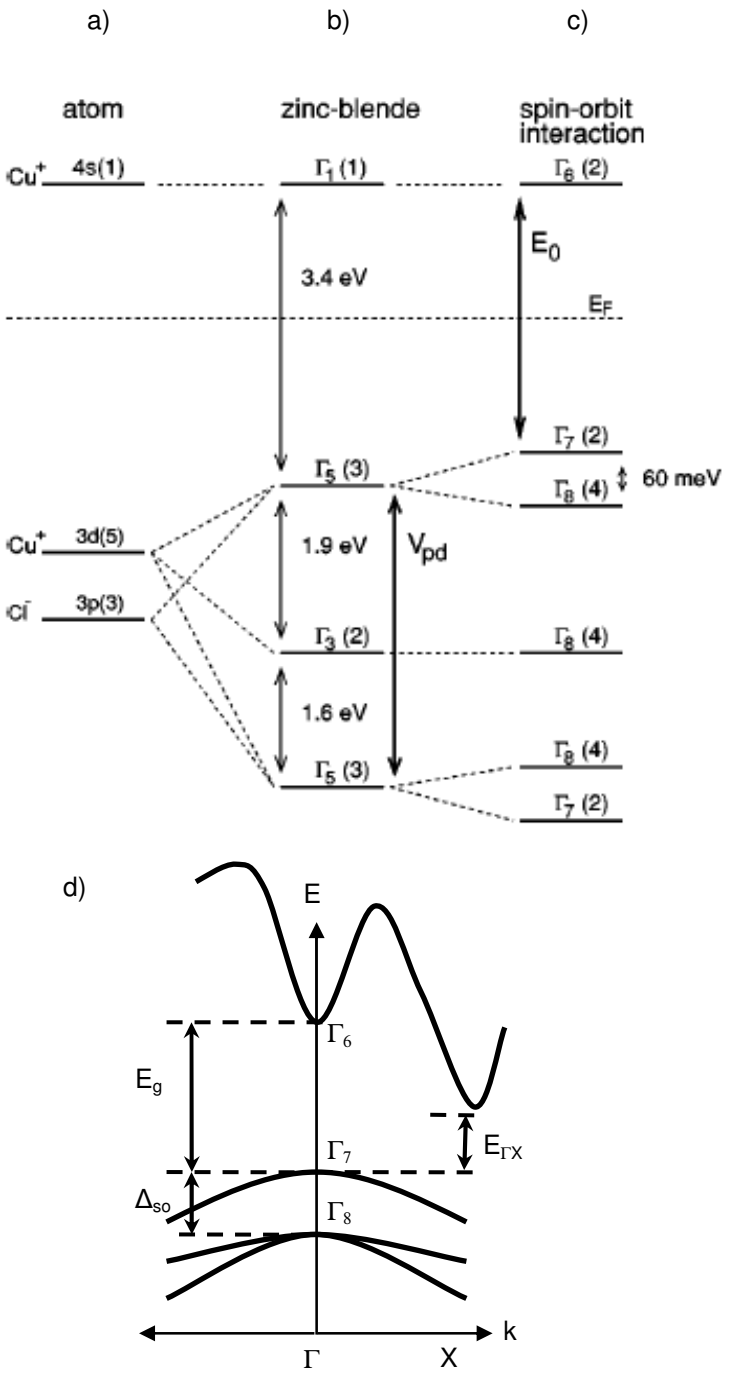

Figure 1.2: Schematic of CuCl conduction and valence bands.[30] a) Atomic levels of Cu and Cl, b) partial lifting of degeneracy and hybridization by the crystal field, and c) spin-orbit splitting. Vpd is a matrix element responsible for level splitting between p and d states. d) Schematic of CuCl band structure.

1.3 Excitons

An exciton is a bound electron-hole pair.[37] When an electron is excited from the valence band to the conduction band, for example by an incoming photon, a "hole" is left behind in the valence band. The Coulomb attraction between the two opposite charges binds them together forming an exciton that can travel freely throughout the lattice. Excitonic structure is commonly observed through low temperature absorption spectra. Photons with energy above the band gap are absorbed, generating free electrons and holes. The energy to create excitons is slightly less than the band gap energy to account for the exciton binding energy. Excitons are generally characterized by their size relative to the host lattice. Those localized at a lattice site are called Frenkel excitons, and those that span several lattice sites are referred to as Wannier excitons.[37] Excitons in CuCl are Wannier excitons, and all further discussion will refer to this variety. Since the exciton spans many lattice sites, the complex two-body problem it presents can be simplified by using the effective mass approximation.[38] Thus, it becomes a hydrogen-like problem with a Coulomb potential leading to the hydrogen-like series shown below the band gap. The binding energy of an exciton is defined as:

$$E_b^{ex} = R_y^* \frac{1}{n^2} \qquad (R_y^* = R_y^{hydrogen} \frac{\mu}{m_0 \varepsilon^2}) \qquad [1.1]$$

where n = 1, 2, 3, … is the principal quantum number, R_y^* is the exciton Rydberg energy, μ is the translational exciton mass and ε is the dielectric constant of the crystal lattice. The excitonic Bohr radius, which describes the size of the exciton, is defined as:

$$a_B^{ex} = a_B^H \varepsilon \frac{m_0}{\mu} \qquad (a_B^H = \text{hydrogen Bohr radius}) \qquad [1.2]$$

Both R_y^* and a_B^{ex} depend on the mass of the exciton, and thus the band structure of the material. Dimensionality also strongly influences the character of an exciton; for example, quantum confinement in low-dimensional structures increases the binding energy.[39]

The analogy of excitons to hydrogen atoms can be taken a step further. Just as two opposite-spin hydrogen atoms can bind to form a hydrogen molecule, two excitons can bind to form an excitonic molecule, or biexciton.[40] Technically, a biexciton is a four-body problem; however, one may consider it a two-body system of point-like excitons if $E_b^{biex}/E_b^{ex} << 1$, where E_b^{biex} and E_x^{ex} are the binding energies of the biexciton and exciton, respectively. The mass of the biexciton is twice that of a single exciton.[41]

There are several conservation laws that must be satisfied for a photon absorption process to excite an exciton. These apply to energy, momentum, angular momentum, and parity. The exciton must have the photon's energy and center-of-mass momentum (~0 for visible light). In the dipole approximation, photons have angular momentum of $\lambda = 1$ that is transferred to the exciton. For direct gap semiconductors, the transition at the wavevector $k = 0$ is dipole-allowed; however, for indirect gap materials, a phonon is required to provide the necessary momentum transfer.[37]

Excitons have a limited lifetime in a crystal before they either dissociate into a free electron-hole pair or recombine, giving off a photon with the internal energy of the exciton (luminescence). Biexcitons also have limited lifetimes based on the time for one of the excitons to recombine. Before recombination, excitons and biexcitons may become bound at impurities such as neutral or ionized donor and acceptor sites. The binding energy to these impurities is generally small, on the order of several meV.

1.3.1 Exciton Luminescence

Luminescence from free and bound excitons and biexcitons provides a useful tool in evaluating exciton population dynamics, band structure, and crystal quality.[42] Luminescence is essentially running the photon absorption process in reverse, and the same conservation rules apply. Consequently, recombination occurs only for a small portion of the population of free excitons, and a photon may be reabsorbed and re-emitted by the crystal many times before escaping the surface.[37] During this time, there is a significant probability that the excitons will be bound at impurities. Once bound at an impurity,

an exciton becomes localized, and momentum conservation no longer applies, thus they are free to recombine radiatively or nonradiatively. Free excitons can also radiate via phonon-assisted modes, as conservation laws are satisfied for the entire exciton population. Biexcitons decay by recombination of one exciton, leaving a photon plus an exciton. Thus, while the internal energy of a biexciton is twice that of an exciton, it luminesces at the exciton energy less the biexciton binding energy. All of these processes have discrete energy differences that can be resolved in a photoluminescence spectrum. Such measurements are made at liquid helium temperatures to avoid the thermal dissociation and broadening of low energy modes.

Photoluminescence is a common technique for measuring luminescence spectra.[15] A laser, either continuous wave (CW) or pulsed, is used to irradiate a sample with photons. Above-the-gap excitation utilizes photons with energy greater than the band gap of the material. Each photon can create a single electron hole pair that will become an exciton (one-photon absorption). The difference between the incident photon and exciton energies is carried by the excitons, making them "hot." A second excitation process involves tuning the laser output to half the exciton energy. In this case, one photon excites a virtual intermediate state that is converted by a second photon into an exciton (two-photon absorption). Since the two photons added together are exactly the exciton (or biexciton) energy, they are considered "cold" and the process is highly resonant.[41]

1.3.2 Excitons in Copper Chloride

The excitons generated in CuCl set it apart in a diverse landscape of semiconductor materials. The exciton of interest is the 1s exciton that comes from the transition between the lowest conduction (Γ_6) and highest valence (Γ_7) bands, commonly labeled the Z_3 exciton. The $Z_{1,2}$ exciton ($\Gamma_8 \rightarrow \Gamma_6$) is the second exciton of note; however, it only appears in absorption spectra and has no luminescence signature. The electron-hole exchange interaction in the Z_3 exciton leads to splitting into a triplet state and an optically-inactive singlet state.[41] Figure 1.3 is a low temperature absorption spectrum showing the various exciton lines in CuCl.[43] The triplet state is further split into one longitudinal and two transverse modes that can

couple with photons to form exciton-polaritons. Table 1.1 summarizes the critical exciton and biexciton parameters.

Table 1.1: Summary of the Z_3 exciton and biexciton parameters in CuCl.

Exciton binding energy	Exciton Bohr radius	Biexciton binding energy	Electron-hole mass ratio	Exciton lifetime	Biexciton lifetime
E_b^{ex}	a_B^{ex}	E_b^{biex}	σ	τ	τ
190 meV	7.04 Å	32 meV	0.2	200 ps	60 ps

The exciton binding energy of CuCl is much larger (and Bohr radius much smaller) than those found in III-V and II-VI semiconductors, making excitons in CuCl stable at room temperature. The biexciton binding energy is also very high, allowing spectra to be measured up to 100 K[44] and large densities of biexcitons to be stable before transforming to an electron-hole liquid.[45] Indeed, the concept of the biexciton was first experimentally confirmed in bulk CuCl.[40] Since excitons and biexcitons are bosons, there has been a push to observe Bose-Einstein condensation in CuCl.[2,38]

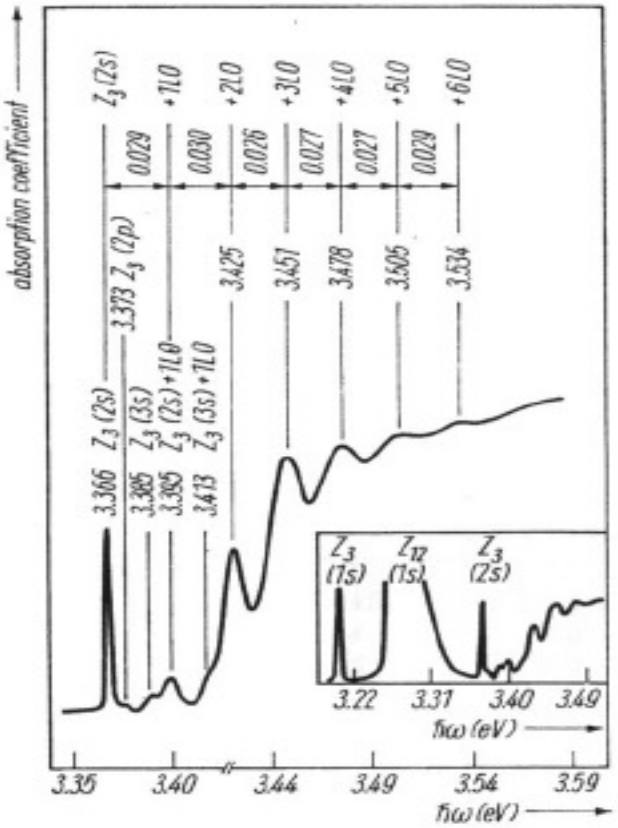

Figure 1.3: Absorption spectrum of CuCl by Mysyrowicz *et al.*[46]

1.4 Nonlinear Optics

The field of nonlinear optics (NLO) can be strongly linked to the availability of high-intensity lasers, as they provide the intensity needed to modify the optical properties of a material. Nonlinear optics studies the phenomena that occur due to the modification of the optical properties of a material by light.[47] "Nonlinear" refers to the fact that the response of the material depends nonlinearly upon the optical field strength. The optical response is defined by the dipole moment per unit volume, or polarization **P**(t), and the strength of the applied optical field is **E**(t). Following the derivations of Boyd, weak fields elicit a linear response:[48]

$$\mathbf{P}(t) = \chi^{(1)} \cdot \mathbf{E}(t) \qquad [1.3]$$

Here, $\chi^{(1)}$ is the material susceptibility, a second rank tensor. Moving into the nonlinear regime, χ becomes **E**(t)-dependant, and **P**(t) can be expressed as a power series:

$$\mathbf{P}(t) = \chi^{(1)} \cdot \mathbf{E}(t) + \chi^{(2)} \cdot \mathbf{E}^2(t) + \chi^{(3)} \cdot \mathbf{E}^3(t) + \mathrm{K}$$

$$\mathbf{P}(t) = \mathbf{P}^{(1)}(t) + \mathbf{P}^{(2)}(t) + \mathbf{P}^{(3)}(t) + \mathrm{K} \qquad [1.4]$$

The values of $\chi^{(n)}$ are the n^{th}-order susceptibilities that are n+1 rank tensors.[34] In this formulation, it is assumed that the material responds instantly to the applied field and by Kramers-Kronig relations, that it be lossless and dispersionless. Equation 1.4 implies that in a nonlinear experiment, light transmitted by the material contains the input frequency as well as the double and triple frequencies: second harmonic (SHG), and third harmonic generation (THG), respectively.

1.4.1 Second Harmonic Generation

Figure 1.4 is a schematic of the SHG process. In the energy level diagram, the solid line represents the atomic ground state, and the dashed lines are virtual states accessed by the photon and atomic energy eigenstates combined.[48] Quantum-mechanically, two photons of frequency ω are destroyed, and one photon of frequency 2ω is created simultaneously.

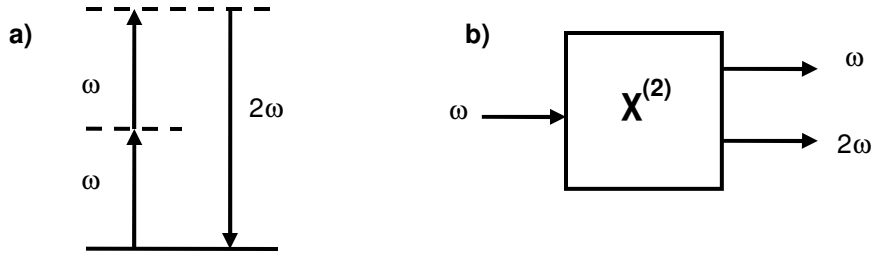

Figure 1.4: a) Energy level diagram and b) schematic for SHG.[49]

SHG is a coherent process requiring that both excited states have the same phase as the incoming light.[34] For monochromatic laser light, the field is given by:

$$\mathbf{E}(t) = \mathbf{E} \cdot e^{-i\omega t} + c.c \qquad \text{(c.c. = complex conjugate)} \qquad [5]$$

The nonlinear polarization (with nonzero $\chi^{(2)}$) is then given by:

$$\mathbf{P}^{(2)}(t) = 2\chi^{(2)} EE^{*} + (\chi^{(2)} E^{2} \cdot e^{-2\omega t} + c.c) \qquad [6]$$

The second order polarization consists of two contributions: one at zero frequency (first term) and one at 2ω (second term). This second term leads to the generation of photons at 2ω, while the first term does not generate any radiation as its second time derivative is zero.[48] A more realistic picture of SHG should include effects such as dephasing, pump depletion, symmetry, and bulk/surface contributions. The result of these processes is that not all of the incident frequency ω is converted to 2ω, as shown in Figure 4b.[48]

Crystal symmetry plays a significant role in SHG. For a crystal with inversion symmetry, all even-order χ's will vanish. For incoming fields $\mathbf{E}(\omega)$ and $-\mathbf{E}(\omega)$, two opposite dipoles will be created: $\mathbf{P}(2\omega)$ and $-\mathbf{P}(2\omega)$. By Equation 6, this is only possible if $\chi^{(2)} = 0$, which eliminates 11 of the 32 crystal classes.[34] Spatial symmetry also has an effect and eliminates some systems while simplifying others.[47] Since crystal symmetry is broken at surfaces and interfaces, it is still possible to see localized SHG in a centrosymmetric crystal. The zincblende structure is one of the few cubic structures which, while highly ordered, lacks inversion symmetry. This can be seen in Figure 1.1 where the nearest neighbor atoms are different; so there is no point of inversion in the crystal along the [111] direction.

Second harmonic generation has proven to be a very useful tool both in optics and materials characterization. It has been extensively used as an analytical tool for monitoring surfaces, interfaces, and ferromagnetic domain growth.[34] Since the selection rules for SHG differ from the linear optical regime, it can also be a powerful spectroscopic tool for probing specific excitations.[34] Researchers have used this technique to measure SHG enhancement by excitons in CuCl, C^{60}, and NiO.[49]

1.4.2 Second Harmonic Generation in Copper Chloride

Second harmonic generation has been measured in a variety of CuCl structures. Early measurements focused on determining the second order nonlinear coefficient for CuCl single crystals.[30,50,51] There were conflicting reports as to the absolute sign of the coefficient, but later studies confirmed that Cu 3d electron contributions make it negative.[52,53] CuCl has also been used extensively to study the effects of excitons on SHG. It has been shown that SHG is strongly enhanced by the $Z_{1,2}$ and Z_3 excitons in CuCl, yet remains unaffected by band gap or electron-hole continuum contributions.[49,54] SHG enhancement also occurs for glasses (normally SHG-forbidden) doped with microcrystalline CuCl clusters.[55]

1.5 Growth of CuCl Thin Films and Nanostructures

Due to its relatively low melting point, CuCl is ideally suited for vapor growth techniques. Strongly ionic compounds tend to evaporate congruently as molecules; in a CuCl vapor Cu_3Cl_3 and Cu_6Cl_6 are the most stable species.[56] Thermal evaporation (TE) and molecular beam epitaxy (MBE) are the two conventional techniques for growing thin films of CuCl.[45,56-69] Magnetron sputtering[70] and liquid-phase epitaxy[25,71] have also been utilized to grow thin films; however, the best methods for achieving high quality films have been vapor deposition techniques. There are a wide variety of substrates used for CuCl thin films, including GaP(110),[60] TiO_2(110),[72] NaCl(100),[65] MgO(001),[58] CaF_2(111),[57] Si(100),[73] Si(111),[68] GaAs(111),[73] Fe_2O_3(0001),[66] and Al_2O_3(0001).[45] Studies of the CuCl growth mechanism and structure on many of these substrates demonstrate 3D island[56-58] or layer-by-layer followed by 3D island[59] growth. Very thin films grown by MBE are able to nucleate in a purely layer-by-layer growth mode up to at least 100 monolayers,[60,68] and several groups have grown single-crystal films on NaCl(100)[65] and Si(100)[73]. Monolayer growth and single-crystal films have been unattainable using thermal evaporation growth methods.

The unique excitonic and optical properties of CuCl make it an excellent choice for quantum confinement experiments. CuCl quantum dot (1D)[74,75] and quantum well (2D)[67,76] structures have both been fabricated. A CuCl quantum well is simply a monolayer film confined between two buffer layers.

CuCl quantum dots are generally grown by doping NaCl single crystals with Cu so that CuCl nanocrystals precipitate out into the matrix. Solution methods have also been used to nucleate CuCl tetrapods and nanocrystals.[77,78]

Section 2: Fabrication and Optical Characterization of CuCl Thin Films

2.1 Thermal Evaporation of Copper Chloride Thin Films

CuCl thin films were grown by thermal evaporation in a modified Edwards 306A vacuum coating system (BOC Edwards Inc., U.K.).[45] Figure 2.1 is a schematic of this system. A rotating turret with a capacity of up to four source boats allowed for multilayer growth without breaking vacuum. The system was pumped with an E04K diffusion pump backed by an Edwards E2M8 mechanical pump, providing a base pressure of 7.5×10^{-7} Torr. A liquid nitrogen-charged cold trap was situated before the chamber to trap any oil vapors. Material was evaporated from resistively-heated tungsten or molybdenum source boats. A quartz crystal microbalance (QCM) was used to monitor growth rate and film thickness during deposition. In addition to CuCl, the system was typically used for evaporation of metals such as gold, silver, copper, aluminum, zinc, and iron and other low melting temperature dielectrics, such as calcium fluoride (CaF_2) and magnesium fluoride (MgF_2). Substrates were typically mounted on a plate that is situated 14 cm from the source boats. The center of the plate was aligned with the center of the source boat. There were six holes around the outside of the plate, 5 cm from the center. The QCM was placed over one of these holes during the deposition. A tooling factor was programmed into the QCM read-out to calibrate the film thickness.

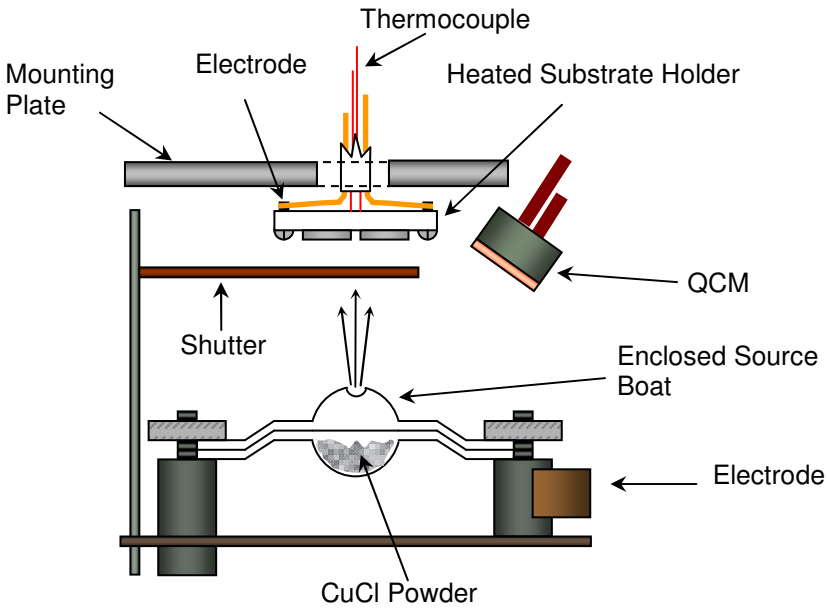

Figure 2.1: Schematic of CuCl thermal evaporator system with enclosed boat source and heated substrate holder.

Two important modifications were made to facilitate high quality CuCl film growth. The first was the use of an enclosed source boat. This special boat was made of one tungsten evaporator boat inverted and clamped on top of another with a small hole drilled in the top. In a simple open boat source, CuCl sublimates instead of melting, making growth rate control difficult. The partial pressure of CuCl vapor inside the enclosed boat allowed the source material to melt instead of sublime, providing even heating of the source and a stabilized flux of CuCl. The source material was CuCl powder (Alfa Aesar 99.999% purity). CuCl reacted with moisture to form Cu^{++} ions,[79] easily recognized by their bright green color. Consequently, the source was kept in vacuum storage at $2x10^{-6}$ Torr, and films were kept in sealed vials with a small amount of desiccant. The second modification was the addition of a resistively-heated substrate holder. The holder was designed to fit through the hole in the mounting plate, protruding a few centimeters beneath. A thin sheet of Inconel was attached to a ceramic disk with two screws. A four-hole ceramic rod ran perpendicular to the plate and provided electrical isolation for two power supply wires (attached to the screws) and two thermocouple wires. The thermocouple wires were placed beneath the

Inconel plate and sandwiched between the ceramic disk and a thin piece of mica. Substrates were secured to the holder with thin Inconel strips that were bolted to the ceramic disk.

Substrates could be heated from 60 – 150 ^{o}C during film deposition; however, at temperatures above 110 ^{o}C CuCl began to re-evaporate off the substrate at rates comparable to the growth rate, resulting in semi-continuous films.[45,57] A typical growth rate was 0.15 nm/s. Table 2.1 lists the substrates and growth temperatures used for CuCl thin film fabrication.

Table 2.1: List of substrates and parameters for CuCl thin film fabrication.

Material	Structure	Lattice	Mismatch	Growth Temp.
CuCl	Zincblende	a = 5.406 Å	--	--
Si	Diamond	a = 5.43 Å	0.44%	60 ^{o}C
Al_2O_3	Rhombohedral	a = 4.759 Å c = 12.99 Å	-12%	110 ^{o}C
Quartz	Trigonal	a = 4.914 Å c = 5.405 Å	-9.1%	--
CaF_2	Fluorite	a = 5.463 Å	1.1%	60 ^{o}C

Substrates were prepared for deposition by ultrasonic degreasing for 5 minutes each in hexane, acetone, and methanol. They were rinsed with deionized water and dried by spinning and dry nitrogen bursts. After degreasing, Si substrates were placed in 5% hydrofluoric acid (HF) or a buffered HF solution for 1 minute followed by a soak in deionized water to etch away the intrinsic SiO_2 layer and hydrogen-terminate the surface.[80,81] Optimal growth temperatures in Table 2 were determined from the full-width half-maximum (FWHM) of x-ray rocking curves.[45] At these temperatures coherent films could be grown from 50 nm to 200 nm. Films less than 50 nm thick were predominantly isolated islands, and a film thickness of 200 nm was the limit for one source boat. Multiple source boats could be used to grow films up to 1 μm thick. Many films were also capped with ~25 nm of MgF_2 or CaF_2 immediately following the

CuCl film growth. This is a common technique for protecting CuCl films from moisture[64] and helps prevent damage from the intense laser pulses used in some optical measurements.

2.2 Fabrication of Copper Chloride Pellets

Copper chloride pellets were fabricated by cold-pressing the 99.999% CuCl powder used for source material in the thermal evaporator. A two inch steel pellet die was thoroughly cleaned prior to pressing each pellet. The die was placed in a hydraulic press and subjected to approximately 75 psi of pressure for 1 minute. The pellets were about 1 cm thick and 2 inches in diameter. After pressing, the pellets appeared evenly colored and slightly translucent. One sample was kept in air and a second was stored in a bottle with desiccant. Some of the CuCl powder was placed in a sealed quartz capillary tube to compare with the pellets.

2.3 Characterization of Copper Chloride Thin Films

2.3.1 Scanning Electron Microscopy

CuCl is not easily characterized by SEM; the electron beam provides enough energy to split off Cl^- ions, leaving metallic copper. Under an intense beam, this results in the growth of small Cu nanowires out of the CuCl crystals. This phenomenon has been seen in other CuCl films[82] and has been proposed as a technique for creating Cu nanowires.[83] The few images available in literature for comparison are atomic force microscopy (AFM) images of thin CuCl films grown on MgO and CaF_2 substrates.[56-59] Modifying conventional SEM imaging procedures allowed for the capture of micrographs from a wide variety of CuCl surfaces. The LEO Gemini 1525 was used extensively in this work. It has a Schottky field emission gun that provides excellent imaging even at low accelerating voltages. The LEO also has the advantage of computer-controlled lenses, apertures, focusing, and stage motion, allowing for rapid image capture once brought into focus. This helped prevent excessive degradation of the CuCl film in the electron beam.

2.3.2 X-ray Diffraction

The Rigaku ATX-G system (Cu K_α λ = 1.5406 Å) was used to examine the crystal structure of CuCl films and pellets. The system was set in a parallel beam geometry, had a four-circle diffractometer, and had a highly monochromatic beam with the option of having a Ge(111) compressor crystal installed for higher resolution. Rocking curves (ω-scans) were used to determine the out-of-plane alignment of the CuCl crystallites. The rocking curve width was controlled by the population of crystallites that diverge from the [111] direction of the film; a high quality film with well-aligned crystallites had a narrow curve, while a film with poorly-aligned crystallites had a broader curve. The system was used without the Ge(111) compressor crystal (slit geometry) to measure the powder diffraction pattern from CuCl pellets.

2.3.3 Spectroscopic Ellipsometry

Spectroscopic ellipsometry (SE) is a useful tool for non-destructive determination the complex refractive index and thickness of thin film dielectric films. The SE measures changes in the phase and amplitude of an elliptically polarized light source that is reflected off of a surface. These shifts are related to the refractive index and thickness of the material. A SOPRA ES4G spectroscopic ellipsometer (Sopra, Inc.) was used to measure the wavelength-dependent refractive index of CuCl. Data fitting was done in the Winelli program using a Cauch law polynomial model to determine the real (*n*) and imaginary (*k*) parts of the refractive index.

2.3.4 UV-Visible Absorption

A Cary 1E UV-Vis spectrophotometer was used to measure the room temperature absorption spectra from CuCl thin films. The high exciton binding energy meant it was possible to resolve some of the exciton peaks even at room temperature. Prior to measuring the CuCl films, a blank substrate was scanned to create a background spectrum. This was subtracted from the CuCl data to remove any effects of the substrate. The spectral bandwidth was 0.2 nm to 4 nm. Scans were made from 500 nm to 350 nm.

2.3.5 Low Temperature Photoluminescence

Figure 2.2 shows a schematic of the set-up used to measure photoluminescence from CuCl thin films and pellets. The samples were mounted and cooled to 2K in a Janis variable gas-flow optical cryostat. The low temperature eliminated thermal broadening effects from the system and allowed for better resolution of the various exciton emission lines. CuCl samples were typically excited in three modes: 1) over-the-gap excitation (OTGE), 2) resonant two-photon excitation (RTPE), and 3) non-resonant excitation. Over-the-gap excitation was achieved using the frequency-tripled output (355 nm) of a passive-active mode-locked Nd:YAG laser. This laser produced a train of pulses with a width of about 15 ps and a repetition rate of 10 Hz. The laser could also be directed to an optical parametric amplifier (OPA) to generate light in the ranges of 400 – 685 nm and 737 – 3156 nm. Laser light from the Nd:YAG laser or the OPA was focused using a 15 cm lens to a 3 mm spot on the sample. The corresponding power flux could be varied from 0.1 MW/cm^2 up to 8 GW/cm^2.

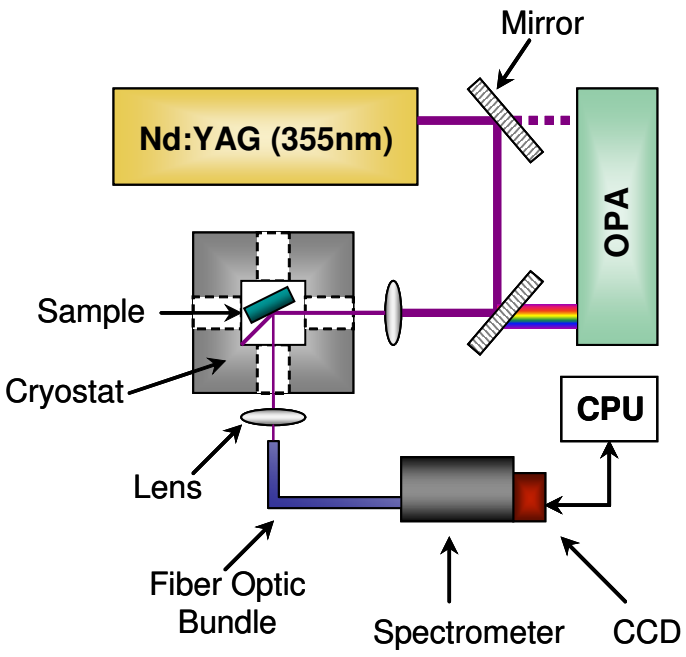

Figure 2.2: Schematic of the setup used to measure low temperature photoluminescence.

To achieve RTPE, the output of the OPA was passed through a frequency-doubling beta barium borate (BBO) crystal. The PL from excitonic matter was collected in reflection geometry and focused onto a fiber optic bundle. The output of the fiber optic bundle was coupled to the entrance slit of a Spex Spec-One 500M spectrometer and detected using a nitrogen-cooled CCD camera. A filter was used to remove 355 nm pump light. The fiber optic bundle was attached to a rotating stage to allow for angular dependent PL measurements.

2.3.6 Second Harmonic Generation

Angle-dependent second harmonic generation was used to determine the nonlinear susceptibility of CuCl thin films deposited on c-plane sapphire and CaF_2(111). The system is shown schematically in Figure 2.3. The fundamental beam from a Quanta Ray DCR-1 Nd:YAG laser (1064 nm) was split between a sample and reference arm. The laser produced pulses with a 5 ns width at a 10 Hz repetition rate with approximately 750 mJ per pulse. In the reference arm, the unfocused beam was filtered to remove 532 nm light generated in the optics, passed through a quartz reference to generate light at 532 nm, then passed through another filter to remove 1064 nm light, and detected using a photomultiplier tube (PMT). In the sample arm, the beam was p-polarized, focused to a 1 mm spot size, filtered to remove SHG light, attenuated with a half-wave plate (if necessary), passed through the sample, filtered to remove fundamental light, attenuated, if needed, and detected with a PMT. Both PMTs and the sample were enclosed in a box to improve the signal to noise ratio. Signals from the sample and reference arm were synched using a trigger signal and sent to boxcar integrators. The ratio of sample to reference intensity was taken to minimize the effects of laser fluctuations and was sent to the computer. The computer controlled the θ rotation of the sample stage during the measurement. The azimuthal angle φ was adjusted manually. The computer recorded SHG intensity as a function of incident angle (θ). Scans were taken from -30^{o} to 30^{o} in 1^{o} increments with an integration time of 2 seconds (average over 20 pulses).

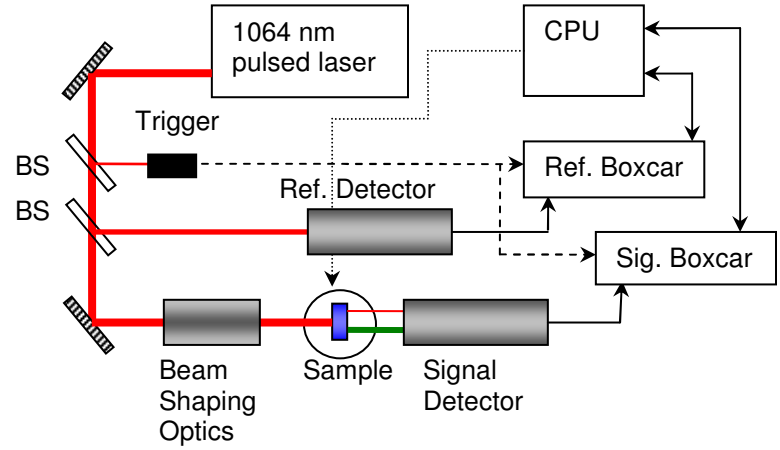

Figure 2.3: Schematic of angle-dependent SHG system.

2.3.7 Determination of the Second Order Nonlinear Coefficient for CuCl Films

The value of the effective second order nonlinear coefficient (d_{14}) for CuCl was determined from angle-dependent SHG data using the Maker-fringe technique.[84,85] The samples were attached to a small metal holder with a 3 cm aperture that was placed in the rotational stage. The alignment of the sample with the lab coordinate system is shown in Figure 2.4.

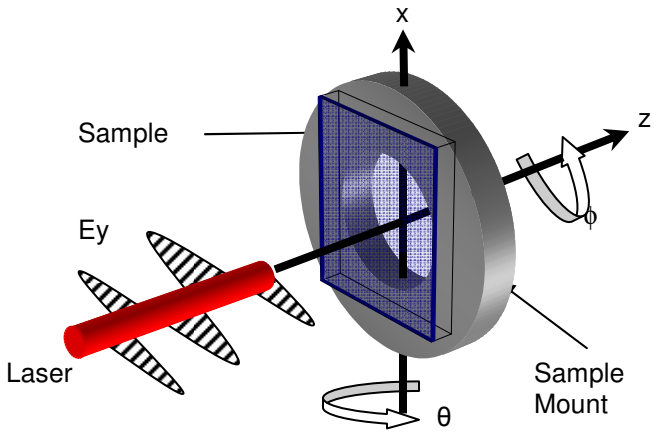

Figure 2.4: Orientation of sample and rotations with respect to the lab coordinates.

The optic axis of the film was aligned to θ = 0 by matching the position of the reflected laser spot to the incident beam. A y-cut quartz plate was measured for use as a reference. The SHG response of both the quartz and CuCl thin films were modeled using the Maker-fringe equation:[85]

$$P_{2\omega} = \frac{128\pi^3}{cA} \frac{(t_{af}^{\omega})^4 (t_{fs}^{2\omega})^2 (t_{sa}^{2\omega})^2}{n_{2\omega}^2 \cos^2(\theta_{2\omega})} P_{\omega}^2 d_{eff}^2 \left(\frac{2\pi L}{\lambda}\right)^2 \frac{\sin^2(\phi)}{\phi^2} \qquad [2.1]$$

where $P_{2\omega}$ is the second harmonic output of the sample, P_{ω} is the fundamental laser power, c is the speed of light, and A is the area of the laser spot. The Fresnel transmission coefficients at the air-film, film-substrate, and substrate-air interfaces are given by t_{af}, t_{fs}, and t_{sa}, respectively. When measuring the quartz reference, t_{fs} can be ignored. The effective SHG coefficient is d_{eff}. $\theta_{2\omega}$ is the angle of the generated SHG beam inside the sample (from Snell's Law) and $n_{2\omega}$ is the refractive index at 532 nm. The remaining terms are the sample (or film) thickness L, the laser wavelength λ, and the phase angle $\varphi = 2\pi L / \lambda [n_{\omega}\cos(\theta_{\omega}) - n_{2\omega}\cos(\theta_{2\omega})]$. The latter term is responsible for the destructive interference of SHG waves in the sample as it is rotated, creating the Maker fringe pattern. As the sample was rotated, the effective thickness increased and the wave oscillated in and out of phase.

The ratio of $(P_{\omega})^2/A$ was determined by fitting the quartz reference data to the above equation using established values for d_{11} for quartz (0.4 pm/V). The value of $(P_{\omega})^2/A$ from this fit was used to calibrate the values of d_{eff} when fitting the CuCl SHG response. Due to symmetry, CuCl has only one independent second order nonlinear coefficient, d_{14}. To properly determine the value of d_{eff} in Equation 2.1, the crystal coordinates need to be transformed to the lab coordinate system. This was done using a set of rotation matrices to determine the final form of d_{eff}.

$$d_{eff} = -\sqrt{\frac{1}{6}} d_{14} \sin^2(\theta) \qquad [2.2]$$

This equation was substituted into Equation 2.1 and fit to the CuCl SHG data to determine d_{14}.

Section 3: Structure and Optical Properties of CuCl Thin Films

3.1 Structure of CuCl Thin Films

The morphology of CuCl thin films varied greatly with substrate and deposition temperature. Typically, films grown at an elevated temperature had larger grains and better crystallinity than films grown at room temperature, regardless of substrate type. Figure 3.1 shows SEM images of CuCl films grown at room temperature on c-plane sapphire, Si(111), CaF_2(111) and SiO_2/Si substrates. The films grown on Al_2O_3(0001) (c-plane sapphire) and Si(111) at elevated temperature both had evidence of the triangular grain structures seen in well-oriented films grown on CaF_2(111).[57,58] At room temperature, films on Al_2O_3(0001) and CaF_2(111) were made up of small grains, and generally lacked the triangular shape. Similarly, films grown at room temperature on Si(111) exhibited smaller grains and lacked the triangular pits seen on the 60^{o}C film. Overall, the films on Si(111) were smoother and more coherent; even at room temperature, there were only a few isolated grains in the matrix of the film. The film grown on CaF_2(111) had large, random grains. This structure was similar to films grown on SiO_2/Si and quartz substrates. The grain sizes ranged from 120 – 150 nm at elevated temperature and from 20 – 40 nm at room temperature. Films grown at temperatures above 110^{o}C were not continuous, as CuCl evaporated off the substrate at rates close to the growth rate.

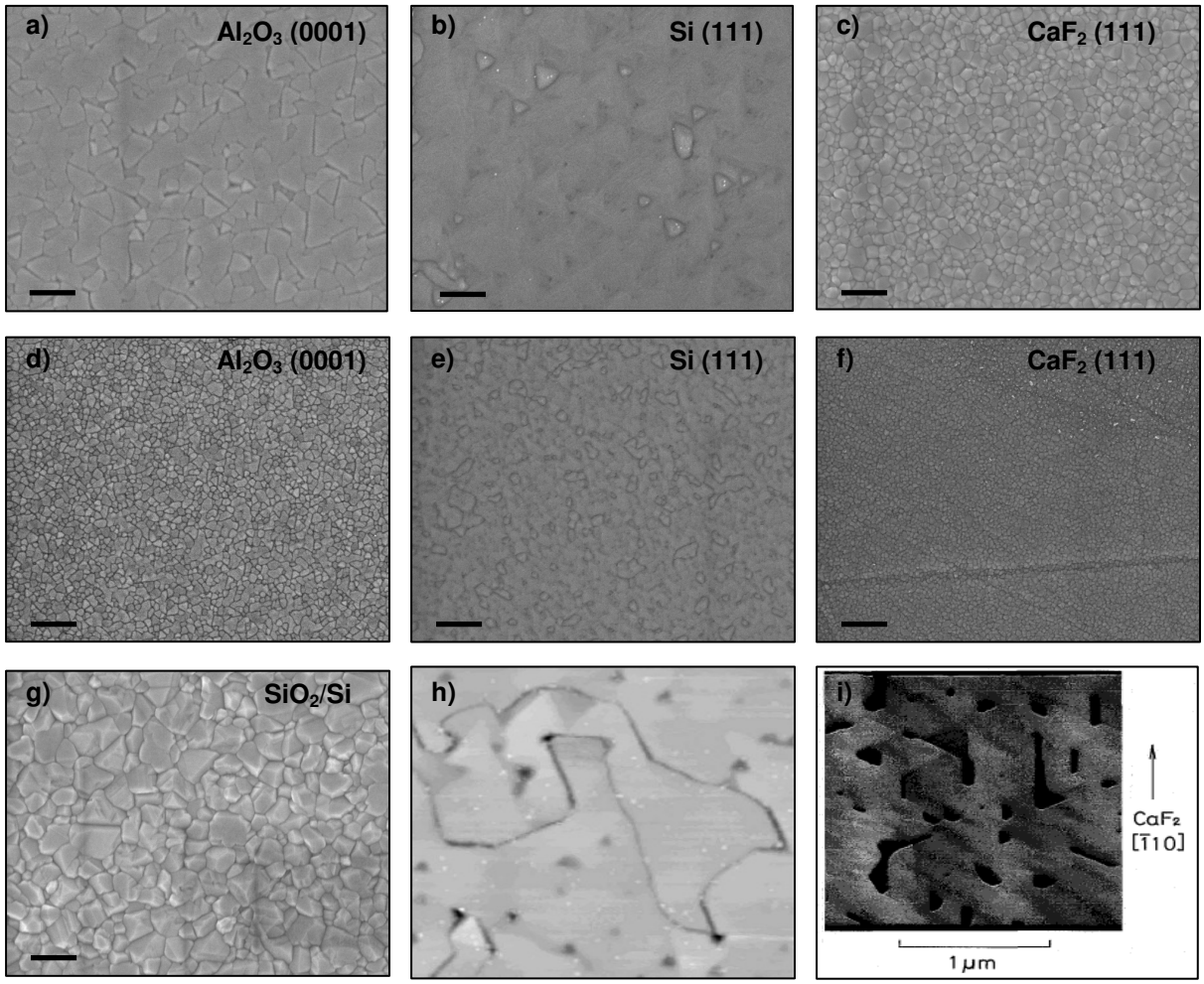

Figure 3.1: Comparison of 100 nm CuCl films grown on the substrate listed at a) 110 °C, b – c) 60°C, d – f) RT, g) 60 °C. For comparison, AFM images of CuCl on CaF_2(111) at h) 180 °C[58] and i) 80 °C.[59] Scale bar is 200 nm for a – g). The image in h) is 3 x 3 μm^2 and i) is 2 x 2 μm^2.

The film structure and substrate adherence were also adversely affected. Figure 3.2 shows the evolution of a CuCl film grown on c-plane sapphire at increasing temperature. As the temperature was increased from room temperature, there was a dramatic increase in the size and faceting of the grains. Once the substrate temperature exceeded 110°C, gaps started to appear in the film.

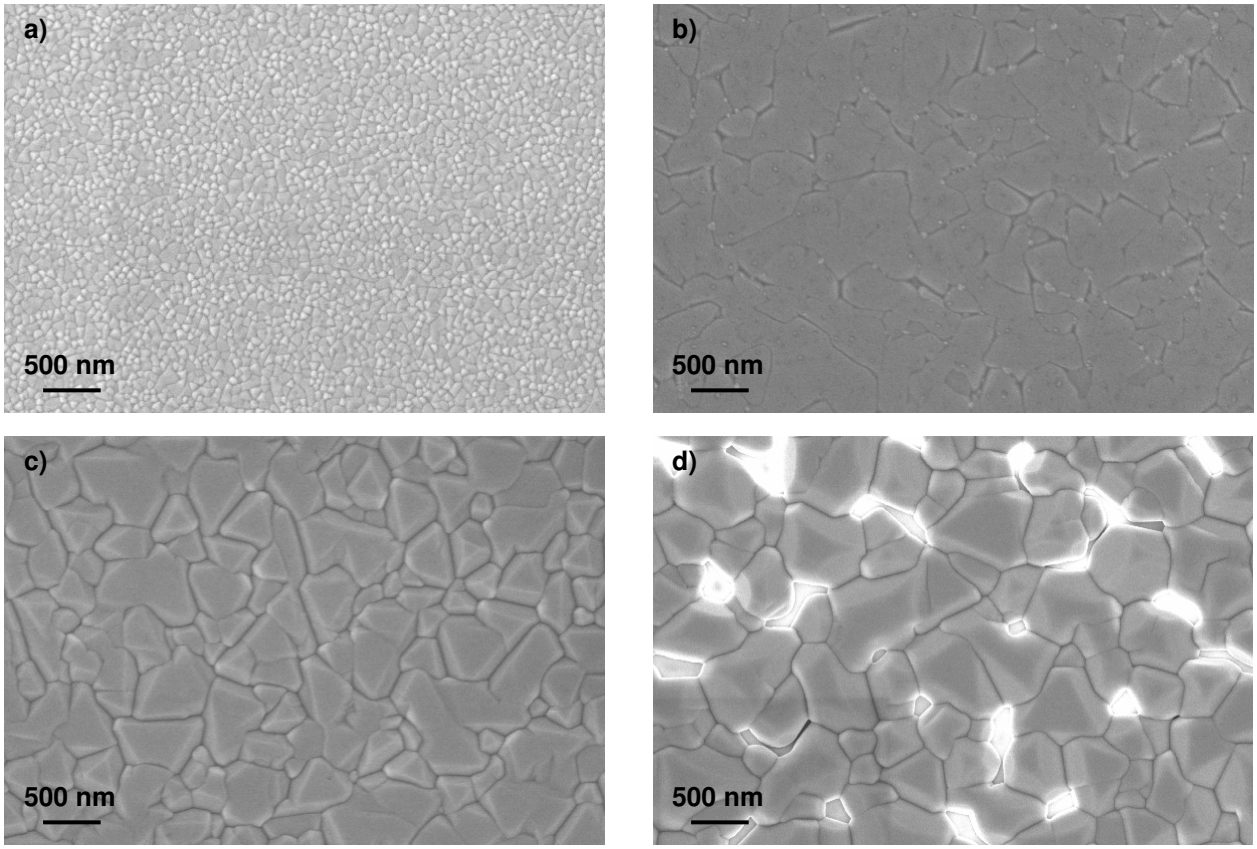

Figure 3.2: SEM images of CuCl grown on c-plane sapphire at a) room temperature, b) 60 °C, c) 110 °C, and d) 130 °C. The bright spots in d) are bare sapphire substrate.

CuCl films grown on silicon also exhibited interesting morphologies. Si was a good lattice match with CuCl (0.44% mismatch) and was useful for growing highly textured CuCl films. Like films on c-plane sapphire, the growth temperature range was highly limited. CuCl and Si could react at elevated temperatures to produce metallic Cu and $SiCl_4$.[86] CuCl evaporated onto Si(111) had the characteristic triangular grain shape seen for oriented grains on c-plane sapphire. CuCl on Si(100), however, was made up of random, roughly spherical grains. Figure 3.3 shows SEM images of CuCl films grown on each substrate at 60˚C.

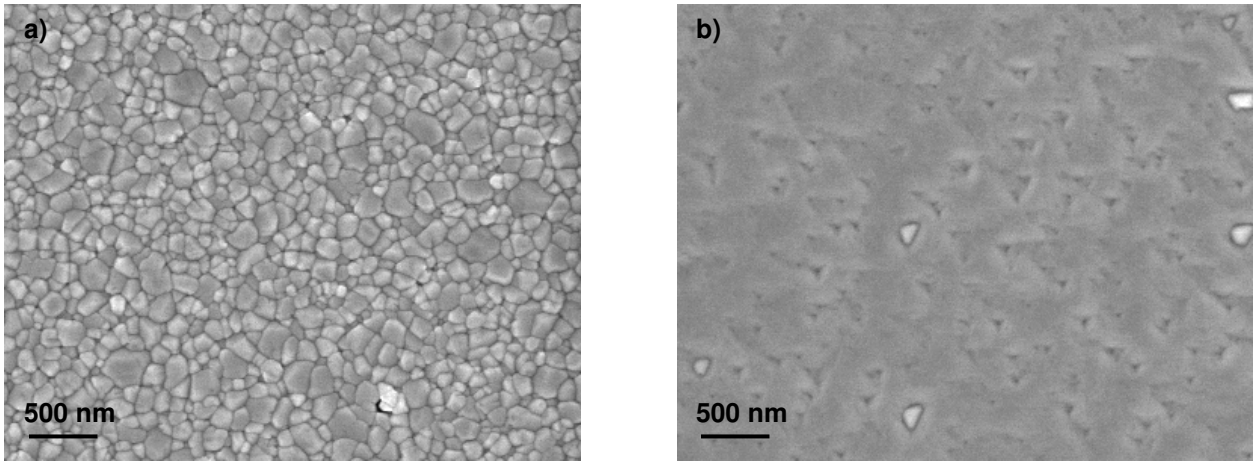

Figure 3.3: SEM images of CuCl films grown on a) Si(100) and b) Si(111) at 60 °C. The film grown on Si(100) shows randomly oriented grains while the film on Si(111) has triangular grains.

XRD was used to determine the orientation and quality of the CuCl thin films. Figure 3.4 shows typical spectra from CuCl grown on c-plane sapphire and Si(111) substrates. Both films exhibit strong [111]-oriented grains. The rocking curves for the CuCl films indicated relatively good crystal quality with full-width half-maximums (FWHMs) typically between 0.2° and 0.4°, depending on the substrate temperature. The best crystal quality for CuCl/Si(111) and CuCl/c-plane sapphire was produced at deposition temperatures of 60 °C and 110°C, respectively. The XRD spectra from CuCl films grown on c-plane sapphire at 110°C (Figure 3.4c-d) was particularly interesting. The diffraction peak was very strong and exhibited fringes commonly seen in high quality crystalline films. Film thickness determined from the fringe spacing matched well with QCM-recorded thicknesses during growth. The rocking curve for 110°C CuCl films on c-plane sapphire was distinctly different from other rocking curves at different growth temperature and on different substrates. It was significantly sharper and more intense with a broad base. The second peak at approximately 14.26° in Figure 3.4d came from CuK_β radiation that was not completely removed by the Ge(111) compressor crystal. The FWHM of a CuCl film grown at 110°C on c-plane sapphire was 0.04°, an order of magnitude lower than the FWHM for a room temperature film. This implied that the films grown at 110°C had better crystallinity than films grown at room temperature. The bulk of the crystallites were well-aligned, as shown in the sharp peak. The broad base around the peak was due to a smaller distribution of misaligned crystallites still present in the film. The triangular grains

seen in Figure 3.2 appeared to play a critical role in determining the quality of the CuCl films. These grains were small and sparse at room temperature; however, at 110˚C the triangular grains grew significantly and dominated the film morphology.

Cross-sectional analysis of the CuCl films by SEM was hampered by rapid film degradation in the electron beam. The in-plane CuCl grain size on c-plane sapphire was approximately 60 nm 47 nm for the triangular and spherical grains in the room temperature films. At 110˚C, the triangular grains are approximately 400 nm in-plane. Analysis of the diffraction peaks using the Scherrer equation yielded grain sizes of 78 nm and 96 nm for films grown at room temperature and 110˚C. The film thickness determined during growth by the QCM was 100 nm. The CuCl films grown at 110˚C were comprised of a single layer of wide, columnar grains stacked side-by-side. Each grain was seeded at the substrate surface and continued to grow until the film reached its final thickness. Likewise, CuCl films grown at room temperature appeared to be composed of one or two layers of columnar-type grains. At room temperature, a second layer of grains could stack on top of the initial layer before the film finished growing.

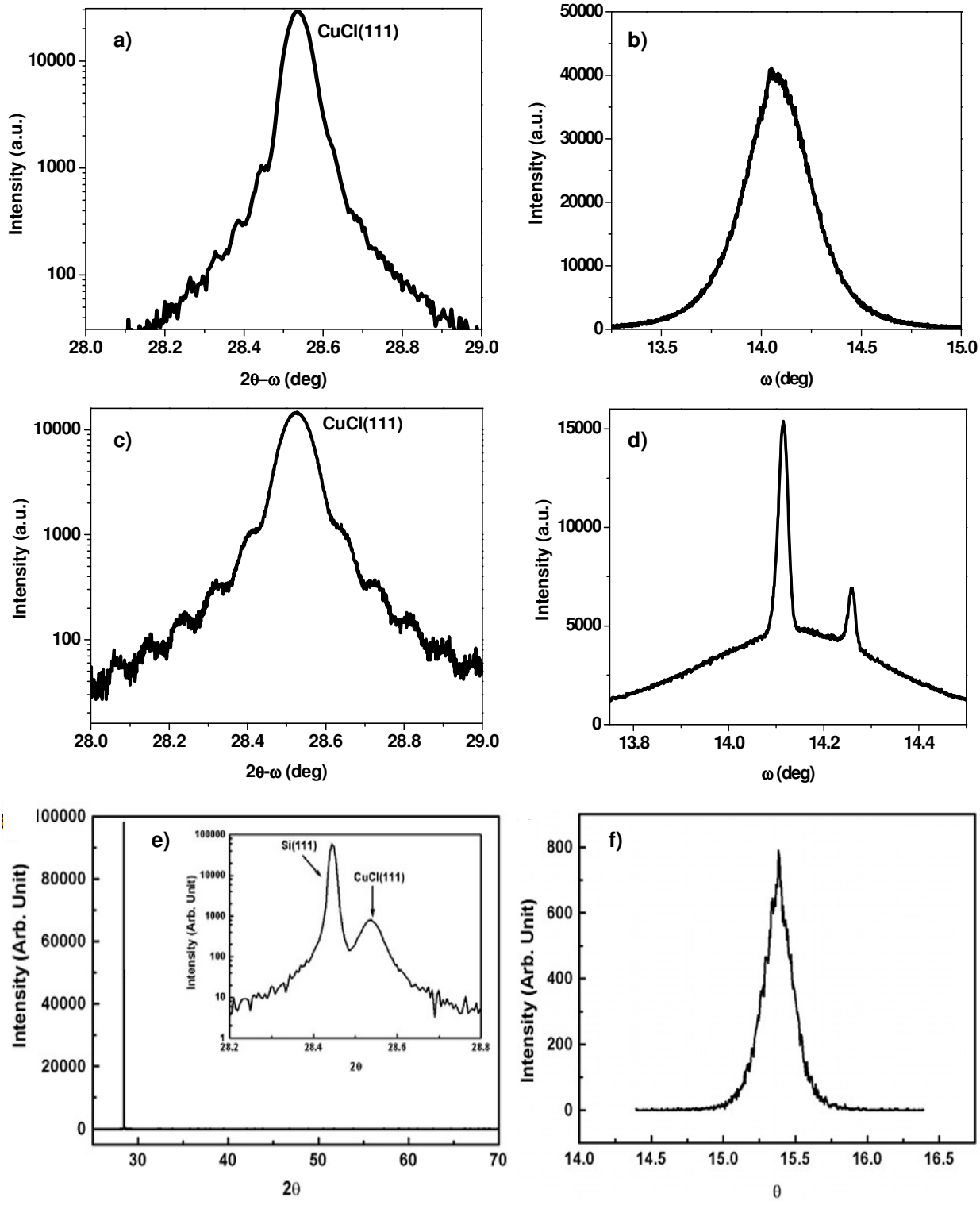

Figure 3.4: a) XRD scan and b) rocking curve for CuCl/c-plane sapphire grown at room temperature, c) XRD scan and d) rocking curve for CuCl/c-plane sapphire grown at 110 ˚C, and e) XRD scan and f) rocking curve for CuCl/Si(111).[45] The second peak in d) is due to Cu K_β x-rays that make it past the Ge(111) compression crystal.

3.2 Optical Properties of CuCl Thin Films

3.2.1 UV-Vis Absorption

The optical quality of CuCl films on transparent substrates was determined by UV-Vis absorption. The high binding energy of the primary excitons in CuCl allowed them to exist even at room temperature. The positions of the Z_3 and $Z_{1,2}$ excitons corresponded well with values found in literature.[62] Figure 3.5 is the absorption spectrum from a 100 nm CuCl film on c-plane sapphire. The energy splitting between the two exciton peaks is approximately 68 meV, consistent with low temperature exciton studies.[87] Similar absorption spectra are seen for films on other transparent substrates over a wide range of thicknesses.

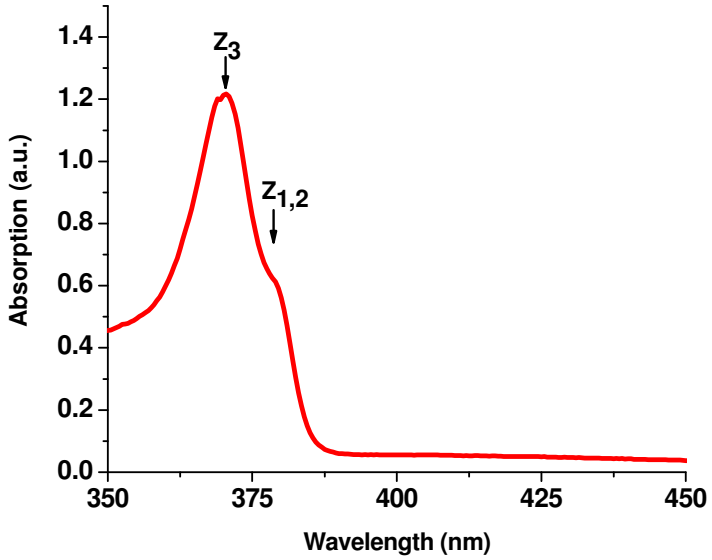

Figure 3.5: Room temperature UV-Vis absorption of a 100nm CuCl film on c-plane sapphire.

3.2.2 Low Temperature Photoluminescence from Excitons and Biexcitons

Photoluminescence measurements of CuCl thin films at 2 K showed several characteristic exciton peaks. Figure 3.6 is PL from 100 nm CuCl films on Si(111), CaF_2(111), and c-plane sapphire. The arrows in the figure show the position of the free exciton (Z_3), the impurity-bound free exciton (I_1), the free biexciton decaying to a transverse exciton (M_T), and the free biexciton decaying to a longitudinal biexciton (M_L). These peak positions correspond well with others in literature and indicate the high quality of the

films.[44] Comparing these positions to those found in traditional single crystal standards reveals that luminescence from thin films was slightly red-shifted. This is likely due to stresses built up in the film during the growth process. The CuCl film grown on c-plane sapphire had the largest lattice mismatch and showed the largest peak shift.

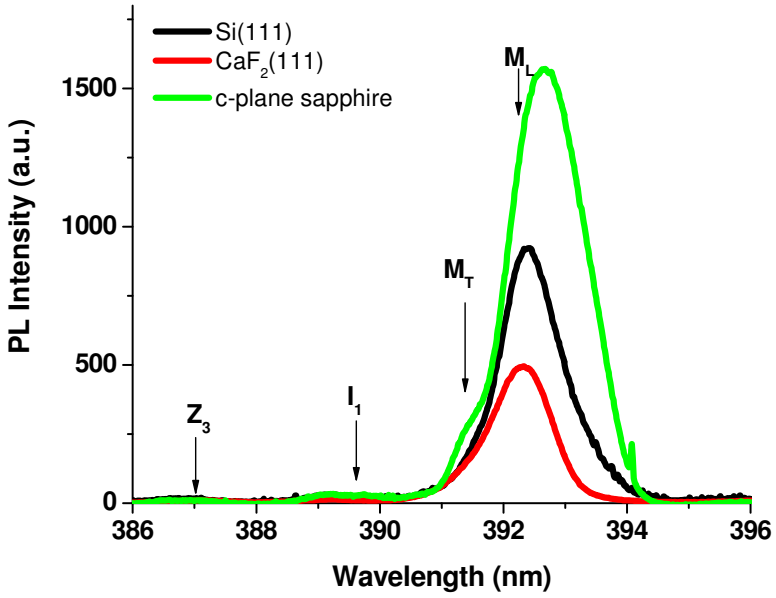

Figure 3.6: PL taken at 2K of 100 nm CuCl films on Si(111), CaF_2(111), and c-plane sapphire substrates. The labels for the exciton and biexciton emission peaks are discussed in the text.

3.3 Propagation of Bipolaritons in CuCl Thin Films

The PL spectra in Figure 3.6 show the efficient biexciton creation that occurs in CuCl films. The existence of a biexciton has been typically described using the giant oscillator strength model. In this model, biexciton formation is described as a two-photon absorption process. One photon is absorbed and creates a virtual exciton that is optically converted by the second photon into a biexciton.[88] Recently, a new model has been proposed that describes the process as the resonant excitation of bipolaritons, a coupled state between two photons and two excitons, that can propagate through the crystal.[89] To test this propagating bipolariton theory, angle dependent PL was measured from a CuCl film grown on c-plane sapphire. Two excitation regimes were used; over-the-gap excitation (OTGE) and resonant two-photon

excitation (RTPE). OTGE indirectly generates true biexcitons from a population of energetic excitons while RTPE is a resonant process that should directly create a biexciton. Figure 3.7 shows the angular dependence of the biexciton PL under each regime.[90]

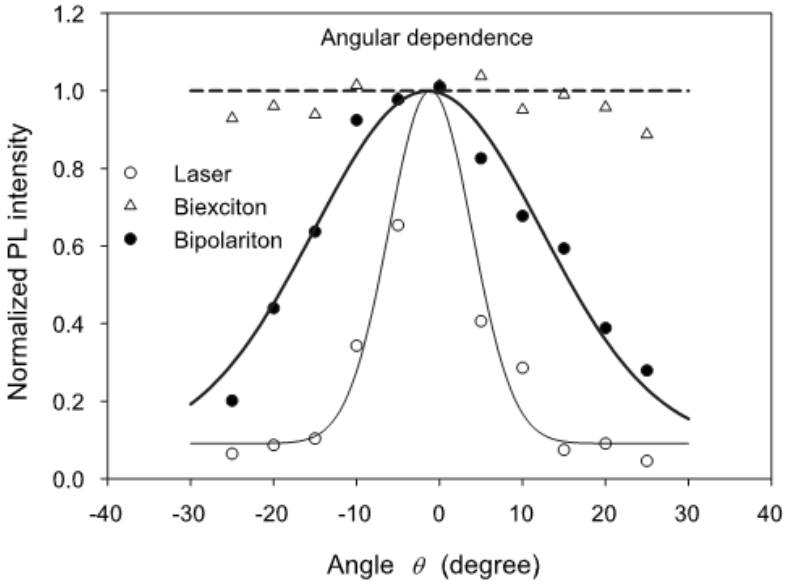

Figure 3.7: Plot of the angular dependence of biexciton (OTGE) and bipolariton (RTPE) photoluminescence. The empty circles represent the angular distribution of the incident laser.

There is a significant difference between the angular distributions of PL generated using OTGE and RTPE. The PL generated from biexcitons using OTGE is essentially isotropic and does not depend on the collection angle. In contrast, RTPE generates PL that has a broad angular dispersion that is similar to the laser dispersion. If biexcitons were generated in this process (as described by the giant oscillator strength model), their large translational mass should cause them to rapidly be scattered by random impurities in the sample. This should result in a relatively isotropic dispersion. In the context of the bipolariton model, the generated molecules (bipolaritons) consist of two very light polaritons with considerably lower mass than a biexciton. This means they could travel through the sample more quickly and with fewer scattering events. Since they are not as readily scattered, they would stay well correlated with the incident laser direction, as was seen for RTPE. The broader dispersion of the bipolariton PL for this sample is likely due to defects formed during growth.

3.4 Non-resonant Two Photon Excitation in CuCl Pellets

The two photon excitation described above is a highly resonant process that requires half the energy needed to excite an exciton or biexciton. If the excitation source is shifted away from this resonance, the excitonic population drops sharply. In experiments on a pellet pressed from the source material used in the thermal evaporator, PL from excitons was found to exist far off the resonance point. Figure 3.8 compares the PL spectra for each excitation case over a range of excitation levels.[91]

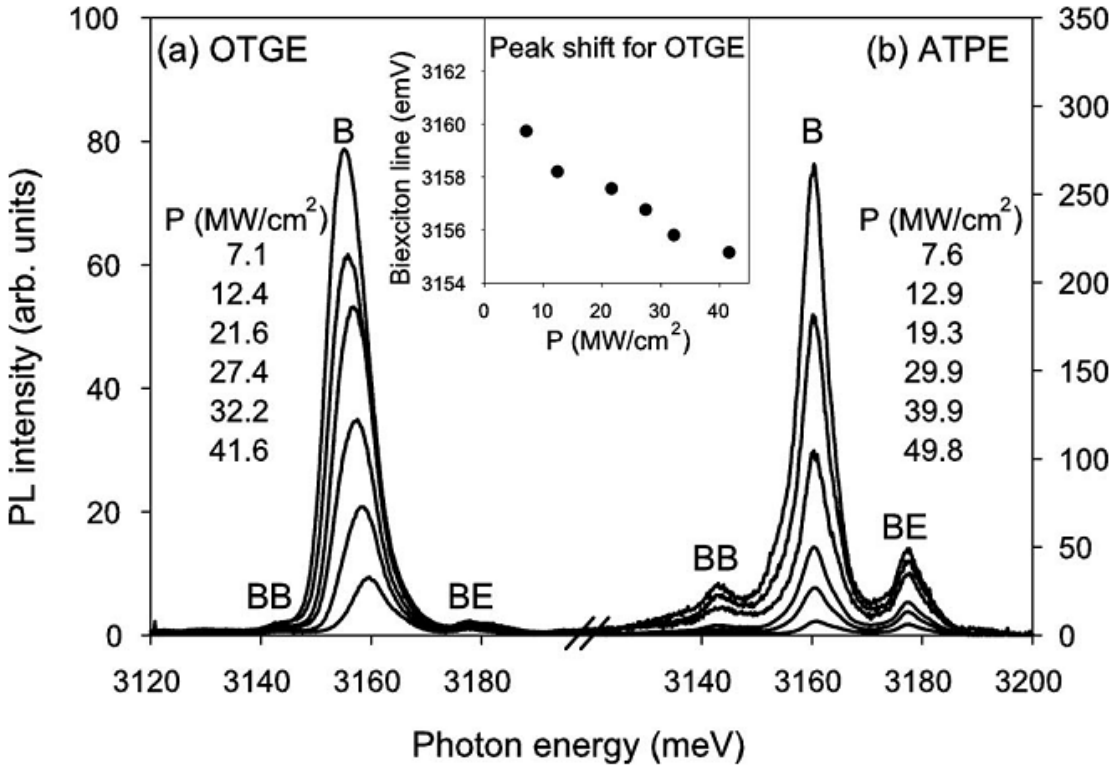

Figure 3.8: PL spectra under a) OTGE and b) anomalous two-photon excitation at a range of excitation powers. The inset shows the red-shift in the biexciton peak under OTGE due to the generation of hot (high energy) excitons.

The peak labels correspond to bound excitons (BE), biexcitons (B), and bound biexcitons (BB). The peak for excitons is minimal in both samples, implying that impurity-capture of excitons is efficient. The population of excitons and biexcitons varies from that found under normal OTGE conditions. At low excitation levels, OTGE produces a small number of biexcitons. As the power is increased, the peak for

biexcitons gradually increases, broadens, and red-shifts. The latter two effects are due to the increasing energy of the excitons generated. The excitation energy for the anomalous excitation is 2.124 eV (584 nm), well away from the band gap of CuCl and off the two-photon resonance. Surprisingly, this excitation persists over a range of energies (1.892 – 2.843 eV). This process appears to favor exciton generation more than OTGE, evidenced by the enhanced bound exciton peak. At higher excitation powers, the two spectra are very different. The biexciton peak gradually builds, but unlike the OTGE case, it is considerably narrower and does not red-shift. This implies that the biexcitons are forming from "cold" excitons (no excess energy) via a resonant multiphoton process.[91] The density of bound excitons and biexcitons can be determined from the PL intensities for each excitation. Analysis of each using steady-state population dynamics reveals that the density of excitonic material in OTGE matches well with the expected one-photon case. The anomalous excitation, however, is best fit using a two-photon excitation model. Figure 3.9 shows the results of this fit for low and high energy limits.[92]

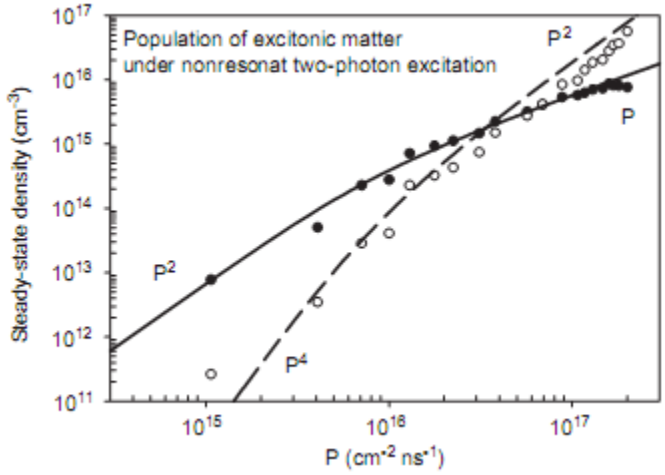

Figure 3.9: Steady-state densities of bound excitons (solid dots) and biexcitons (open dots) under non-resonant excitation. The fits for each curve are generated for a two-photon excitation case.

Similar experiments on CuCl films did not result in any non-resonant excitations. This may be because the random distribution of defects and impurities in the pellet forms a broad band that subsequently decays into the exciton ground state. The small grains should provide a large surface area for defects to populate.

3.5 Second Harmonic Generation in CuCl Thin Films

The second harmonic generation response of CuCl thin films on CaF_2(111) and c-plane sapphire were measured with angle-dependent SHG spectroscopy. Both substrates were transparent and did not exhibit any intrinsic SHG that could alter the signal from the CuCl thin films. XRD of both films revealed strongly [111] oriented grains. Figure 3.10 shows the angle-dependent SHG response for both films.

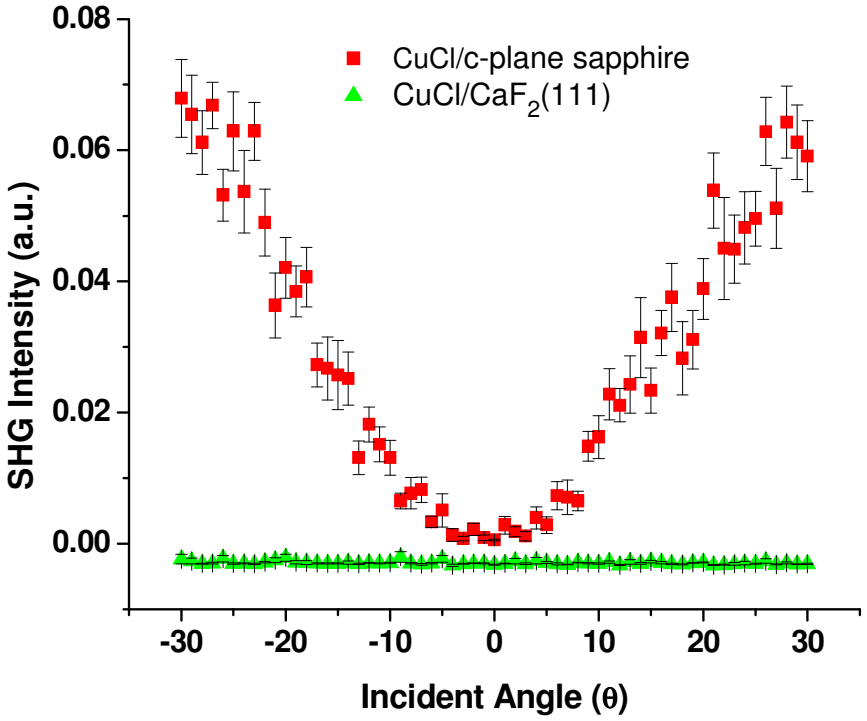

Figure 3.10: Angle-dependent SHG response from 100 nm CuCl thin films grown on CaF_2(111) (green triangles) and c-plane sapphire (red squares).

Surprisingly, there was no SHG response for CuCl films grown on CaF_2(111). Films grown on c-plane sapphire, however, exhibited a detectable SHG signal. Periodic scans made around the azimuthal axis (φ) yielded curves similar to the one above. This curve was fit with Equation 2.1 to determine the value of d_{14} for CuCl in this thin film. Figure 3.10 shows the data and the generated fit. The value of d_{14} was determined to be -1.19 pm/V, which was lower than the d_{14} found for single crystals of around -5.5 pm/V.[50,51]

CuCl crystallizes in the zincblende structure, which is non-centrosymmetric, due to the positioning of Cl atoms in the lattice. For example, the [111] and $[\bar{1}\bar{1}\bar{1}]$ directions are not equal (see Figure 1.1), yet indistinguishable, in an XRD spectrum. Individually, neither orientation has inversion symmetry; so they will be SHG active with opposing polarizations. An equal mix of [111] and $[\bar{1}\bar{1}\bar{1}]$ oriented grains, however, would result in no SHG, as the polarizations would cancel each other out. CaF_2(111) has an excellent lattice match with CuCl, so there may be no driving force to preferentially nucleate along one orientation or the other, and the grains would all average out to zero polarization. In the case of c-plane sapphire, CuCl still grew preferentially <111>-type grains, though on a hexagonal substrate with -12% mismatch. The strain in the CuCl film may drive some of the grains to grow in a particular orientation, in this case labeled the [111] direction. In this situation, the appearance of a preferential <111> orientation would yield a measureable SHG signal. XRD spectra showed that the crystal quality of room temperature films is not as high as films grown at 110˚C. Rocking curves showed that there was a certain population of [111] crystallites that were not aligned with the surface normal of the film. Grains that nucleate as $[\bar{1}\bar{1}\bar{1}]$, either on the substrate or in the second layer, or grow misaligned from the surface normal would reduce the SHG response. This was seen as a lower d_{14} value for a 100 nm thick CuCl film versus a well-oriented, high quality single crystal. A similar SHG response was observed in ZnO thin films.[93] Stacking faults would cause the hexagonal ZnO grains to flip between two orientations. Thinner films limited the presence of stacking faults and thus exhibited higher SHG response than thicker films.

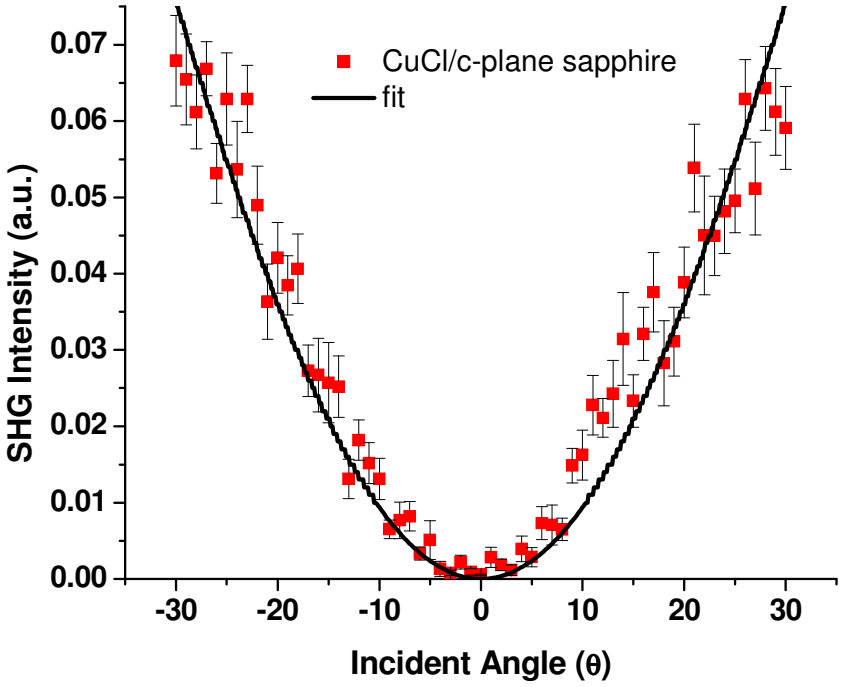

Figure 3.11: Angle-dependent SHG data for a 200 nm CuCl film on c-plane sapphire plus a fit to the Maker-fringe equation (solid line).

3.6 Conclusions

In conclusion, a straightforward thermal evaporation technique was developed for growing high quality CuCl thin films on a variety of substrates. CuCl film growth showed large temperature dependence up to 110^{o}C. At higher temperatures, CuCl desorbs from the substrate at an appreciable rate. XRD measurements of CuCl films on Si(111) and c-plane sapphire showed strong [111] texturing and good crystal quality. Both highly oriented [111] films showed a triangular grain structure consistent with other growth studies on lattice matched CaF_2(111).

The optical quality of the thin films was verified by room temperature absorption and low temperature (2 K) photoluminescence measurements. Angle-dependent measurements of resonantly excited excitonic molecules revealed a strong correlation with the incident laser light. This implied the creation of a propagating light bipolariton that would be able to travel through the crystal with diminished scattering. Similar measurements on biexcitons that were indirectly generated by over-the-gap excitation showed an isotropic distribution, as these heavy molecules were scattered quickly in the crystal. In

contrast to the highly resonant two-photon excitation in CuCl films, a CuCl pellet displayed a large non-resonant multi-photon excitation regime. Excitations in this region directly produced resonant cold excitons, as opposed to the energetic hot excitons formed by over-the-gap excitation. Steady-state population dynamics revealed that this non-resonant excitation is a two-photon process. A possible mechanism for this process is the creation of a large intermediate band from impurity/defect states that can decay to an exciton.

The second order nonlinear optical properties of CuCl films were examined using SHG. Highly [111]-oriented films grown on CaF_2(111) and c-plane sapphire were examined. The film on c-plane sapphire showed an SHG response, but no SHG signal was found for films on CaF_2(111). Analysis of angle-dependent SHG from CuCl/c-plane sapphire gave a value of d_{14} that was lower than the one measured for single crystals. A mechanism of strain-induced preferential [111] grain growth was developed. The decrease in d_{14} is likely due to lower crystal quality found in room temperature films. The lattice-matched film on CaF_2(111) should not have any preferential orientation of <111> grains and thus the polarizations (and SHG response) would balance out to zero.

Section 4: Fabrication and Optical Properties of Three-Dimensional Photonic Crystals

4.1 Introduction to Photonic Crystals

The past several decades have seen a dramatic increase in interest and understanding in the field of photonics. Photonic crystals (PhCs) have emerged as structures with enormous potential to manipulate and control light, much like the flow of electrons is manipulated in a semiconductor. Indeed, photonic crystals are often called semiconductors for light, and many analogies can be drawn between the two systems. Photonic crystals are metamaterials, which means they derive their properties primarily from their physical structure rather than their constituent materials. In this case, the structure is provided by a periodic variation in dielectric constant, $\varepsilon(\mathbf{r})$, which is on the scale of the wavelength of light. The modulation of $\varepsilon(\mathbf{r})$ (or refractive index) affects the dispersion of photons in the PhC and can lead to the development of a photonic band gap (PBG), where propagation is forbidden for photons in a specific frequency range. The development of a photonic band structure is similar in many ways to the electronic band structure of a semiconductor created when electrons propagate through the periodic potential of a crystal lattice. In addition to PBGs, the photonic band structure points to other interesting and useful optical phenomena in photonic crystals, including negative refraction, superprism effects, slow-moving light modes, and modified spontaneous emission.[94-97]

4.2 Dimensionality of Photonic Crystals

Photonic crystals can be fabricated in a variety of structures in one, two, or three dimension(s), 1D, 2D, and 3D, respectively. Schematic examples of these structures are shown in Figure 4.1.

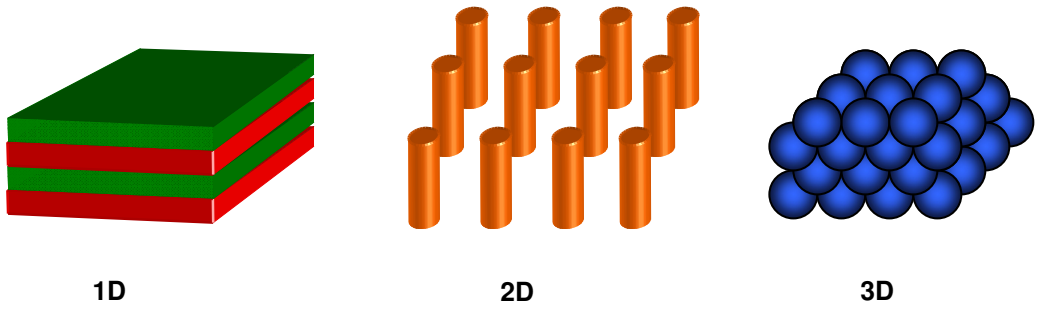

Figure 4.1: Schematics of 1D, 2D, and 3D photonic crystals.

The first demonstration of a photonic band gap occurred over a century ago when Lord Rayleigh fabricated a 1D periodic dielectric stack (Bragg mirror) that showed high reflectivity over a specific frequency range. The concept of a photonic crystal was not proposed until about 20 years ago in groundbreaking work by Yablonovich and John on the suppression of spontaneous emission[98] and the localization of photons[99] in 3D periodic dielectric structures. Since then, research on the theory and fabrication of photonic crystals has expanded rapidly. 1D PhCs, already extensively used in optical coatings, LED enhancement, and high-reflectivity laser cavities (e.g. vertical-cavity surface-emitting lasers or VCSELs), have given way to more advanced 2D and 3D structures. The development of planar 2D PhCs was facilitated by existing patterning and etching processes used in the semiconductor industry, making it relatively easy to design a PhC with a defect for planar waveguiding or microcavity lasing applications. Single-mode photonic crystal fibers[100], a hybrid 2D PhC, have recently become commercially available.

Despite fueling the explosion of interest in photonic band gap materials, the fabrication and utilization of 3D PhCs has proceeded at a more sedate pace than its 1D and 2D counterparts. 3D PhCs offer the most intriguing properties and most difficult fabrication challenges. A photonic crystal active in the visible spectrum requires features sized below the resolution of most microfabrication techniques, and early successes for 3D PhCs were limited to the microwave region.[101] New techniques, most notably self-assembly of monodisperse colloids, have evolved to allow fabrication of 3D ordered structures with the necessary feature size to produce a PBG in the visible light range.

4.2.1 Diffraction and Band Structure of Photonic Crystals

A basic understanding of a photonic band gap can be developed by an analogy to Bragg diffraction in a layered (1D) photonic crystal. Bragg diffraction describes the interference of electromagnetic waves or subatomic particles scattered from a periodic structure (e.g. x-ray diffraction). Photons of a wavelength similar to the periodic spacing between regions of differing refractive index will be scattered at the interfaces. The scattered waves will interfere constructively or destructively, depending on the phase shift upon scattering. Bragg's law describes the case of constructive interference.

$$m\lambda = 2dn_{eff}\cos(\theta) \qquad [4.1]$$

Photons scattered with a phase difference equal to an integer multiple (m) of the wavelength (λ) combine and are Bragg diffracted (reflected) from the crystal. θ is the angle of incidence, d is the spacing between layers, and n_{eff} is the effective refractive index. The value of n_{eff} can be estimated by:

$$n_{eff} = \phi_1 n_1 + \phi_2 n_2 \qquad [4.2]$$

where φ_1, φ_2 and n_1, n_2 are the volume fractions and refractive indices of the respective dielectric materials. Reflections from multiple layers lead to a photonic band gap as all photons at a certain wavelength are rejected from the structure. The center position of the band gap is determined by n_{eff}, while the width depends on the index contrast. The ratio of the width ($\Delta\omega$) to the center frequency (ω_c) is commonly used to determine the strength of the photonic system.[102]

The Bragg diffraction concept of photonic band gaps only applies for systems with index contrast ≈ 1. More complex geometries and larger index contrast materials (higher $\Delta\omega/\omega_c$) require more rigorous analysis using Maxwell's equations for EM waves:[103,104]

$$\nabla \times \mathbf{E}(\mathbf{r}) = i\left(\frac{\omega}{c}\right)\mathbf{H}(\mathbf{r}), \qquad \nabla \times \mathbf{H}(\mathbf{r}) = -i\left(\frac{\omega}{c}\right)\varepsilon(\mathbf{r})\mathbf{E}(\mathbf{r}) \qquad [4.3]$$

Here, ***E(r)*** and ***H(r)*** are the electric and magnetic fields as a function of position in an inhomogeneous dielectric medium, *ω* is angular frequency, *c* is the speed of light in vacuum, and ***ε(r)*** is the position-dependent dielectric constant. These can be simplified to:

$$\nabla \times \left(\frac{1}{\varepsilon(\mathbf{r})}\nabla \times \mathbf{H}(\mathbf{r})\right) = \left(\frac{\omega}{c}\right)^2 \mathbf{H}(\mathbf{r}) \qquad [4.4]$$

As ***ε(r)*** is periodic in a photonic crystal, 1/ ***ε(r)*** can be expanded to a Fourier series summed over the reciprocal lattice vector (**G**):

$$\frac{1}{\varepsilon(\mathbf{r})} = \sum_{\mathbf{G}} \kappa(\mathbf{G}) \exp(i\mathbf{G} \cdot \mathbf{r}) \qquad [4.5]$$

Here, κ(**G**) is the Fourier coefficient. Numerical solutions of Equation 4.4 for EM waves inside the photonic crystal determine the band diagram of allowed frequencies for a given direction, $\omega_n(\mathbf{k})$, over *n* bands. The calculated band structure for a ZnO inverse opal is shown in Figure 4.2a. Photonic crystals lack an absolute length scale and the physics governing their properties are therefore scalable with the lattice constant, provided ε(**r**) does not vary.[105] This allows the frequency to be expressed in normalized units of $a/\lambda = \omega/(2\pi c/a)$, where *a* is the lattice parameter. For inverse opal PhCs, $a = d_s\sqrt{2}$, where d_s is the sphere diameter. The x-axis of the band structure in Figure 4.2a is the wavevector, **k**, plotted along specific directions in the crystal. A schematic of the first Brillouin zone (BZ) and the high-symmetry points for an fcc structure are shown in Figure 4.2b. Each panel in Figure 4.2a corresponds to the allowed frequencies as **k** is swept along the BZ surface between two symmetry points.

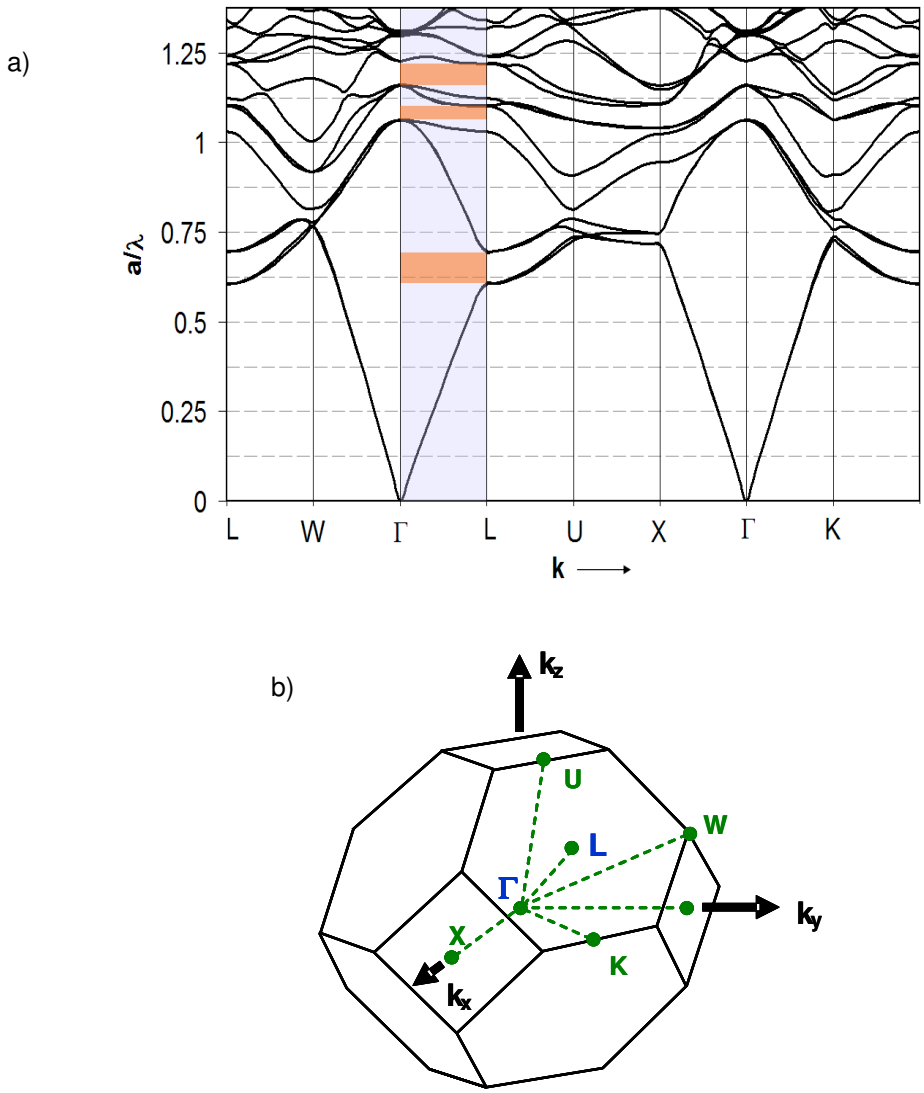

Figure 4.2: a) Band structure for a ZnO inverse opal plotted as normalized frequency (a/λ) versus the wavevector between high symmetry points in the b) first Brillouin zone of an fcc lattice. The pseudo-gaps in the ΓL direction are shaded.

The shaded band in the ΓL direction at a/λ ≈ 0.7 highlights the existence of a directional or pseudo-photonic band gap. In this region, there are no states available for photons to propagate. If such a band occurs over all directions, it is considered a complete or full photonic band gap. The existence of a full PBG in an fcc structure is partially limited by symmetry-induced degeneracy at the W point.[103] The diamond structure, which retains the fcc basis but removes the degeneracy, has been shown to exhibit

full PBGs at relatively low index contrast. Fabrication of a diamond structure is difficult, limiting its use. The inverted opal structure, an fcc array of air spheres in a dielectric lattice, is much easier to fabricate and has been shown to have a full photonic band gap for higher-order bands when a high-index material (e.g. silicon or germanium) is used.[106] The index contrast needed for a full PBG to appear in an fcc-based PhC is 2.8; only pseudo-gaps will exist for materials below this value.

The band structure contains other important information about the interaction of matter and light. Near **k** = 0 (Γ point in Figure 4.2a), the bands are roughly straight lines (free photon behavior) where $\omega = (c/n_{eff})k$. At the BZ edges, band repulsion bends the modes into increasingly more complex forms, and $n_{eff} = c/(d\omega/dk)$ instead of $n = ck/\omega$. In a 3D system, the dispersion line is replaced by a series of spheres that are deformed by band repulsion near the BZ edge. Slices of the deformed spheres taken at a specific frequency yield a dispersion surface. Energy is transferred through the PhC at the group velocity, given by the slope of the dispersion curve ($v_g = c/n_{eff} = d\omega/dk$). For the 3D case, the group velocity vector is given by:

$$\mathbf{v}_g(\mathbf{k}) = \nabla_{\mathbf{k}}\omega(\mathbf{k}) \qquad [4.6]$$

As a consequence of the k-gradient, the group velocity vector propagates normal to the dispersion surface. For a strongly distorted surface, this can lead to propagation in a direction different from the initial wavevector, which is the basis for many interesting phenomena in PhCs (e.g. superprism effect and negative refraction).[6] Additionally, examination of the band structure in Figure 4.2 shows that bands with high order, or close to the BZ edge, are quite flat, making $v_g \approx 0$. Light traveling in these bands is significantly slowed as it passes through the PhC, greatly increasing the degree of light-matter interaction.

4.3 Fabrication Techniques for 3D Photonic Crystals

Techniques for fabricating and simulating high quality three dimensional photonic crystal structures have been advancing at a rapid rate. The lattice constant of a photonic crystal determines its operation wavelength, and a size scale of 150 – 350 nm is necessary for the visible spectrum. The first

complete photonic band gap material was created in 1991 by Yablonovich (aptly called “Yablonovite”) using micromachining techniques to create a non-spherical fcc array of holes that overcame the W-point degeneracy issue.[101] Other microfabrication techniques have allowed for similar complete PBG structures in the infrared.[107] Resolution limits, scalability, and the labor-intensive nature of these techniques have restricted their use below this range.

The second type of 3D PhC structure is the “woodpile” structure, which is similar to the ideal diamond lattice. The woodpile structure is formed from a periodic stack of dielectric rods that are either micromachined or fabricated using layer-by-layer lithography-based techniques.[108,109] Again, applications of this process are limited by scale, time, and cost.

4.3.1 Self-Assembly of Colloidal Microsphere Opals

The limitations of the above 3D fabrication techniques have spurred the development of many new methods for creating large-scale 3D PhCs. Of these techniques, self-assembly of artificial opals from monodisperse, colloidal microspheres has become the most studied and utilized, due to ease of use and extensive commercial availability of a wide size range of silica, polystyrene (PS), and poly(methyl methacrylate) (PMMA) microspheres. These artificial opals mimic the opal structure commonly found in nature: domains of periodic, close-packed silica spheres in air.[110] The silica spheres are on the same size scale as visible light; thus, the periodicity introduces a pseudogap in the visible regime. Different orientations of these domains result in the multitude of colors often seen in opal gemstones, a phenomenon often mistakenly identified as “opalescence.” (The play of colors due to the presence of pseudogaps is a form of iridescence.)

Early self-assembled colloidal crystals were formed by sedimentation of microspheres from a suspension onto a horizontal substrate.[111] The settling rate of small spheres was very low, as gravity-forced sedimentation is opposed by Brownian motion of the suspension. The prevalence of defects such as stacking faults, dislocations, and grain boundaries limited the photonic utility of these crystals. New techniques have evolved to improve the quality of colloidal crystals, including confinement cells,[112]

Langmuir-Blodgett films,[113] and vertical convective self-assembly (VCSA).[114] Of these, vertical self-assembly is the most widely used and studied.

The VCSA method involves a substrate held vertically in a dilute suspension of microspheres. A meniscus is formed at the water/substrate/air interface. As the suspension evaporates, the meniscus sweeps down the substrate and strong capillary forces pull spheres to this interface, where they spontaneously self-assemble into a large fcc array with the (111) plane perpendicular to the substrate. The exact mechanism behind this phenomenon is still not well understood. Thermodynamics predicts the equilibrium packing for hard, non-interacting spheres should be fcc.[115] The energy difference between fcc and hcp packing is minimal, $\leq 10^{-3}$ $k_B T$ per sphere,[116] which would lead one to expect to see a mixture of fcc and hcp packing in the relatively short growth time (hours) for VCSA opals. Despite this, fcc is the predominant packing seen in these structures. Norris *et al.* explained the preferential fcc packing using convective flow through octahedral (open) and tetrahedral (obstructed) pores in the sphere layer.[116] Other groups have examined the nature of liquid bridges present in the growth front, which remain after the meniscus has passed[117] and the arrangement of the spheres as they get pulled into the meniscus.[118] Unlike traditional self-assembly, VCSA appears to rely on the meniscus shape and solvent flow rather than strict thermodynamic considerations. It is a robust technique that is easy to implement in a variety of forms.[119-123]

4.3.2 Infiltration of Opal Templates

Artificial opals are useful tools for studying photonic properties; unfortunately, they lack a complete photonic band gap.[6] A structure with a low filling fraction of high refractive index material is necessary to optimize the band structure, and inverse opals were developed to meet these requirements. A high index material is infiltrated into the pores of an artificial opal template, and the structure is then "inverted" by removing the spheres. The result is a periodic array of air spheres with a dielectric backbone, providing greater refractive index contrast. A schematic of the inverse opal fabrication process is shown in Figure 4.3.

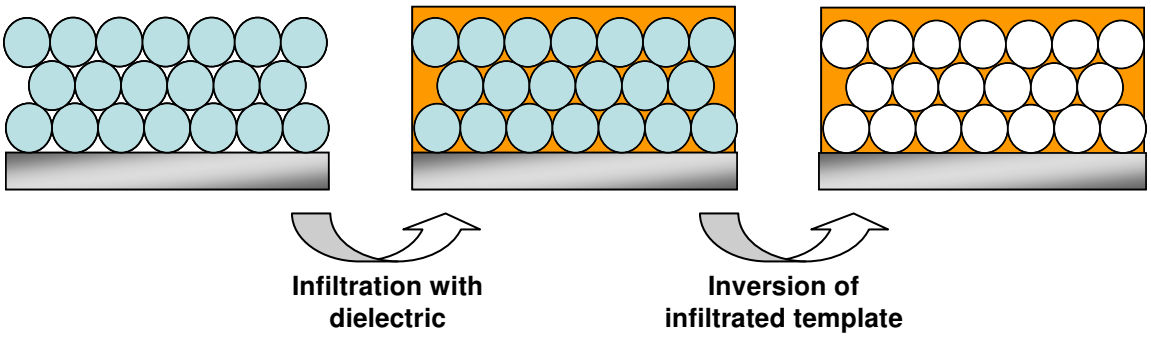

Figure 4.3: Schematic of the infiltration and firing steps used to fabricate inverse opal photonic crystals.

Considering the requirements needed to achieve a complete photonic bandgap (index contrast > 2.8), research of materials for use in inverse opal structures has focused on those with a high dielectric constant. Silicon and germanium are acceptable for the long wavelength spectrum, but inverse opals for the visible spectrum require high transparency in that region. Several materials have been used that meet these requirements including TiO_2,[124] ZnO,[125] and ZnS.[126]

A variety of techniques have been developed to infiltrate material into artificial opals (or other low-index sacrificial templates). They are typically either liquid or gas-phase processes. Liquid infiltration techniques include sol-gel infiltration[127], nanoparticle infiltration[128], and electrodeposition.[129] Liquid-phase techniques often suffer from low filling fractions and random distributions of porosity; however, they allow for the widest range of materials to be infiltrated, including polymers and metals. Gas-phase infiltration techniques include low-pressure chemical vapor deposition (CVD)[130] and atomic layer deposition (ALD).[125] These techniques have been traditionally used to infiltrate various semiconductor materials and have the best control over filling fraction, porosity, and material quality.

4.3.3 Atomic Layer Deposition

Atomic layer deposition is a CVD-type process that involves two self-limiting sequential binary reactions occurring between a gas and a surface. The basis for ALD was originally developed by Soviet researchers in the 1960's[131] and explored by Finnish scientists in the 1970's and 1980's as a technique to

fabricate thin film electroluminescent displays.[132] Commercial and experimental utilization of ALD has blossomed in the past two decades as devices are continually scaled down and structures become more complex. The major advantage of ALD is that material growth is surface-controlled versus source-controlled (e.g. CVD, MBE, sputtering), allowing for precise, sub-monolayer control of conformal coatings with complex shapes. A typical ALD growth cycle follows four basic steps:

1) Exposure cycle, yielding self-terminated chemisorption of the first (metal) precursor adatoms on the surface
2) Inert gas purge cycle to remove excess precursor, physisorbed reactant, and by-products from the first half-reaction
3) Exposure cycle of a second (non-metal) precursor, causing a self-terminating reaction with the initial (metal) precursor adatoms to form a layer of the desired material
4) Inert gas purge cycle to remove excess precursor, physisorbed reactant, and by-products from the second half-reaction

This process ideally yields a monolayer of material at the completion of steps 1-4. Heating the ALD reactor and substrate prevents excess condensation of the precursors and provides the activation energy for chemical reactions to take place at the surface. Process temperatures typically have an upper limit to prevent precursor decomposition.[131,133,134] These limitations form what is known as the ALD window, where the growth per cycle (GPC) remains constant over a range of temperatures. Ideally, ALD will grow one monolayer of material per cycle; however, in practice this is rarely the case.[131] A variety of situations limit the adsorption and reaction of precursors, including steric hindrance for large precursor molecules, decreased reactive surface sites, competing surface reactions, and secondary reactions with the surface reactive groups and reaction by-products.[131] The GPC is often not constant over the full ALD process and is affected by temperature and number of cycles.

4.3.3.1 Atomic Layer Deposition of ZnO

Growth of ZnO from the metalorganic precursor diethylzinc (DEZ) and water (H_2O) is characterized by the following two half reactions:[135]

$$Zn–OH^* + Zn(CH_2CH_3)_2 \rightarrow Zn–O–Zn–CH_2CH_3^* + CH_3CH_3 \quad [4.1]$$

$$Zn–CH_2CH_3^* + H_2O \rightarrow Zn–OH^* + CH_3CH_3 \quad [4.2]$$

* = surface species

A schematic of how these reactions occur in the framework of a full ZnO ALD cycle is shown in Figure 4.4. The volatility of DEZ allows this chemical reaction to take place at temperatures below the typical ALD window. The by-product for each half-reaction is ethane (CH_3CH_3), which vaporizes and is purged from the system with minimal reactivity toward other surface groups. Secondary reactions involving excess DEZ precursor molecules and Zn-CH_2CH_3 surface groups can lead to deposition of metallic zinc, decreasing the available active sites for reaction with H_2O. These reactions are typically much slower than those in Equations 4.1 and 4.2, and can be minimized with short pulse cycles.[102]

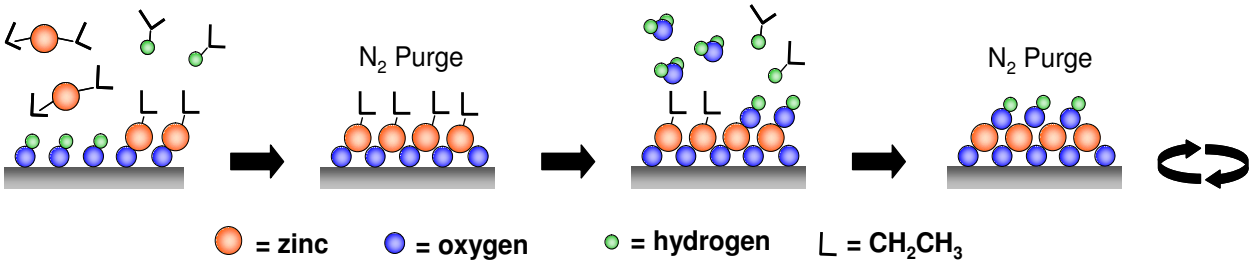

Figure 4.4: Schematic of the half-reactions that occur during the ZnO ALD process with DEZ and H_2O as precursors.

4.3.3.2 ALD for 3D Photonic Crystals

ALD has grown an amazing variety of oxides, nitrides, semiconductors, and metals.[131] The ability to coat complex and high aspect ratio structures makes ALD ideally suited for inverse opal fabrication; ZnO,[125] TiO_2,[124] ZnS,[126] Al_2O_3 and VO_2[136] inverse opals have been fabricated by ALD. The major drawback of ALD-based infiltration is the fill fraction limit imposed by the opal template geometry. Conformal coating of the spheres is limited by closure of the narrowest pathway through the opal

template. In an fcc-packed opal this corresponds to the space between three spheres in the (111) planes. Geometry dictates that the thickest possible coating *inside* the opal will be 7.75% of the sphere diameter.[102] When these pathways close, additional ALD cycles will only grow material on the top surface, forming a cap layer. Partial air pores are left in the tetrahedral and octahedral interstitial points of the structure, with a maximum infiltration of about 86% of the total available volume. Recently, King *et al.* demonstrated a two-step technique for increasing the degree of infiltration in TiO_2 inverse opals.[137] The opal template is heavily sintered to reduce the pore volume between spheres and increase the windows at sphere contact points. After infiltration and inversion, the inverse opal is backfilled with additional TiO_2 to form a non-close-packed structure with excellent photonic band gap tunability.

The presence of interstitial pores in an inverse opal affects the photonic band structure on two fronts. First, the pores will slightly decrease the average refractive index of the structure by increasing the volume fraction of air versus the dielectric. Second, the periodic positioning of the pores means they act as a photonic substructure, mainly causing flattening in high order bands.[138] Studies on silicon inverse opals have shown that both incomplete infiltration (with interstitial pores) and the windows formed during sintering can have a dramatic impact on the full gap that appears between the eighth and ninth bands.[106]

4.4 Plasmonic Effects in Metal Nanoparticles

Plasmonics, like photonics, is a field that has seen a dramatic increase in interest in the past several decades. Plasmons trace their roots back many centuries to medieval artisans and glassmakers, who unknowingly utilized plasmonic effects from nanoscale metal particles in stained glass.[139] Plasmons are the quanta of collective oscillations in an electron gas at optical frequencies in a metal.[37] Most metals can be described as a system of free, mobile conduction electrons and fixed positive ions (a plasma). When the metal is excited by E-M radiation, the electric field causes the free electrons to coherently oscillate at the plasma frequency, ω_p:[140]

$$\omega_p = \sqrt{\frac{ne^2}{\varepsilon_0 m_e}} \qquad [4.7]$$

Here, ε_0 is the dielectric constant of vacuum, e and m_e are the charge and mass of an electron, and n is the electron density. The equation above describes the plasma frequency for a bulk metal. Since light will not penetrate far into a metal, it is convenient to consider the oscillations of electrons at the surface, called surface plasmon polaritons (or often just surface plasmons - SPs). At a continuous metal-vacuum interface, the surface plasmons can propagate as a longitudinal surface charge density wave.[140] Metals with finite volume, such as metal nanoparticles, support localized surface plasmons that do not propagate. An E-M wave excites the electrons away from the metal, in essence creating two overlapping spheres of opposite charge (ions and electrons), as shown in Figure 4.5.

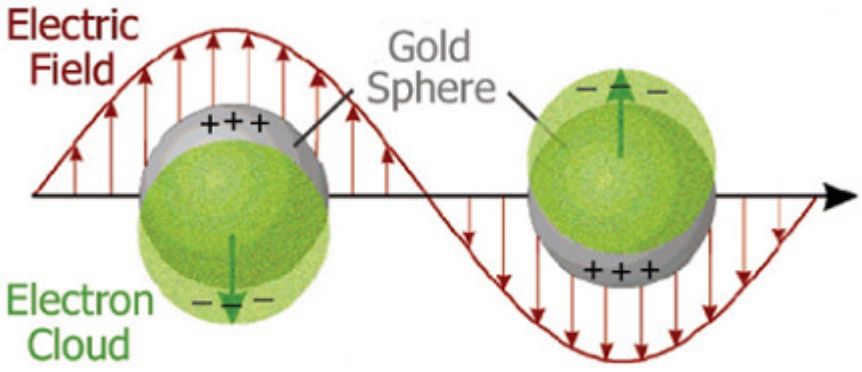

Figure 4.5: Schematic of the collective electron oscillation induced by an E-M wave in gold spheres. The shape and volume of the particles prevents propagation of the surface plasmon modes. Adapted from Xai *et al.*[140]

The charge differential creates a large, local E-field that drives the electrons back to their original positions. This process has a resonant frequency of:

$$\omega_p^{LSP} = \frac{\omega_p}{\sqrt{3}} \qquad [4.8]$$

Shifts in the localized SP peak position can be induced by changing the local refractive index or by coupling of SP modes in agglomerated nanoparticles. This phenomenon has been exploited to produce sensors for small molecules and DNA.[140] Surface plasmon resonances appear in optical spectra as absorption peaks, as light at the plasmon frequency is absorbed to excite the SP modes. The position and number of localized SP modes is highly dependent on the size and shape of the metal nanoparticle.

Surface plasmons have also been used to enhance the emission efficiency of fluorescent and luminescent emitters, such as dyes, quantum dots, or quantum wells.[141-143]
It is believed that this effect is due to a high local density of states when the emitter is near a metal surface or nanoparticle. Fermi's golden rule states that the probability of transition (emission) depends upon the coupling between the initial and final states as the matrix element of the coupling squared. Thus, the emission rate increases dramatically with the strength of the perturbation (the SP mode).[144]

4.5 Metal-Dielectric Photonic Crystals

In recent years, many researchers have sought to combine the plasmon resonance of metallic nanoparticles with the unique properties of 3D photonic crystals. These structures fall into four basic categories: 1) opals doped with varying levels of metallic nanoparticles,[145,146] 2) inverse opals with a mixed dielectric/metal backbone,[128,147] 3) inverse opals doped with metallic nanoparticles,[148,149] and 4) opals assembled from metal-coated dielectric spheres.[150,151] Photonic crystals doped with low levels of metal nanoparticles typically show a PBG that is shifted due to the additional index contrast from the metal. At higher doping levels, SP resonance peaks start to appear along with the diffraction peaks from the opal structure. Photonic crystals assembled from coated spheres have even more complex optical spectra, as splitting occurs in the SP modes. Metal-coated sphere opals have generated much interest as they have been theoretically proposed to have full photonic band gaps in the visible spectrum.[152] Metal-dielectric photonic crystals have shown promise as highly tunable PBG structures and as biomaterial and refractive index sensors.

Section 5: Fabrication of ZnO Inverse Opal Photonic Crystals

5.1 Vertical Convective Self-Assembly of Polymer Opal Templates

Opal templates were fabricated using the vertical convective self-assembly technique developed by Jiang *et al*. for growing high quality, well-oriented colloidal films over large areas.[114] Monodisperse, colloidal carboxylate-modified polystyrene (CM-PS) microspheres with sizes ranging from 183nm to 424nm were purchased from Seradyn, Inc. The spheres had a <3% coefficient of variation. The CM-PS microspheres had acrylic acid copolymerized with the styrene monomer to leave carboxyl groups attached to the surface of the particle, giving it a strong net negative charge, a hydrophilic surface, and covalent coupling sites for a variety of molecules, including ALD precursor molecules. Previous experiments on ALD infiltration of PS microsphere opal templates has shown that the carboxyl groups allow for better initialization, or "seeding", of a dense ZnO film on the sphere surface.[125] The amount of carboxyl groups on the surface of the CM-PS microspheres is measured by the "parking area" (PA) which denotes the amount of surface area occupied by a functional group. A small PA therefore indicates a high density of carboxyl groups on the microsphere surface.

Standard glass microscope slides were used as substrates for the opal templates. The glass slides were cut in half both lengthwise and widthwise, yielding four identical 1.5 in x 0.5 in pieces. These pieces were cleaned by sonication for 1 hour in 1% cleansing Alconox solution, or by a 5 minute etch in a 4:1 (H_2O_2:H_2SO_4) piranha solution. Both treatments resulted in a highly hydrophilic substrate surface. The substrates were rinsed with high-purity MilliQ deionized (DI) water and dried with nitrogen. The colloidal microspheres were diluted with high-purity MilliQ DI water to final volume fractions in the range 0.1% - 0.3%. These suspensions were placed in 7 dram glass vials that had been pre-cleaned by sonication in a 1% cleansing solution for 1 hour, and the suspensions were then sonicated to disperse the microspheres. The substrates were added to the vials with a clip at the top to hold them roughly vertical in the center of the vial. The vials containing the colloidal suspensions and substrates were placed in a vibration-damped drying oven at 50^{o}C for about 60 hours. As the water slowly evaporated, convective and capillary forces

at the meniscus pulled microspheres from the suspension to self-assemble into an fcc structure at the interface. This process is shown in Figure 5.1.

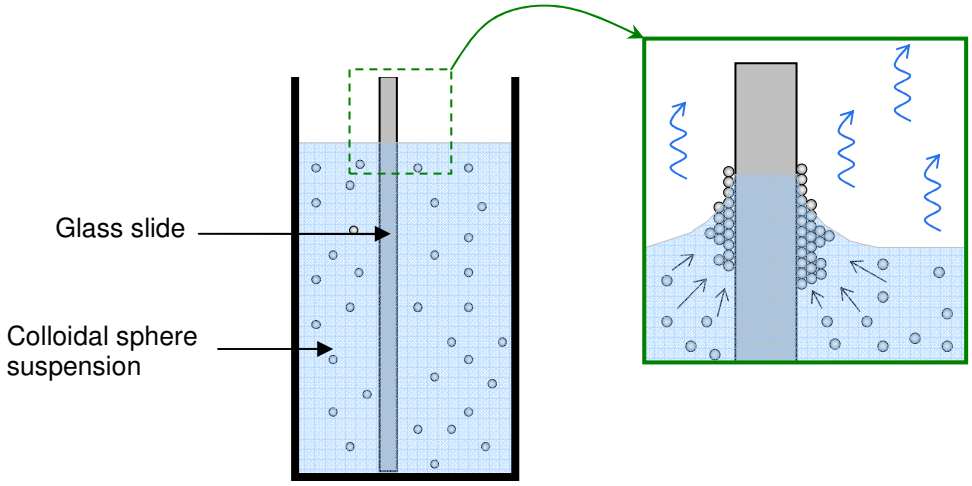

Figure 5.1: Schematic of the vertical convective self-assembly process. As the colloidal suspension evaporates, the meniscus sweeps down the vertical substrate. Spheres flowing to the meniscus self-assemble into an fcc-packed opal.

After the colloidal suspension completely evaporated, an opal template remained on the glass substrate. Due to the vertical placement of the glass substrate in the suspension, opals were generally deposited on both sides of the glass. Typically, there was a high quality opal with excellent coverage on one side and sparse coverage on the "back" side. The back side of the substrate was scraped clean with a razor blade and wiped with acetone to remove any residual polymer microspheres prior to infiltration. This inhibited the formation of a second inverse opal on the back side of the substrate and ensured that the observed optical properties were restricted to the single inverse opal structure on top.

5.2 Infiltration of Opal Templates via ALD

The opal templates were infiltrated with ZnO using a flow-type ALD custom-built and modified for this purpose.[153] Figure 5.2 is a schematic of the component layout. Nitrogen flows from a tank to a reservoir before passing into two separate lines for each bank of precursors. Mass flow controllers (MFCs) maintain the flow of nitrogen through the system. The system has ports for six total precursor

vials, three on each line. The valves and tubing are enclosed in an insulated box heated to 120^{o}C to prevent condensation of precursor molecules. The separate precursor lines join together at the chamber. Inside the chamber there is a raised stage that is heated to control substrate temperature during deposition. The chamber is enclosed in another insulated box that is heated during operation. A plate in front of the chamber inlet diffuses the precursor gases throughout the chamber and protects the substrates from being locally cooled by direct exposure to the nitrogen flow.

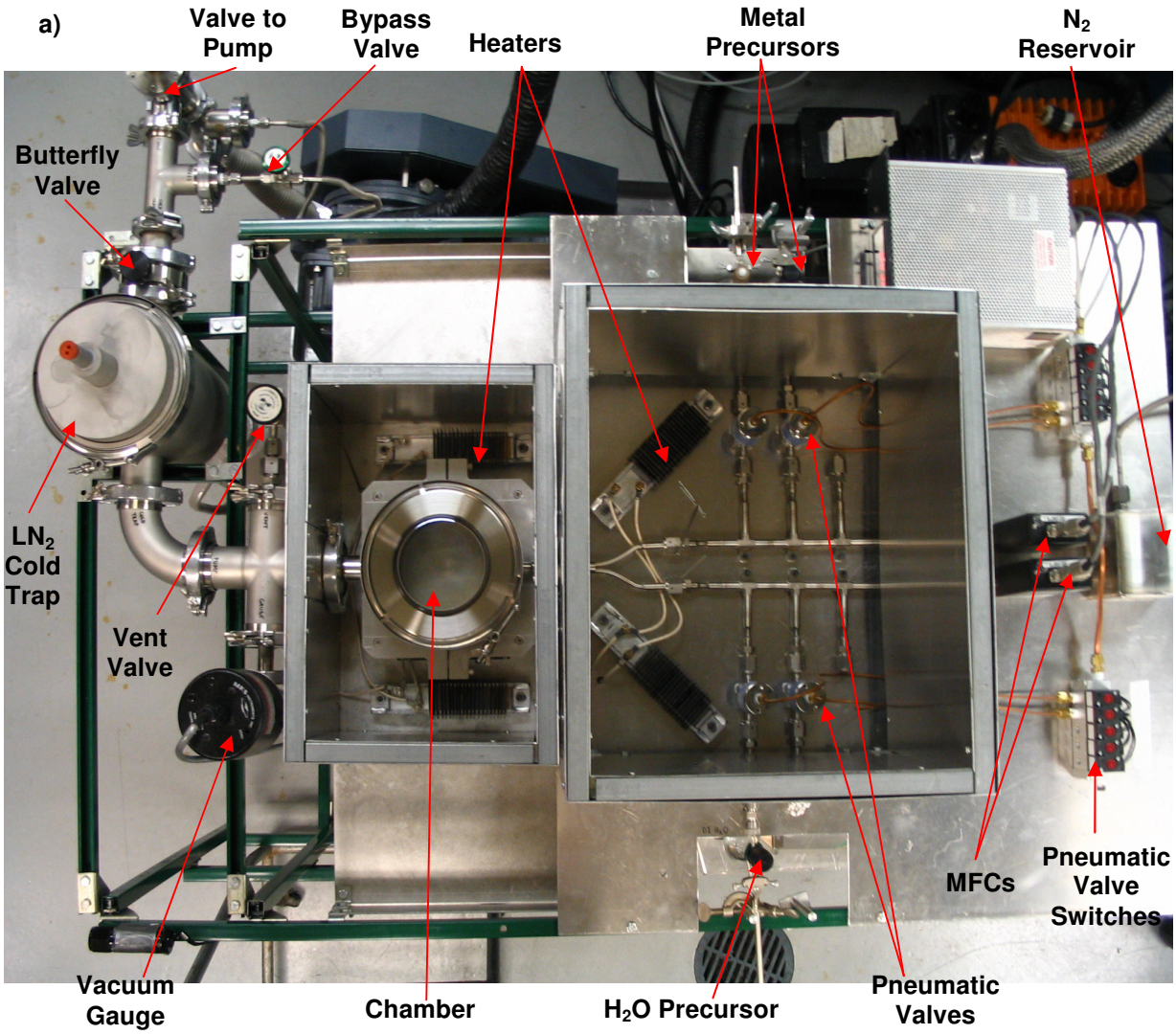

Figure 5.2: a) Overhead view of the custom ALD system used to infiltrate opals with ZnO. b) Schematic of valves and flow in the ALD system.

After the chamber there is a Baratron vacuum gauge used to set the chamber pressure. This gauge has a heating element to help prevent precursor condensation. A liquid nitrogen cold trap condenses excess precursor in the nitrogen flow so it does not reach the vacuum pump. Past the cold trap there is a butterfly valve used in conjunction with a vacuum bypass needle valve to set the chamber pressure. The precursors used for ZnO infiltration are high purity water and diethylzinc. Table 5.1 summarizes the parameters used to infiltrate opal templates with ZnO in the ALD system.

Table 5.1 – Parameters used for infiltrating ZnO polymer opal templates.

Flow Rate of UHP N_2	50 sccm
Chamber Pressure	5.4 Torr
Substrate Temperature	80 ^oC
Chamber Temperature	75 ^oC
Metalorganic Exposure Time	1 s (DEZ)
DI Water Exposure Time	1 s
N_2 Purge Time	20 s
Precursor Temperatures	Ambient
Number of Cycles	100

The prepared opal templates were placed in the chamber away from the edges of the heated substrate plate. The chamber was then pumped down to the base pressure, approximately 25 mTorr. The substrate plate reached operating temperature within 5 – 10 minutes, but the insulated box around the chamber took about 60 – 70 minutes to reach the temperature setpoint. This allowed the templates to be sintered for approximately 1 hour prior to infiltration. The substrate temperature was initially set at 80^oC to stay below the T_g of PS (~95 ^oC) and prevent deformation of the microspheres prior to infiltration. Film thickness and growth rate were determined by spectroscopic ellipsometry (SE) analysis of thin films grown on silicon during an opal infiltration.

The current configuration of the ALD system also allowed for deposition of Al_2O_3. Polymer microsphere opals could not be infiltrated with Al_2O_3 due to the temperatures necessary for deposition to occur (>120 ^oC). However, there were no such limitations on the final inverse opal structure. Thin

coatings of Al_2O_3 were deposited on the surfaces of ZnO inverse opals as passivation or protective layers. The growth of Al_2O_3 by ALD was similar to ZnO. The precursors were trimethylaluminum (TMA) and high purity DI water, and the growth recipe was the same as that for high temperature ZnO.

5.3 Inversion of Infiltrated Opal Templates

Infiltrated opal templates were inverted by firing at high temperature in air to remove the polymer microspheres. The result was an inverse opal with air voids and a dielectric backbone. Thermogravimetric analysis (TGA) was used to determine the temperatures sufficient to remove the PS template. In addition to firing in air, opals were inverted by firing in a nitrous oxide atmosphere in an attempt to remove the polymer more quickly. Grain growth was measured by scanning electron microscopy (SEM) and X-ray diffraction (XRD). A typical firing recipe is described in Table 5.2.

Table 5.2 – Typical firing parameters for inverse opals.

Atmosphere	Air
Room temperature – 150 ^{o}C (ramp)	1 hour
150 ^{o}C – 450 ^{o}C (ramp)	1 hour
450 ^{o}C (hold)	2 hours
Cool to room temperature	Cool in furnace

5.4 Structural Characterization Techniques

The thickness, infiltration, grain size, and ordering of ZnO inverse opal samples was most often examined by SEM. A Hitachi S-4800 FE SEM and a LEO Gemini 1525 FE SEM were used interchangeably for imaging purposes. Both instruments use low (or ultra-low in the case of the S-4800) accelerating voltages during imaging, making conductive coatings generally unnecessary. For cross-sectional analysis, the inverse opal samples were cleaved using a diamond scribe on the back side of the glass substrate. The sample was then mounted on a sample stud that had been cut in half, with the cleaved surface facing up. Cross-sectional samples allowed for easy thickness measurements and a view of the interior of the inverse opal. Cleaving often caused the inverse opal to fracture unevenly along domain crack boundaries

as well as through domains at odd angles. Thus, it was often difficult to determine the degree of ordering in the samples. To better image the inverse opal structure, the cap layer of ZnO was removed using reactive ion etching (RIE). After the RIE process, it was possible to see "into" the inverse opal for a few layers through the holes formed where microspheres were sintered together prior to infiltration.

5.4.1 Reactive Ion Etching

A Plasma Technology Plasmalab µP system was used for RIE processing of the ZnO inverse opals. The system utilizes a radio frequency electromagnetic field to excite a gaseous etch medium into a plasma. Ions in the plasma strike the surface and react with the material there to etch it away. RIE provides a way of gently removing the top layer of ZnO from the inverse opal with minimal structural damage. A mixture of methane (CH_4) and hydrogen (H_2) was used for plasma etching. The etching process is comparable to running the ALD reaction in reverse. CH_x radicals in the plasma react with the Zn to form metalorganic molecules; likewise, the hydrogen ions in the plasma react with oxygen at the surface to form water. The species are volatile enough to vaporize and are pumped away. It is important to control the ratio of CH_4/H_2 as an excess of CH_x radicals can result in polymer buildup and poor etch quality.[154] To prevent polymer buildup, short CH_4/H_2 etches were alternated with O_2 etches. Table 5.3 lists the parameters used for RIE of the inverse opals.

Table 5.3 – Recipe for RIE of the top surface of ZnO inverse opals.

Parameter	**CH_4/H_2 etch**	**O_2 etch**
Power	200 W	150 W
Chamber Pressure	185 mTorr	100 mTorr
Gas Flow Rates	10 sccm / 81 sccm	100 sccm
Duration	2 min	2 min
Number of Cycles	2.5	3
Total Etch Time	5 min	6 min

5.5 Optical Characterization Techniques

The true measure of quality in a photonic crystal is in its optical properties. A variety of techniques have been used to examine the photonic properties of the various ZnO inverse opals samples. These techniques examined the photonic band gaps of the inverse opals, the photon emission of the ZnO, and the depth of interaction between the two.

5.5.1 Transmission and Reflection

Transmission and reflection are common techniques for observing the presence of photonic band gaps in the inverse opals. Both spectra were measured on a Cary UV-Vis-NIR spectrophotometer equipped with a diffuse reflectance accessory (DRA). A white light source was passed through a monochromator to select a specific wavelength. For transmission measurements this light was split into a sample and reference beam to strip any variations of the light source out of the spectrum. A baseline of the substrate was taken so that the measured transmission spectrum displayed only properties of the inverse opal. The samples were oriented such that the beam passed through along the [111] direction (surface normal) of the inverse opal. A dip in transmission appeared when a photonic band gap was present, as light of that wavelength could not propagate through the inverse opal. Thicker sections of the inverse opal scattered and absorbed more light, making it difficult to measure the photonic band gap for these sections. The electronic band gaps of ZnO and TiO_2 were in the near-UV range, so any spectral features due to high-order band gaps were suppressed.

Reflectivity was used to generate a clear picture of the photonic properties of inverse opals, regardless of thickness. The sample mount had two settings for measuring diffuse (scattered) reflectivity and total (diffuse + specular) reflectivity. Specularly reflected light was tightly reflected around the angle of incidence (mirror-like reflection). Diffuse reflected light was scattered from roughness, defects, etc. at multiple angles and was collected by reflections off the integrating sphere. The inverse opals were mounted to the DRA sphere such that the [111] direction was pointing almost directly inwards (~3^o off normal). Specular reflectivity spectra were taken by subtracting the diffuse reflectivity from the total reflectivity. Photonic band gaps appeared as peaks in reflectivity, as incident light at that wavelength

cannot pass through the sample. The effect of band edge absorption in the near-UV was minimized; so it was possible to see reflectivity peaks from high order band gaps that were normally not visible in transmission spectra.

5.5.2 Angle-Dependent Reflectivity and Photoluminescence

Angle-dependent reflectivity and photoluminescence were used to measure the behavior of photonic pseudogaps compared to the calculated band structure. For both types of measurements, the inverse opal was mounted in the center of a goniometer stage with a detection arm mounted on the perimeter.[155] A schematic of the reflectivity measurement configuration is shown in Figure 5.3. A collimated white light source (UV-enhanced Xe lamp) was focused on the sample with a lens (L1) at an angle of incidence θ from the [111] surface normal direction. The spot size on the sample was approximately 1mm in diameter. Light reflected off the sample was collected with a second lens (L2) and focused on an optical fiber bundle connected to a spectrometer. A linear polarizer (P) between the fiber and L2 allowed for measurement of *s*- or *p*-polarized light. Scans were typically taken from 5^{o} to 60^{o}, with an angular resolution of 5^{o} and a specular resolution of 1 nm. Reflectivity from the surface normal could not be measured, as the detection arm would block the incident light. Raw reflectivity data was normalized by removing the effects of the Xe lamp spectrum.

Angle-dependent photoluminescence was taken in a similar configuration, as shown in Figure 5.3b. In this geometry the inverse opal was fixed in position with the [111] surface normal at $\theta = 0^{o}$. The sample was pumped with the 325 nm line of a He:Cd cw laser or a 405 nm diode laser. The He:Cd laser excited ZnO above the band gap (~378 nm) and the diode laser was used to pump luminescent materials inside the inverse opal without exciting the ZnO. The angle of incidence of both was fixed to $\theta_p = 30^{o}$.

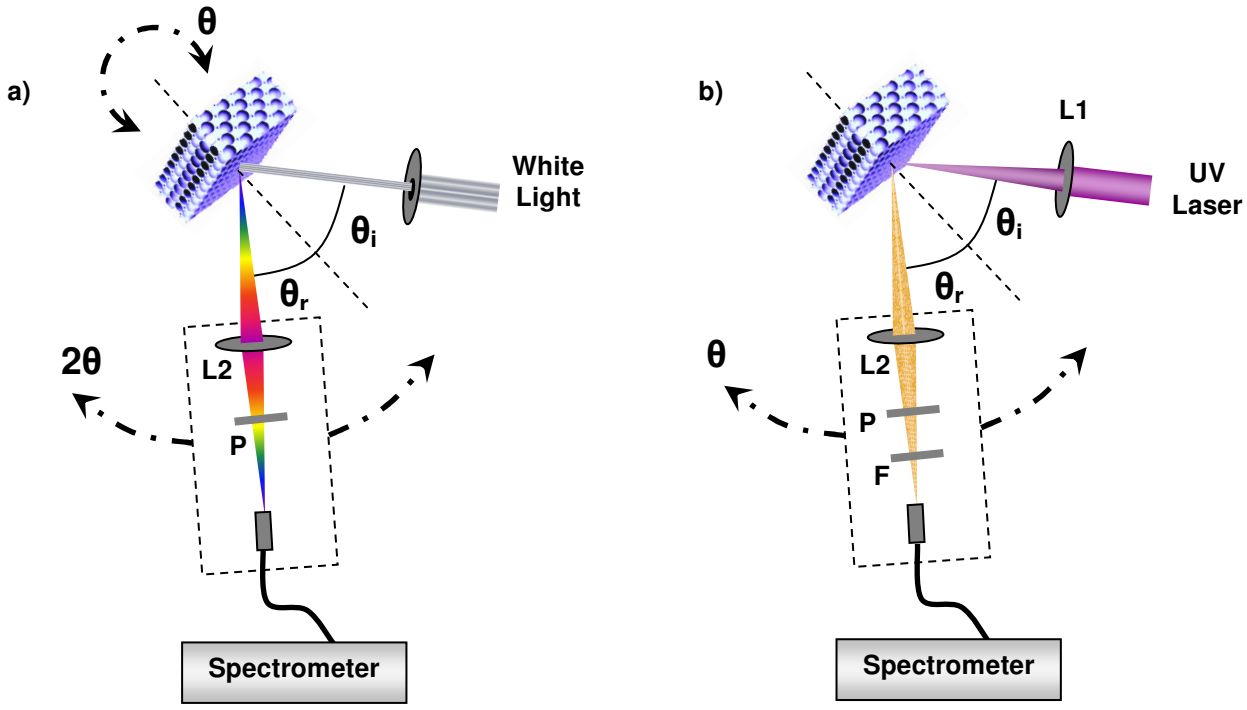

Figure 5.3: Optical setup for measuring angle-dependent a) reflectivity and b) photoluminescence from inverse opals. Reflectivity was measured in the θ-2θ geometry.

Emission of light at different angles *θ* was measured by scanning the detection arm. To prevent detection of the pump light, the incident plane was vertically offset from the detection plane. Additionally, a filter (F) was placed after the polarizer blocks to pump light scattered by the sample into the detection plane. Angle-dependent reflectivity and PL measurements could be taken both by manual rotation of the goniometer stage or by utilizing a computer-controlled motor linked with the spectrometer software. Raw PL data was normalized to remove the effects of variable integration time. The PL regime was characterized by a linear dependence of luminescent peak intensity with excitation power. The He:Cd laser output was attenuated to prevent amplified spontaneous emission in the ZnO inverse opals.

5.5.3 Spectroscopic Ellipsometry

A SOPRA ES-4G spectroscopic ellipsometer (SE) was used to determine the thickness of films deposited under various conditions in the ALD. Measurements of thickness combined with total number of cycles allowed for an estimate of the growth rate per cycle in the ALD. The same system was used for

characterization of CuCl films. Films for ellipsometry analysis were concurrently grown during opal infiltrations by placing a degreased silicon substrate in the chamber. Data fitting for each material was accomplished using a Cauchy law polynomial model in the WinElli program.

5.6 Infiltration of Inverse Opals

The porous structure and high surface area of inverse opal photonic crystals makes them excellent candidates for infiltration of liquids and gases. Inverse opals were infiltrated with semiconductor quantum dots and metallic nanoparticles and the modified optical properties examined.

5.6.1 Infiltration of CdSe/ZnS Quantum Dots into Inverse Opals

CdSe/ZnS core-shell QDs with emission wavelengths of 540 nm, 560 nm, 580 nm, and 600 nm were purchased from Evident Technologies, Inc. They were infiltrated into ZnO inverse opals by soaking in a diluted solution of QDs. Inverse opal samples to be infiltrated were generally 10 mm x 10 mm. Each sample was tacked to a piece of microscope slide and cut to fit vertically in a sealed 1 dram glass vial. The inverse opal was oriented such that the long domain cracks running along the growth direction were vertical when it was placed in the vial. Stock QD solution was diluted in toluene to 10^{-7} M prior to soaking, to prevent losses due to excess build up.[94] After a 24 hour soak, the inverse opals were removed and rinsed with toluene. They were then placed in a vial of fresh toluene for ~5 minutes under gentle agitation.

5.6.2 Confocal Fluorescence Microscopy

The extent of quantum dot infiltration in inverse opals was examined using a Leica Confocal Laser Scanning System (Leica Microsystems, Inc.). Only the 10x and 20x air objectives were used, as the higher-magnification oil-immersion objectives may have affected the QD distribution. The quantum dots were excited using the 457nm line of an Ar-laser. Transmitted light and fluorescent light channels were imaged simultaneously in z-series through the thickness of the inverse opal samples. A second detector was set to the QD emission wavelength to determine infiltration homogeneity.

5.6.3 Synthesis of Silver and Gold Nanoparticles

Silver and gold nanoparticles (AgNPs and AuNPs) were infiltrated into ZnO inverse opal samples as plasmonic materials and as seed layers for additional metal deposition. Colloidal gold nanoparticles (~5 nm diameter) were purchased from Sigma-Aldrich Co., and silver nanoparticles (~5 nm diameter) were synthesized by reduction of silver nitrate ($AgNO_3$) in solution.[156] A second set of parameters was also used to fabricate larger silver[157] (12 nm) and gold[158,159] (15 nm) nanoparticles with similar optical properties. All recipes were based on the reduction of metal ions from solutions of $AgNO_3$ and $HAuCl_4$. The 5 nm Ag and 15 nm Au nanoparticles were generally utilized for inverse opal infiltration experiments. The particles were stabilized in solution by electrostatic repulsion due to surface charges.[160] The windows between air spheres, created by contact points between adjacent spheres, generally ranged from 50 nm to 70 nm for the sphere sizes and sintering times used during template fabrication. The smaller particles were less likely to become trapped in and obstruct these passages. Both AgNP and AuNP solutions could be stored in the dark for several months at ~ 4^{o}C. The AgNP solution was especially sensitive to light; prolonged exposure to fluorescent light caused the nanoparticles to coalesce into nanoprisms, causing a subsequent shift in plasmonic resonance(s).[161] The size distribution of the metal nanoparticles was measured using the scanning transmission electron microscopy (STEM) mode on the Hitachi S-4800 FE SEM.

5.6.4 Infiltration of Metal Nanoparticles into ZnO Inverse Opals

Metal nanoparticles were placed inside ZnO PhCs by soaking RIE-processed inverse opals in the AuNP and AgNP solutions described in the previous section. The ZnO surfaces of the air spheres were functionalized to provide attachment sites for the nanoparticles, facilitating denser, more homogeneous coverage. The high temperature inversion and RIE processes invariably damaged the hydroxylated surface present from the final half-reaction in an ALD growth cycle. To restore the surface hydroxylation the inverse opals were exposed to a saturated water vapor atmosphere for 15 minutes. Following the hydroxylation step, the inverse opals were placed in a 1:4 solution of 3-aminopropyltrimethoxysilane (APTMS) and methanol for 15 - 30 minutes. The silane-terminated end of the APTMS molecule reacts

with the hydroxyl group on the ZnO, extending the amino groups outwards.[162] After silanization, the inverse opals were rinsed with methanol and water to remove excess APTMS from the sample. AuNPs and AgNPs were attached to the surfaces of the inverse opal by soaking in the citrate-stabilized solutions for 1 – 4 hours. The negatively charged citrate ions were bound with the amino groups on the ZnO surfaces. A polyelectrolyte, 2% poly(diallyldimethylammonium chloride) (PDDA), was also used to functionalize ZnO inverse opals. PDDA dissociates in water into Cl^- ions and a positively charged polymer chain. The chain binds with the OH^- groups on the ZnO surface and the negative citrate shells on the metal nanoparticles.

5.6.5 Additional Growth of Metal Nanoparticle Seeds

The AuNPs and AgNPs were also used as seeds to fabricate larger metal nanoparticles with different plasmonic properties. Additional growth of the seed particles was accomplished by adding additional metal ions to the nanoparticle suspension (either $AgNO_3$ or $HAuCl_4$) followed by addition of reducing agents.[163] The degree of nanoparticle growth was controlled by the amount of metal ions added. A similar process could be used to grow AuNPs and AgNPs already infiltrated into ZnO inverse opals. It was adapted from common techniques used in fabricating metal-nanoshells on silica spheres.[140,160,164,165] Inverse opals that have been infiltrated with AuNPs or AgNPs were placed in solutions containing either gold or silver ions. A reducing agent was then added to the solution to reduce the Au and Ag ions into metallic Au and Ag on the metal seed particles on the ZnO surface. Recipes for fabricating metallic nanoshells typically utilized a slow reducing agent to start the reduction process, followed by a drastic increase in pH to speed up the reaction. Growth of metal NPs inside inverse opals required the use a slow reducing agent to prevent excessive silver growth on the inverse opal surface.

Section 6: Structural and Optical Characterization of ZnO Inverse Opal Photonic Crystals

6.1 Polymer Microsphere Opal Templates

The VCSA process was used in previous work to grow a robust range of PS and PMMA opal templates.[102,153] The concentration of the initial suspension of spheres was varied depending on the sphere size and desired thickness range (typically between 20 - 60 layers). As the opal dries, 2-4 μm wide cracks appear, formed by shrinkage of the spheres as they lose water, and by the strong surface tension at the meniscus/opal interface. This process results in the formation of domains that are typically 40-70 μm in width and 80-150 μm in length, with the long dimension of the domains running along the growth direction. Sphere ordering is generally well-preserved across domain-crack boundaries. The domain size also varies along the growth direction; small domains appear in the initial thinner portions of the opal and gradually become larger as the opal grows thicker, consistent with previous studies.[166] It was proposed that thicker opals with large (up to 1000 μm x 500 μm) domains would improve the optical properties by reducing light scattering at the boundaries. Unfortunately, this is balanced by an increase in scattering due to stacking defects and surface disorder in thicker opals. Figure 6.1 shows optical micrographs of the domains formed at different positions along an opal.

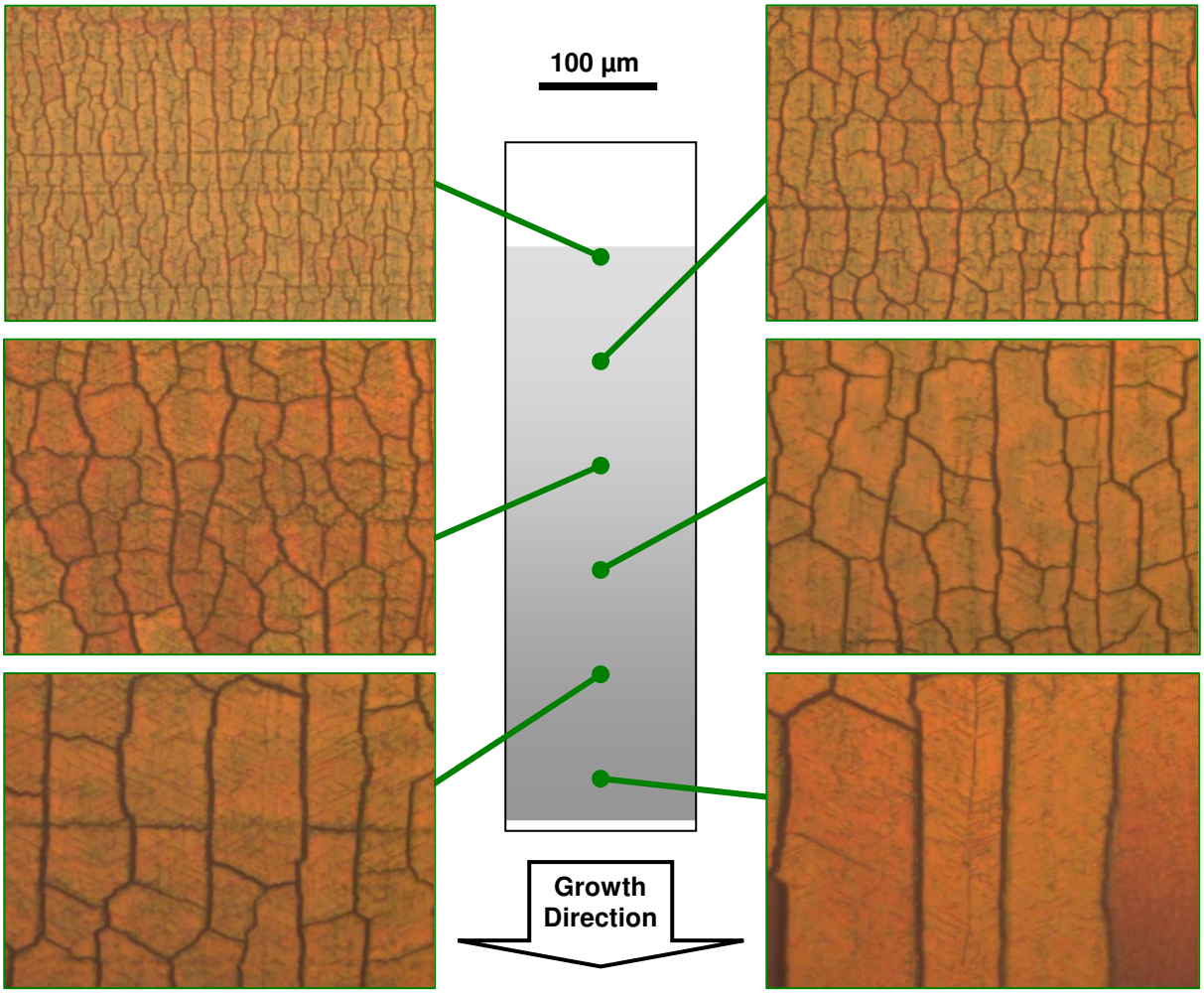

Figure 6.1: Optical micrographs showing the increase in domain size along the growth direction of a 375 nm ZnO inverse opal (shaded region). The opal thickness also increases along the growth direction.

Water loss during drying results in shrinkage of the PS spheres that make up the opal. Analyses of sphere size in opal templates and inverted opals reveal that sphere diameters decrease by approximately 10-15% for PS during the opal assembly process. Therefore, an inverse opal fabricated from 311nm PS spheres will actually result in an inverse opal with ~278 nm air spheres. Any calculations made involving the sphere size (band structure, etc.) must account for this size difference. In this thesis, all inverse opals are labeled by the initial sphere size rather than the shrunken sphere size.

A typical opal template can be divided into three sections: 1) the thin initial growth region where mono- and bi-layer growth mechanisms transition to multiple layers, 2) the middle region that contains

enough layers to support well-defined photonic properties, and 3) the final growth region where the meniscus shape is affected by proximity to the bottom of the vial, and the opal is thickest and least stable. The sections comprise roughly 10%, 60%, and 30% of the opal, respectively. The second section has the best optical properties and is easily distinguished by homogeneous coloring under direct light.

The carboxyl-groups attached to the spheres also had an effect on opal template quality. The parking area was different for each sphere size and varied from 17 Å^2 to 60 Å^2 (low PA denotes high carboxyl-content). Opals assembled from spheres with a PA < 30 Å^2 were generally more uniform and well-ordered across the whole substrate. Spheres with PA > 30 Å^2 had a tendency to have thickness and orientation variations across the width of the opal, as well as issues with meniscus pinning during assembly. When the meniscus stuck during assembly, it left behind a rippled area in the crystal. Subsequent pinning processes could produce uneven surfaces along the entire opal. Experiments with colloidal crystals assembled from polyelectrolyte-coated PS spheres demonstrated that a highly hydrophilic surface improves the crystal structure.[167] The carboxyl groups make the PS surface more hydrophilic, and thus the low PA spheres are easier to self-assemble. Despite these factors, it was still possible to fabricate high quality opal templates with all the spheres used in this thesis.

6.2 Results of ALD Infiltration of Opal Templates

6.2.1 Characterization of ZnO for Infiltration

Spectroscopic ellipsometry of ZnO and Al_2O_3 ALD films grown on silicon were used to determine the approximate growth rates per cycle for each material. Table 6.1 summarizes these parameters.

Table 6.1 - Growth rates of ZnO and Al_2O_3 at various temperatures.

Material	Temperature	Growth per Cycle
ZnO	80°C	0.42 nm/cycle
ZnO	175°C	0.47 nm/cycle
Al_2O_3	175°C	0. 38 nm/cycle

These values are only an estimate of the growth per cycle (GPC) during the ALD process and are used to target the minimum number of cycles necessary to infiltrate a specific opal. A systematic study of opal template infiltration was made using the above GPC values and the maximum achievable coating thickness allowed by sphere size and geometry. Maximum coating thickness ranges from 13.3 nm (187 nm spheres) to 30.3 nm (426 nm spheres). Planar films were grown with relatively short (0.5 s) exposure times; however, opal infiltration required longer 1 s exposures to allow the precursors to fully diffuse into the structure. It was found that 100 ALD cycles of ZnO was sufficient to fully infiltrate all size opals with minimal cap layer build-up. The GPC for ZnO inverse opals was very close to that of planar films.

The growth temperature for ZnO is outside of the nominal ALD window. The possibility of incomplete reactions, secondary reactions, and reactive by-products could lead to impurities in the coatings. A second potential source of contamination is the metal precursor flow line. The ALD is set up such that all the metal precursors are carried in one line that is heated to prevent precursor condensation. Energy dispersive spectroscopy (EDS) and time-of-flight secondary ion mass spectroscopy (ToF SIMS) of ALD-grown ZnO films show minimal amounts of carbon (from by-products or un-reacted precursor) when compared with high quality pulsed layer deposited ZnO films.

6.2.2 Inversion of Infiltrated Opal Templates

It is important to balance the temperature and time of the firing process used to invert infiltrated opal templates. Firing has a significant impact on the optical properties of ZnO inverse opals, as the high temperatures accelerate grain growth in ZnO. Figure 6.2 is a firing curve measured by thermogravimetric analysis. The curve shows that ~94% of the PS opal is volatilized at 350^{o}C and above. The loss rate for the remaining 6% is much slower until the temperature reaches 450^{o}C, whereupon the loss rate increases slightly, before leveling off at 500^{o}C. Based on this data, a firing temperature of 400 – 450^{o}C will allow the PS template to be removed as quickly as possible while minimizing grain growth. The sample used for the TGA measurement was small (3 mm x 3 mm). Cutting the sample from a larger inverse opal left an open fracture surface along the sides. The open surface and small volume gave the volatilized PS a more direct route out of the structure and shortened the firing process significantly. An fully intact infiltrated opal

was found to lose the PS through diffusion and small cracks in the structure over a longer period of time. Firing comparisons between full-sized inverse opals with and without the cap layer did not show a significant decrease in firing time. RIE of unfired inverse opals was difficult as the O_2 plasma steps began to etch the PS away without fully cleaning the surface, resulting in etch rate variations.

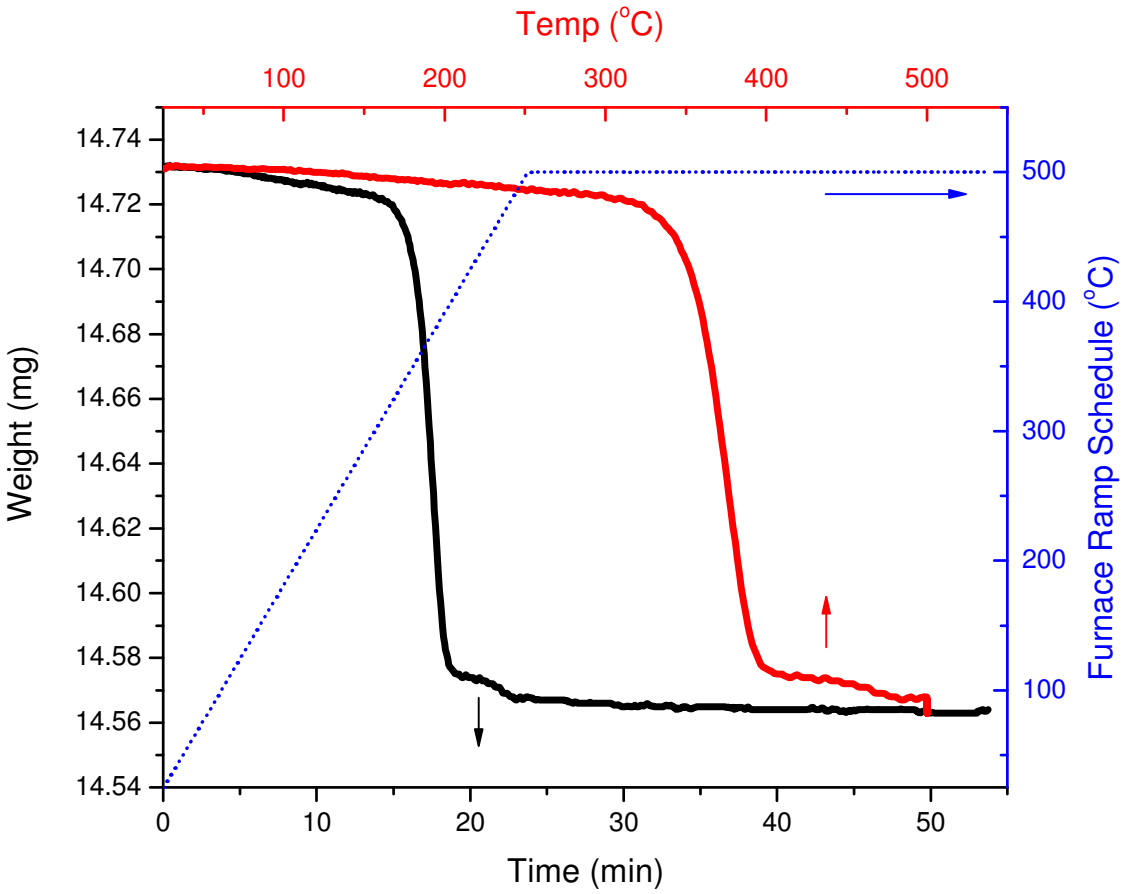

Figure 6.2: TGA curves measured during firing of a PS microsphere template. The temperature was ramped at 25°C/min to 500°C and held for 25 minutes (blue curve). The black curve corresponds to weight lost over time and the red curve to weight lost at a given temperature.

The second approach to controlling the firing time was to change the atmosphere in the furnace. Infiltrated opals placed in a tube furnace connected to a vacuum pump (base pressure 25 mTorr) took 2-3 times as long to invert compared with a typical air atmosphere. Valves connected to the opposite end of the tube allowed gases to flow during firing. Firing under a N_2 atmosphere (500 mTorr) also greatly increased the necessary firing time. Oxygen clearly plays a very significant role in volatilizing the PS spheres. Nitrous oxide (N_2O) was used as an oxidizing agent in an attempt to more quickly burn out the

PS from the inverse opal. At the firing temperature, N_2O will "crack" to yield oxygen radicals that could potentially speed up the rate of PS decomposition. The presence of N_2O during the firing process did not significantly decrease the time needed to remove the PS template and resulted in slightly larger grains than air-fired samples. The ZnO coating prevents the gaseous species from efficiently reaching the spheres. A firing process in air was the most efficient way to remove the PS spheres from the infiltrated opal. A typical full-sized, fully-capped sample required 2 hours at 450°C to be completely inverted. Thicker opals grown from higher sphere concentrations would occasionally require an extra hour to completely burn out all of the PS.

6.2.3 Structural Characterization of ZnO Inverse Opals

Figure 6.3 shows XRD scans for ZnO ALD-grown coatings before and after firing. Low temperature ZnO is nanocrystalline; however the high temperature firing process results in sintering and grain growth. The extent of grain growth depends on both the temperature and duration of the firing process.

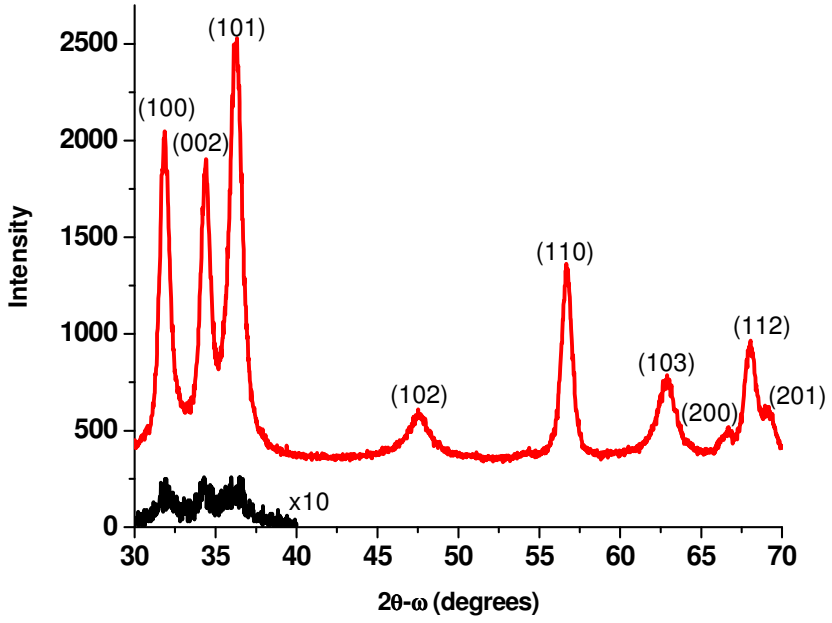

Figure 6.3: XRD from a fired (red curve) and unfired ZnO inverse opal. The unfired spectrum is scaled up by a factor of 10 for visibility

As the grains grow larger they extend out into the air sphere, creating roughness at the air/ZnO interface. This distorts the shape of the air sphere and, for inverse opals with small lattice constants, it can negatively impact the optical properties. For applications such as random lasing, a certain amount of grain growth is necessary to support photon scattering processes.[168] Prior to firing, the ZnO grain size is ~8-14 nm. Firing at 450°C for 2 hours increases the grain size to 20-25 nm. The grain growth rate rapidly increases above this temperature, with grains becoming ~40 nm for only 20 minutes at 550°C.[102] Figure 6.4 shows SEM images of typical ZnO inverse opals grown via ALD.

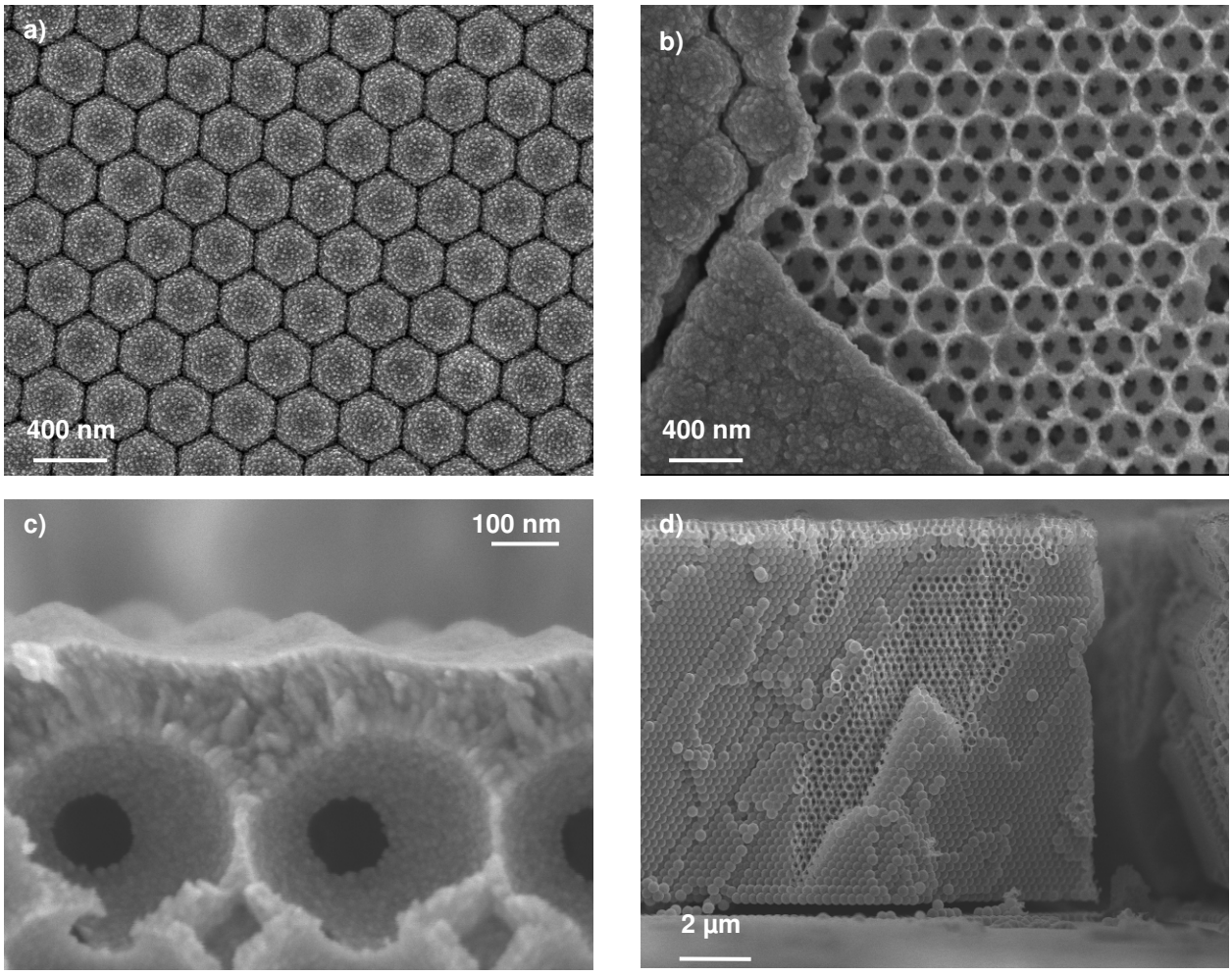

Figure 6.4: SEM images of ZnO inverse opals. a) top view of sphere ordering, b) top view of ZnO cap layer removed, c) detailed side view of grains in the cap layer, and d) side view of a domain and domain crack.

Figure 6.4a shows the excellent ordering of the structure over distances of several microns. In regions where the ZnO cap layer was fractured (Figure 6.4b), it was possible to see the structure of the air spheres and ZnO backbone underneath. The black holes are open spaces produced by PS spheres sintering prior to infiltration. The detailed view of the cap layer in Figure 6.4c shows how the ZnO grains nucleate during the ALD growth process. Once the grains coat the surface of a PS sphere, larger grains nucleate in successive layers until growth is complete. Images of partially infiltrated opals reveal that the early stages of infiltration are characterized by nucleation of individual islands on the PS sphere surface (Figure 6.5). The presence of island growth or mixed layer-island growth (Stranski-Krastanov) is common for many ALD processes.[131]

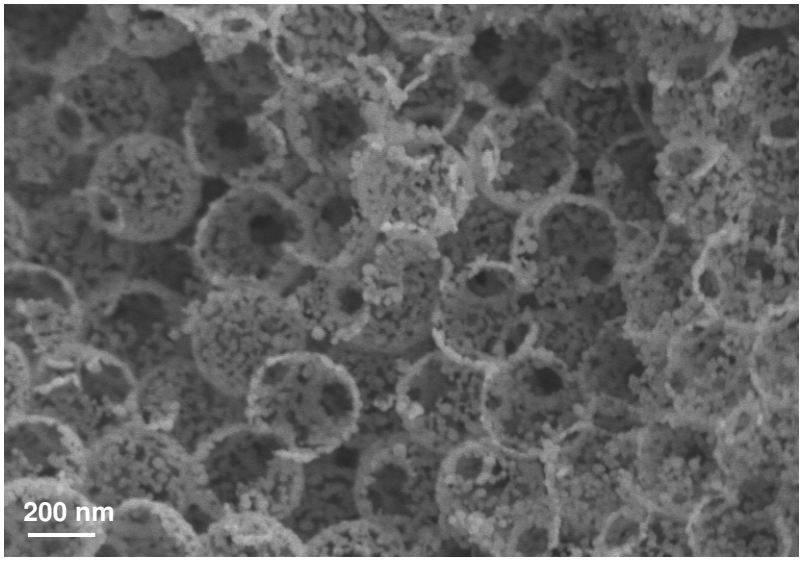

Figure 6.5: SEM image of a partially infiltrated region of a ZnO inverse opal. The early stages of growth are characterized by island growth.

6.3 Optimization of RIE Parameters

The recipe for removing the ZnO cap layer was adapted and optimized from previous experiments in our group.[102,153] The original recipe called for an equal mixture of H_2 (40 sccm) and CH_4 (40 sccm) at 40 mTorr excited by 300 W. This procedure took >15 minutes to etch away the 40-50 nm cap layer and was difficult to control. The same recipe that would yield a fully etched opal in one run would often over- or under-etch in subsequent runs. Frequent O_2 cleaning etches (every 3 minutes)

increased the chance of degrading the surface of the inverse opals. Some of the inconsistency may have been due to build-up of polymer on the surface from the excess CH_x radicals in the max-power plasma during the 3 minute windows between O_2 plasma cleaning steps. In this study, the mixture of CH_4/H_2 was changed to 10%/90% and the power decreased by 33%. This allowed the cap layer to consistently be removed in several minutes for all inverse opal sizes (infiltrated with 100 ALD cycles). Studies of CH_4/H_2 etching of ZnO films demonstrated that processing pressure, gas mixture, and RF intensity can affect etch rates by a factor of 4.[154] Figure 6.6 shows the evolution of this etch recipe for 2, 4, 5.5, 6, and 8 minute etches.

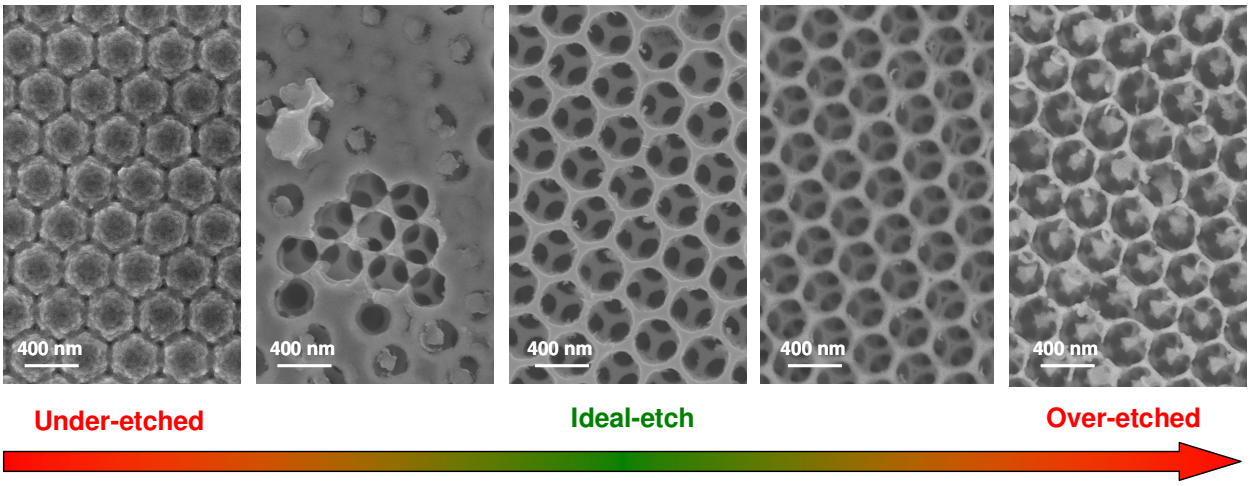

Figure 6.6: SEM images of a ZnO inverse opal surface after 2, 4, 5.5, 6, and 8 minute etches using a CH_4/H_2 mixture.

This etch process will yield a fully "opened" inverse opal without O_2 plasma cleaning; however it was found that inclusion of several cycles of O_2 plasma treatment resulted in a more homogeneous etch. In contrast, running the original recipe without periodic O_2 plasma cleaning increased the etch time. The etch rate will vary across the contours of the cap layer, depending on how the surface is oriented toward the RIE electrodes. Once the top is etched away, the plasma will begin to penetrate into the inverse opal, etching away the finer backbone structure between spheres. For an ideal etch, the top of the cap layer is etched away along with half of the first layer of spheres, leaving the largest possible opening with a flat surface.

6.3.1 Inverse Opal Structure

The RIE process greatly enhances the ability to see into an inverse opal, revealing details of the ordering and defects present in the crystal. Here again there is a strong analogy between photonic and atomistic lattices. Figure 6.7 demonstrates some of the defects commonly found in photonic crystals fabricated by self-assembly of microspheres, including vacancies, dislocations, stacking faults, and grain boundaries.

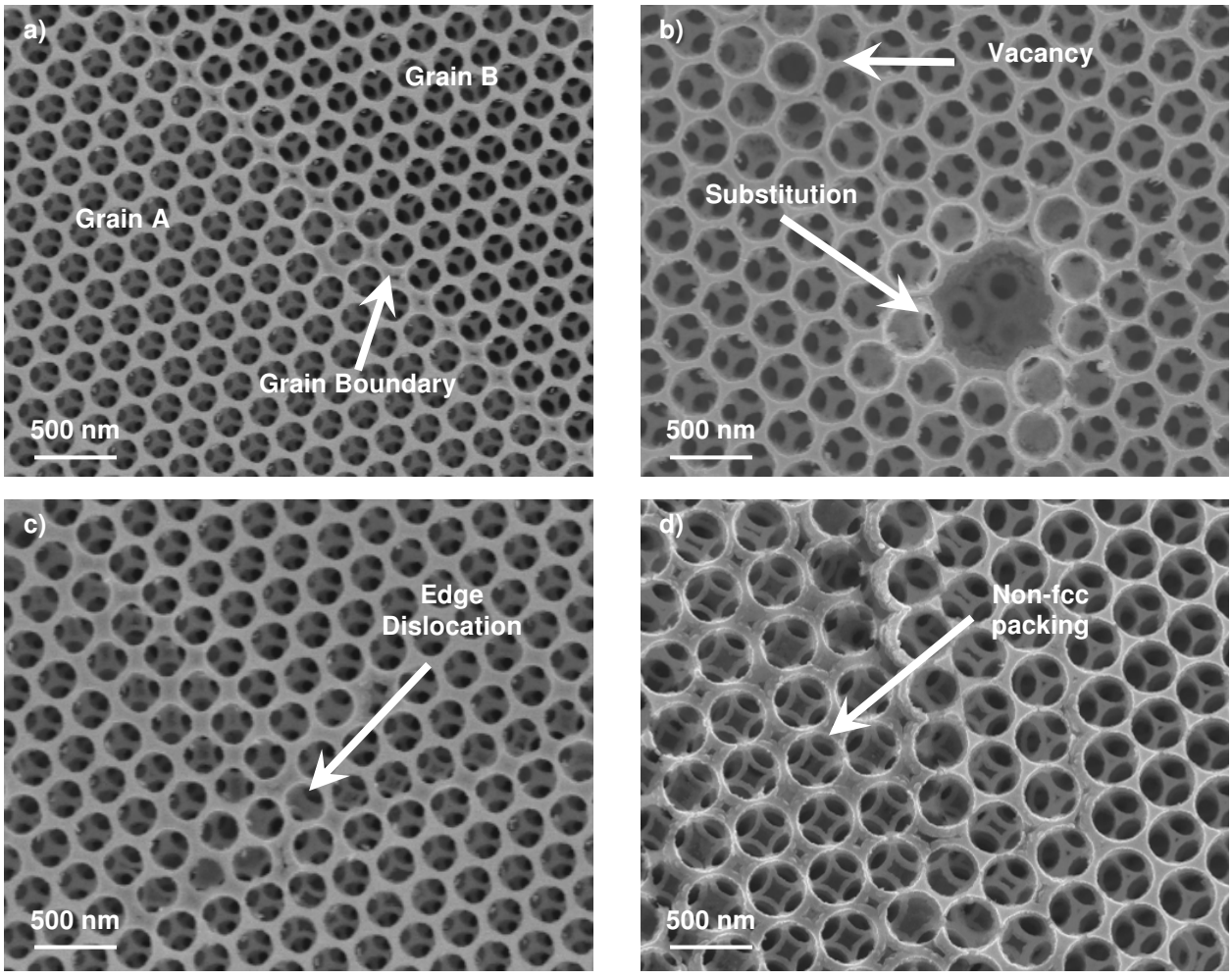

Figure 6.7: SEM images of ZnO inverse opals demonstrating some of the common lattice defects including a) grain boundaries, b) vacancies and substitutions, c) dislocations, and d) changes in orientation.

Defects act as scattering centers or traps for photons passing through the crystal, much like defects in semiconductors can trap or scatter electrons moving through the lattice. To achieve the strongest photonic effects, it is necessary to minimize defects while maintaining a well-ordered long-range lattice. Regions that deviate from normal fcc-packing (Figure 6.7d) will have different photonic band dispersions and act to dilute the strength of the desired [111] photonic band gap. Doping is a common practice to control the electronic properties through engineered defects. Likewise, selective placement of defects in photonic crystals is critical for realizing devices such as waveguides and microcavity lasers.[104] In inverse opal photonic crystals, two-photon polymerization techniques have been developed to selectively etch a defect path through an opal in three dimensions.[5] For the purposes of this thesis, fabrication of inverse opals was undertaken with the intent of limiting the presence of defects.

6.4 Optical Characterization of ZnO Inverse Opals

Transmission and reflection measurements determined the quality of an inverse opal. Deep, well-defined dips in transmission and strong specular reflectivity peaks are the hallmarks of a quality photonic crystal. Excessively broadened or shallow transmission dips and high diffuse reflectivity are indications of large amounts of defects and/or structural disorder. Figure 6.8 shows transmission and reflection spectra from 311 nm and 375 nm ZnO inverse opals. The transmission spectra showed a strong dip where the fundamental PBG prevents photons from passing through the structure (via reflection). The PBGs for the 311 nm and 375 nm inverse opals were centered at 550 nm and 680 nm, respectively. The transmission dipped again near the UV range, as light was absorbed by the ZnO band edge (~378 nm). The reflectivity spectra (Figure 6.8b) showed peaks centered on the PBGs of the inverse opals. Several smaller peaks appeared at lower wavelengths and were correlated with several higher order pseudogaps that develop in the ZnO inverse opal band structure

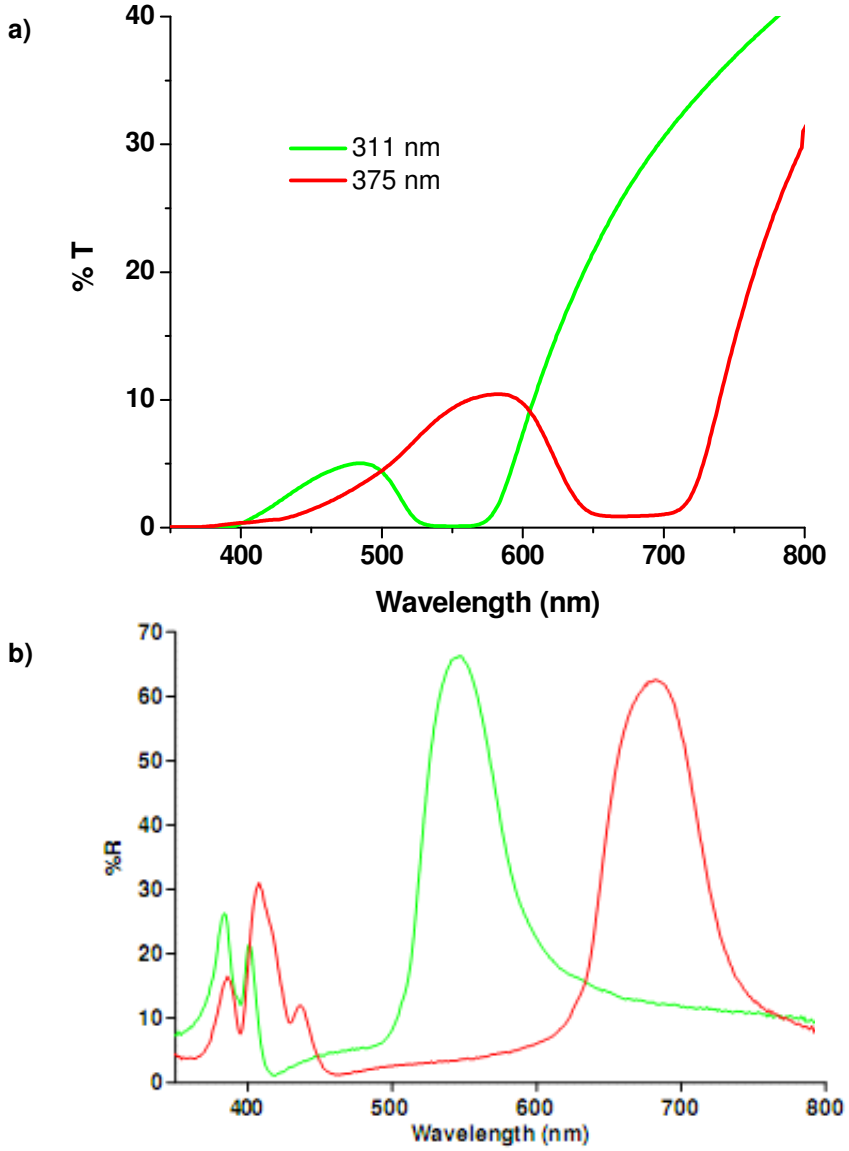

Figure 6.8: a) Transmission and b) specular reflectivity spectra for 311 nm (green curves) and 375 nm (red curves) ZnO inverse opals.

The room temperature ZnO photoluminescence spectrum consists of a sharp peak near the band edge due to exciton recombination (~378 nm), and a very broad peak that can range from 450 nm up to 850 nm. Emission occurs over this range as excitons become trapped at a variety of defects in ZnO before recombining to emit a photon. Green, yellow, and red-orange peaks are common in low temperature fabrication of ZnO nanostructures.[169,170] Oxygen vacancies (V_O), oxygen interstitials (O_i), zinc vacancies (V_{Zn}), zinc interstitials (Zn_i), and several types of impurities are generally thought to be the

centers for defect emission; however, there is still a great deal of controversy over which defects are responsible.[171] Figure 6.9 shows typical PL spectra for ZnO films grown via ALD at 80°C and 175°C. At 175°C, the PL is characterized by a strong band edge emission in the UV and defect emission from 450 nm to 650 nm. At 80°C, the band edge PL peak is barely visible, and defect emission dominates the spectrum. The higher temperature process creates a coating that has few defects and better crystallinity.

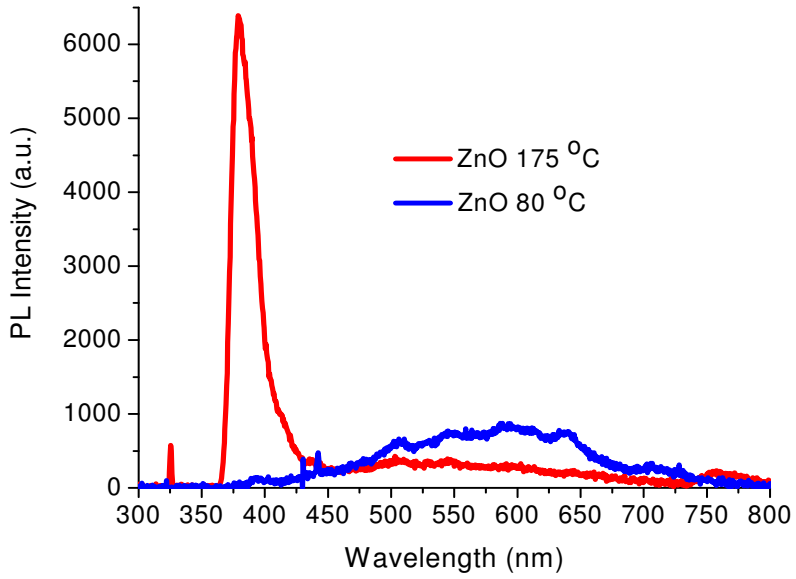

Figure 6.9: PL spectra of a ZnO film grown at 175°C (red curve) and a ZnO inverse opal grown at 80°C.

Photoluminescence from the ZnO backbone was strongly modified by the fabrication process and the photonic band structure. Figure 6.10 is the PL spectrum from a 311 nm ZnO inverse opal. In the vicinity of the fundamental photonic band gap (~570 nm), emission from the ZnO is suppressed. The presence of the PBG effectively traps these photons within the photonic crystal. Since this is not a full PBG, light at this wavelength can escape along other directions.

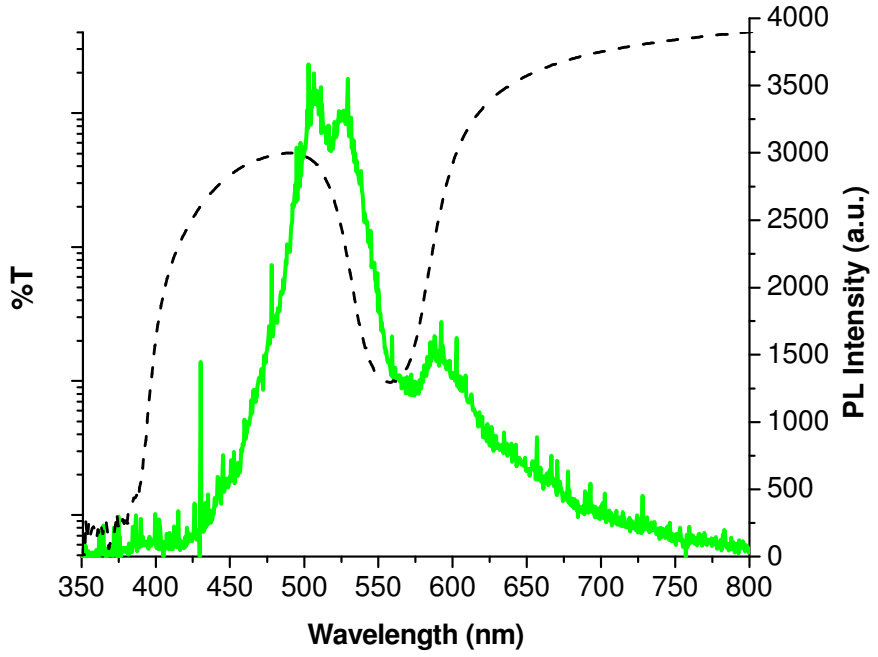

Figure 6.10: PL emission from a 311 nm ZnO inverse opal being suppressed by the PGB located at ~570 nm. The dashed line is a log plot of the transmission from the same structure. The band gap in %T is blue-shifted slightly as the measurement is taken slightly off normal.

6.4.1 Effects of ALD Growth Temperature on Optical Properties

The general procedure for infiltrating ZnO into opal templates made use of a substrate temperature of 80°C to stay well below the T_g for PS. The bulk value for PS T_g is ~95°C, as reported by the PS microsphere manufacturer. It has been shown that the T_g for PS microspheres, while similar to the bulk value, ranges from 92°C to 101 °C.[172] A core-shell model was proposed with a bulk-like PS core surrounded by a mobile ~4 nm shell with a T_g < 40°C. A series of 311nm and 375nm opal templates were infiltrated with ZnO at 80°C, 100 °C, 120°C, and 140°C to determine how the spheres are affected by temperatures around the T_g. For each deposition, the opals were sintered for ~ 1 hour prior to deposition at 25 mTorr. Figure 6.11 shows reflectivity from the resulting ZnO inverse opals. Deformation due to softening in spheres sintered at 120 and 140°C destroys the periodicity of the structure, removing the PBGs (no reflectivity peak). The slight change in the positions of the high-order peaks sintered at 80 and

100 °C is due to changes in the size of the connecting windows and interstitial air pores. The ability to heat the spheres up to 100 °C was important as it allowed for infiltration of higher quality ZnO material.

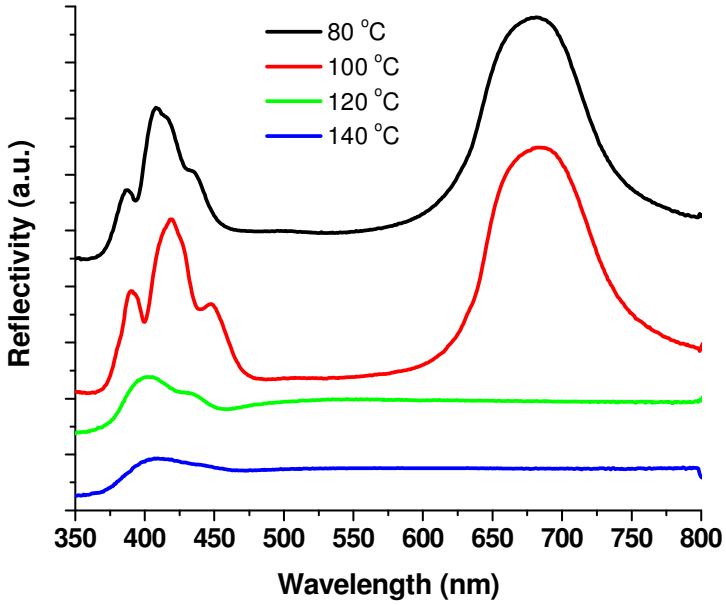

Figure 6.11: Reflectivity of 375 nm ZnO inverse opals fabricated from opals sintered at 80 °C (black), 100 °C (red), 120 °C (green), and 140 °C (blue).

6.4.2 Effects of RIE on ZnO Inverse Opal Optical Properties

6.4.2.1 Photoluminescence Modification

Reactive ion etching has a significant effect on the optical properties of inverse opal photonic crystals. Figure 6.12 shows PL spectra for ZnO inverse opals prior to RIE (after firing) and after RIE. There are two features to note: 1) decreased defect emission between 450 - 700 nm and 2) significantly enhanced band-gap emission at 380 nm. The inverse opal size was 375 nm, with a fundamental PBG at 680 nm.

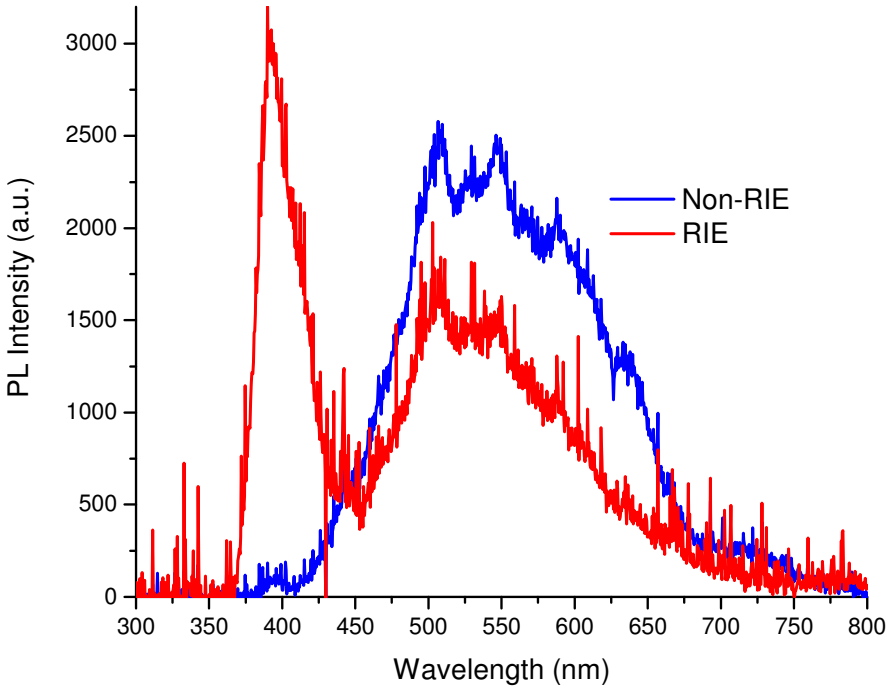

Figure 6.12: Photoluminescence from a 375 nm ZnO inverse opal before (blue curve) and after (red curve) RIE processing. The peaks at 390 nm correspond to band edge emission from ZnO. The fundamental PBG appears at 680 nm, suppressing the tail end of the broad defect emission band.

Increasing the H_2 percentage in the CH_4/H_2 plasma etch for ZnO from 40% to 90% prevents excess CH_x radical formation at the cost of creating a significant number of highly energetic H^+ ions. The etch rate is limited by how quickly CH_x radicals react with Zn^+ to form volatile species. Thus, the rate of reaction of H^+ with O^{-2} is also limited by the amount of CH_x present. The large imbalance in the ratio of H_2 to CH_4 results in an excess of H^+ ions that can become incorporated in the inverse opal. Van de Walle proposed that interstitial hydrogen can act as a shallow donor in ZnO and is likely one of the factors responsible for its n-type conductivity.[173] Incorporation of additional hydrogen in ZnO by plasma treatment or annealing can enhance the free carrier concentration (and thus conductivity) and passivate deep-level defects, improving band-edge emission.[174-177] Several models have been proposed for the position of hydrogen in the ZnO lattice at different temperatures and doping levels.[173,178,179] During the etching process, the excess high-energy H^+ ions diffuse into the ZnO backbone, passivating a portion of the defects and enhancing the band-edge emission. There remains a significant level of emission from defect states that are likely re-introduced into the ZnO during the O_2 plasma cleaning steps. Additional H_2

plasma treatment further enhances the UV band-edge emission and completely suppresses defect emission. This treatment followed the same procedure as the CH_4/H_2 etch with Ar replacing CH_4. Figure 6.12 is the PL from a post-RIE H_2 plasma treated inverse opal. Figure 6.12b shows the structural damage sustained by the inverse opal surface during this etch.

The hydrogen-doped inverse opals are relatively stable over time at room temperature, with the band-edge UV emission remaining relatively strong after at least one month. Over longer periods, it is expected that the H^+ will completely diffuse out of the ZnO. This can be greatly accelerated by heating the inverse opal. A 10 minute anneal at 400 ^oC in air is sufficient to return the PL to its original post-fired state. The enhanced band edge emission can prove useful for photonic crystals used in UV-emitting applications such as lasers or LEDs.[168]

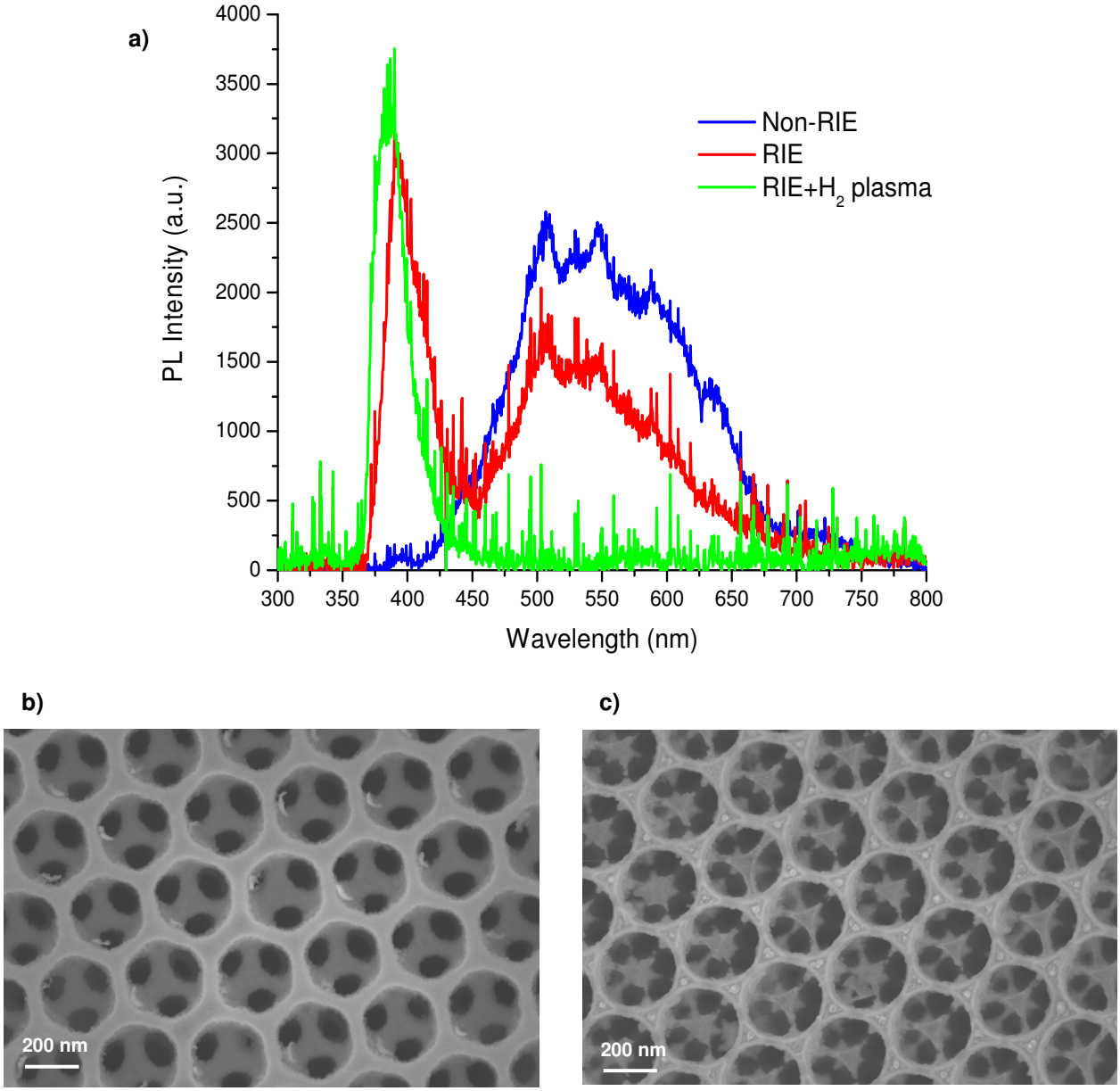

Figure 6.13: a) Photoluminescence from a 375 nm inverse opal that has been RIE processed, followed by treatment with a H_2 plasma (green curve). The blue and curves are the same as those in Figure 6.12. The H_2 plasma quenches all defect emission from the ZnO. SEM images show b) the normal RIE processed surface and c) the damage induced by the H_2 plasma.

6.4.2.2 High-Order Reflectivity Peak Modification

The pre- and post-RIE reflectivity spectra for a 375nm ZnO inverse opal are shown in Figure 6.14a. Figure 6.14b-c shows a cross-section of how the inverse opal surface is modified during RIE.

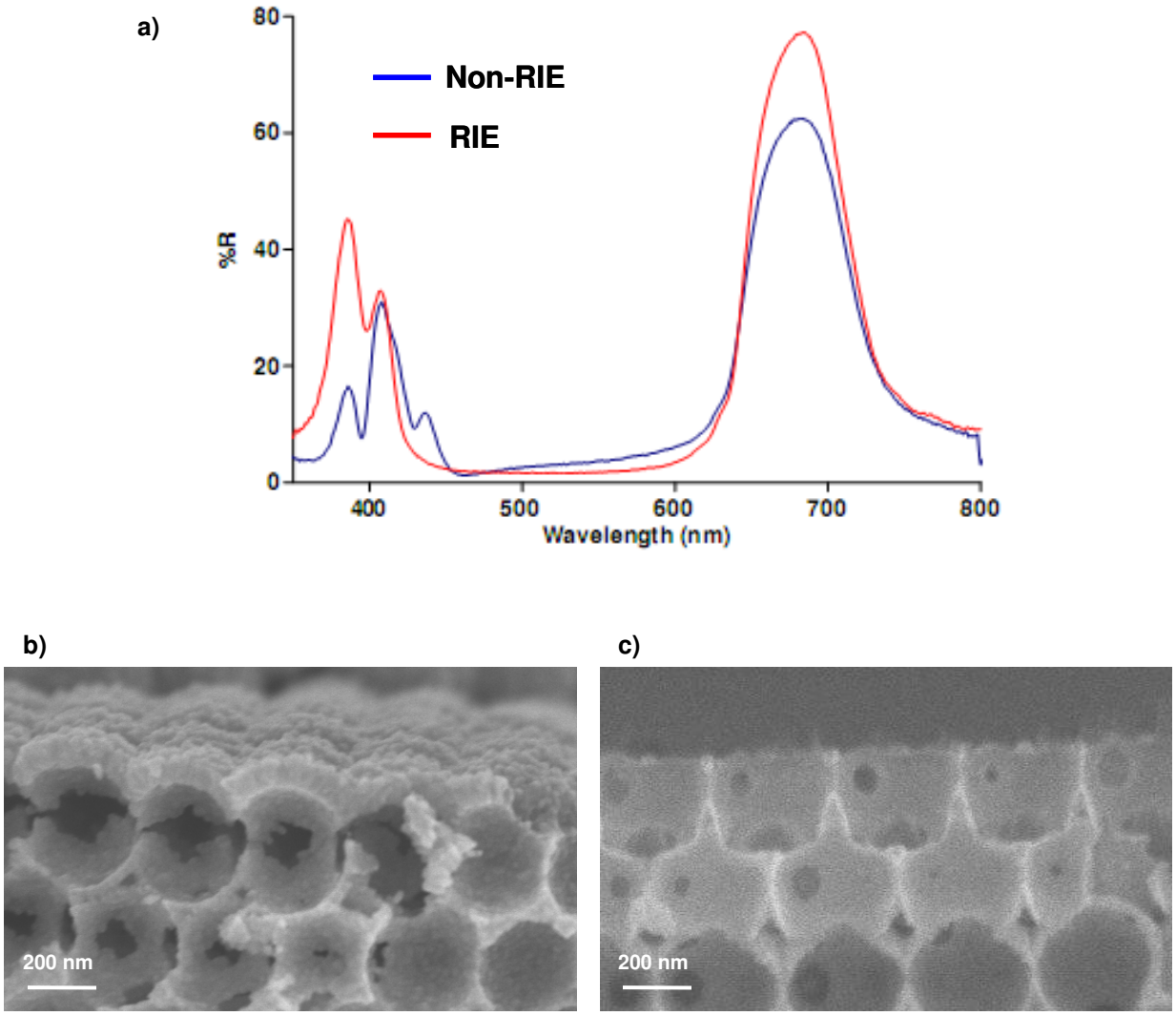

Figure 6.14: a) Specular reflectivity and SEM images of an inverse opal b) before and c) after RIE processing. The blue and red curves represent reflectivity before and after etching, respectively. Etching removes the contoured cap layer, leaving a flat surface.

As expected, the fundamental PBG remains unchanged; however, there are several changes in the number and intensity of the high-order peaks near the UV region. Prior to RIE, the inverse opal exhibits four high order peaks at 440 nm, 425 nm, 415 nm, and 375 nm. After the RIE process, the peaks at 440 nm and 425 nm disappear and the intensity of the 375 nm peak is enhanced. The ZnO inverse opal band structure in Figure 4.2 indicates that there are only two high-order gaps, and thus only two peaks shown be produced in the reflectivity spectrum. The additional peaks in the pre-RIE spectrum appear due to reflection of light at the contoured surface of the inverse opal. The cap layer on the inverse

opal acts as a waveguide grating that creates a resonance due to Wood's anomalies. Diffraction of guided modes causes them to become "leaky", allowing them to escape the waveguide (cap layer) surface. Incident light at this frequency sets up a resonance that redistributes energy in the diffracted modes.[180] The resonance is controlled by the refractive index of the waveguide layer and the geometry of the grating. Removing the cap layer removes the waveguiding element and the extra reflection peaks disappear. The presence of these resonances may have a significant impact on the effectiveness of the photonic crystal. They reflect light at the surface, preventing the coupling needed to access many of the potentially useful optical modes within the photonic crystal, such as slow light modes and embedded cavities or emitters. The RIE process provides a straightforward technique for improving the coupling to higher-order band gaps in ZnO inverse opals.

6.4.3 Angle-Dependent Optical Properties

The photonic band gaps in ZnO inverse opals are pseudogaps that open up only along specific directions. The band structure indicates how the position (frequency) of the band gap changes along a given direction. The angle-dependent nature of these structures is easily seen with the naked eye (Figure 6.15).

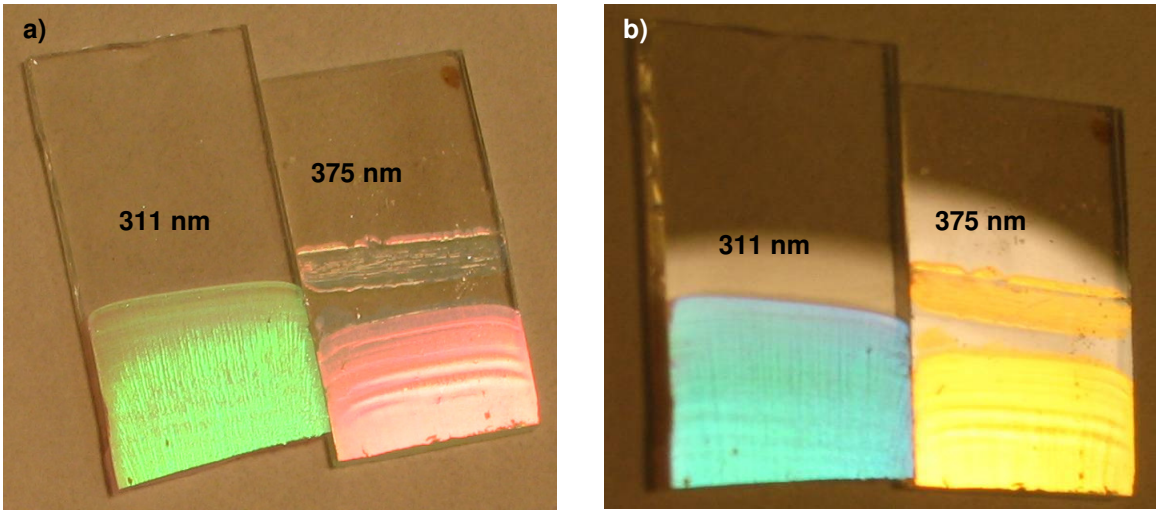

Figure 6.15: Images of 311 nm and 375 nm ZnO inverse opals at roughly a) 0° and b) 30° angle of incidence. The shift of the photonic band gap is apparent by the changes in color.

Measurements of the angle-dependent reflectivity showed that the fundamental photonic band gap blue-shifts with increasing angle of incidence. Reflectivity measurements combined with band structure modeling also showed that the photonic crystal band structure also depends on the polarization of the incident light. Figure 6.16 is the reflectivity from a 424 nm ZnO inverse opal illuminated with *s*- and *p*-polarized light.[155]

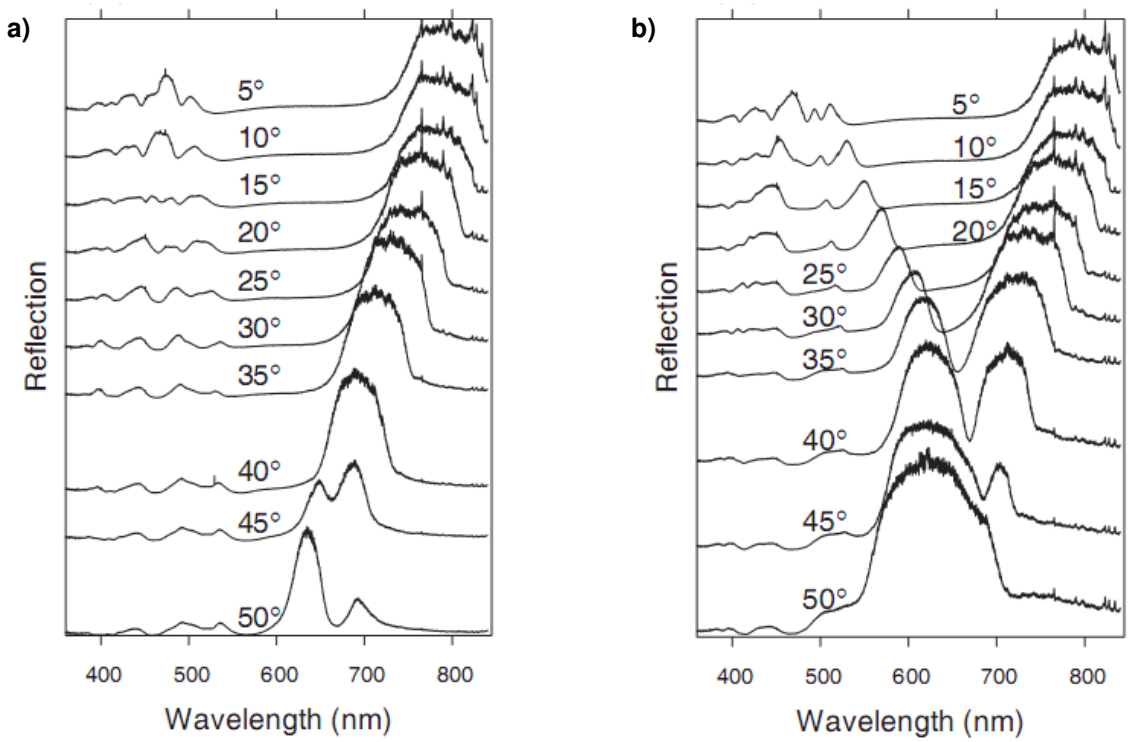

Figure 6.16: Angle-depended reflectivity for a 424 nm ZnO inverse opal for a) *p*-polarized light and b) *s*-polarized light. The angle of incidence is given next to each plot.

The fundamental band gap, found at 800 nm, blue-shifts with increasing angle for both polarizations. The higher order peaks (400 – 500 nm) behave differently. For *p*-polarization, they remain relatively nondispersive; however, for *s*-polarization, the peak at 510 nm significantly red-shifts with increasing angle. At about 45°, these two peaks exhibit anticrossing and a sharp dip in reflectivity appears. This corresponds to a stationary inflection point in the band structure and the appearance of a frozen mode. A frozen mode is characterized by low group velocity ($d\omega/dk \sim 0$) and good impedance matching with the PhC/air interface ($d^2\omega/dk^2 \sim 0$). This effect was used to enhance the *s*-polarized defect

PL from ZnO inverse opals resonant with this mode.[155] Figure 6.17 shows the normalized *s*-polarized PL from the 424 nm inverse opal. Each spectrum was normalized by the PL emission of a random sample. This sample was made by infiltrating an opal of multiple sphere sizes, which prevents any ordering or photonic band gap effects. The dashed line in each curve is unity; PL above this line is enhanced, and PL below is suppressed. Suppression due to the photonic band gap can be seen in the dip at 800 nm.

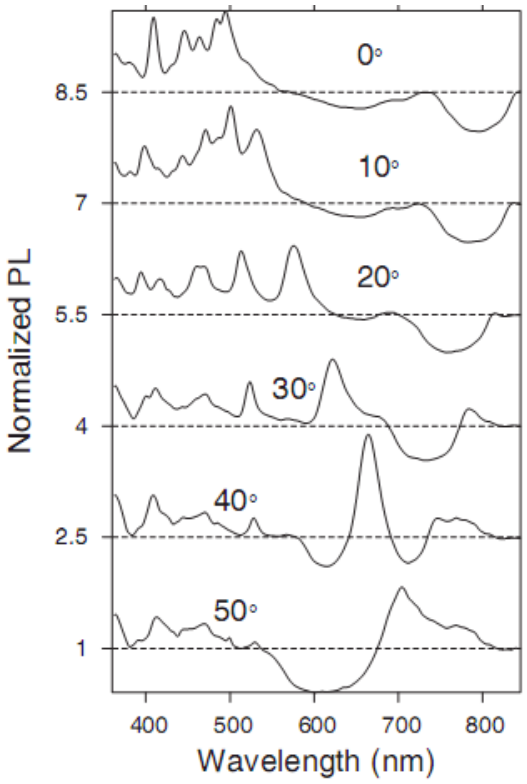

Figure 6.17: Angle-depended reflectivity for a 424 nm ZnO inverse opal for a) *p*-polarized light and b) *s*-polarized light. The angle of incidence is given above each plot.

PL on the shoulder of the higher order gaps is enhanced due to the increased density of states (DoS) near the edges of the flat band. The rate of spontaneous emission is known to depend on the density of states.[104] For a low DoS (e.g. a photonic band gap), emission is suppressed, while a high DoS leads to enhanced emission. The density of states is proportional to the inverse of the group velocity; thus, a flat band with a low group velocity (enhanced light-material interaction) has a high DoS. As the angle of incidence is increased the enhanced PL peak starting at ~500 nm red-shifts with dispersion similar to the

s-polarized higher order reflectivity peak seen in Figure 6.16b. For comparison, the two spectra are overlaid in the top row of Figure 6.18.[155]

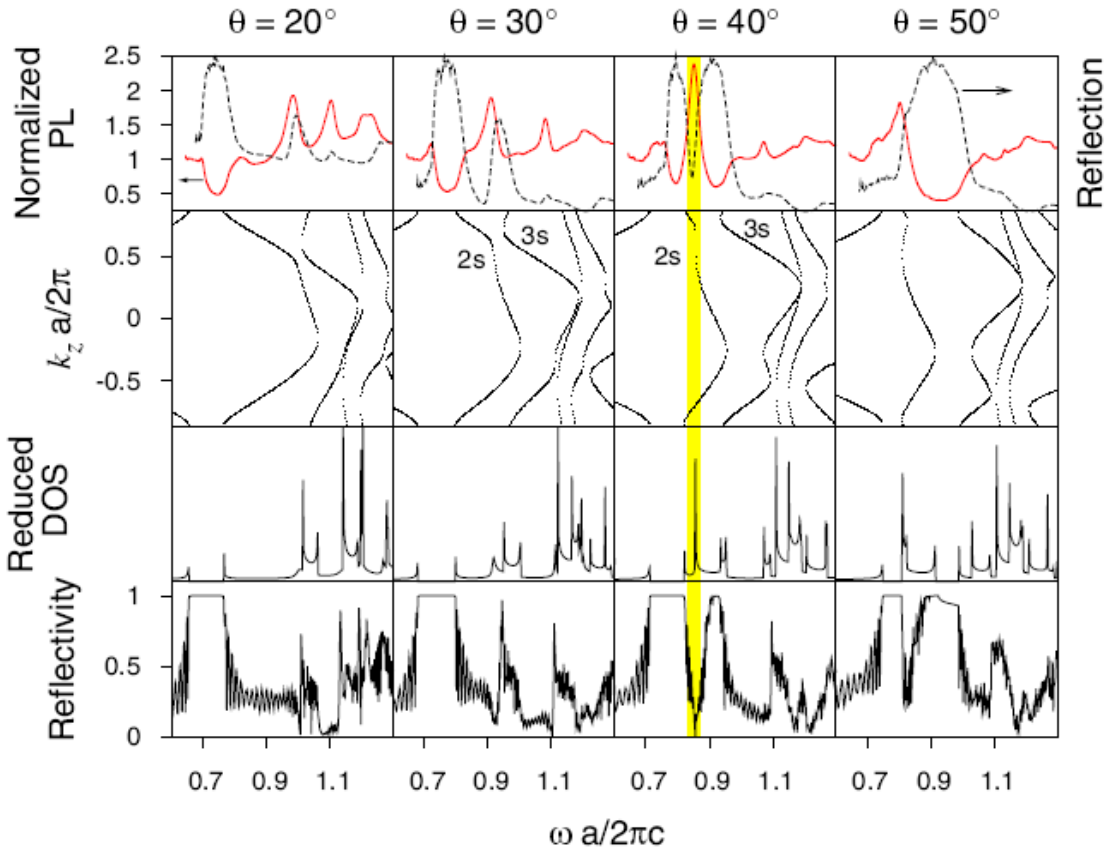

Figure 6.18: First row: angle-resolved *s*-polarized reflection spectra (black dashed line) of the ZnO inverse opal overlaid with the normalized PL spectra (red solid line) of the same polarization and angle θ. Second row: calculated *s*-polarized reduced band structure of the ZnO inverse opal for a fixed angle of incidence and/or exit in air. Lattice constant *a*=566 nm; the dielectric constant of ZnO = 3.8. Third row: calculated reduced density of *s*-polarized states of the ZnO inverse opal. Fourth row: calculated reflectivity of *s*-polarized light from a ZnO inverse opal whose thickness is 34 layers of air spheres. θ =20° (first column), 30° (second column), 40° (third column), and 50° (fourth column). For θ =40°, a stationary inflection point is developed for the 2*s* band at ω*a*/2π*c*=0.856 (yellow band).

Each column represents an increasing angle of incidence from 20° - 50°. The second row displays the reduced band structure for a ZnO inverse opal. The third row is the calculated reduced density of states along a specific direction. The fourth row is the calculated reflectivity spectrum, which matches well with the experimental spectrum. A maximum enhancement of the PL is seen at 40° at the stationary inflection point. At θ = 50°, the 2s band shows local maxima and minima at $k_z a/2\pi$ ~ 0.5 and 0.7. When the angle

shifts to 40°, these two points cross, forming a large flat band in the region of interest. With decreasing angle, the slope of the 2s curve does not change sign, confirming that there is a stationary inflection point at θ = 40°. The high density of states due to the flat band enhances the emission of the ZnO, which can be efficiently extracted from the photonic crystal due to the merging of the local maxima and minima in the 2s band and a sharp drop in reflectivity at that point. In the case of *p*-polarized light, the 2p and 3p are weakly coupled and do not show any band repulsion. This is due to poor diffraction of *p*-polarized light due to a Brewster angle effect.

6.5 Infiltration and Distribution of Quantum Dots in Inverse Opals

Quantum dots provide an alternate light source for further testing of the frozen mode enhancement seen in the ZnO defect emission. They have been used to examine emission suppression, redistribution, and enhancement by the fundamental PBGs in a variety of photonic crystals.[94,97,181,182] Figure 6.19a is a series of fluorescence confocal microscopy images showing the macroscopic distribution of QDs through the inverse opal thickness after a 24 hour horizontal soak and 1 minute rinse in toluene. There was significant build-up of QDs in the large cracks between domains in the inverse opal. The bright regions in Figure 6.19a indicate luminescence from QDs. The intensities of these domain cracks are much higher than the QDs infiltrated inside the domains. The infiltration process was improved by soaking the samples in the QD solution vertically and rinsing under gentle agitation for 5 minutes. The result is shown in Figure 6.19b. The excess QDs are completely removed from the domain cracks and the QD distribution appears homogeneous throughout the entire thickness.

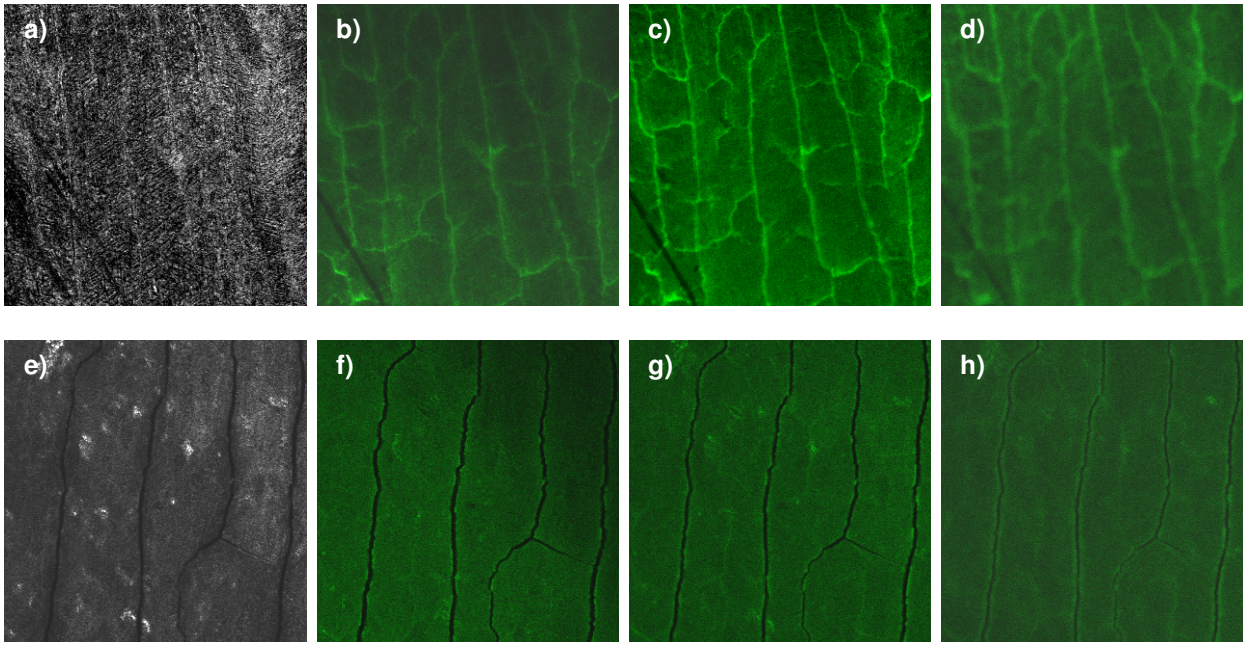

Figure 6.19: Confocal microscopy images of a ZnO inverse opal infiltrated with QDs. The top row shows an un-rinsed sample and the bottom a rinsed sample. a) and e) are the respective reflected light images. b) – d) and f) – h) are QD emission images from the top, middle, and bottom of each sample, respectively. The brightness in these images represents QD emission.

6.6 Modification of QD Emission by Inverse Opals

Initial attempts to match up the frozen mode of 375 nm ZnO inverse opals with the QD emission peak proved difficult. The actual stationary inflection point in the samples varied slightly from sample to sample (typically <10 nm) and the emission peak from a single QD size was very sharp. Analysis of the changes in emission peak shape was difficult when the stationary inflection point fell on one shoulder. The broad, relatively homogeneous defect emission from ZnO provided an excellent backdrop for examining the effects of emission enhancement. In order to achieve a broader emission profile from the QDs, all four sizes were mixed and infiltrated in the inverse opal. The ratio of each size was adjusted according to individual stock solution concentrations and quantum efficiencies. Figure 6.20 shows the PL from QDs that were infiltrated into a 375 nm ZnO inverse opal. The frozen mode is located at approximately 550 nm in the 40^{o} angle of incidence based on angular-dependent reflectivity measurements (not shown). As can be seen in Figure 6.20, there was no significant enhancement of the QD mission due to the presence of the frozen mode.

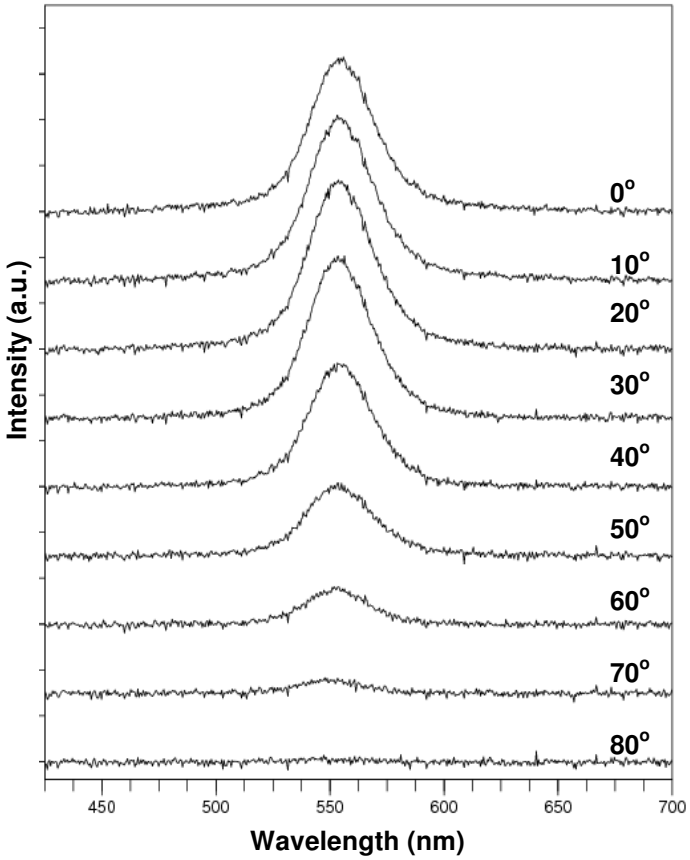

Figure 6.20: Angle-dependent *s*-polarized PL spectra from QDs infiltrated into a 375 nm ZnO inverse opal. The frozen mode appears at ~550 nm in the 40° rotation.

Similar measurements from other inverse opal sizes, different inverse opal thicknesses, and different QD emission profiles yielded the same result. The structure of the inverse opal had been optimized in the experiments described above and was still capable of producing enhanced defect emission PL after extensive processing. The lack of enhancement may be due to a couple factors. The positions of the QDs in the inverse opal were slightly different compared to the ZnO backbone, as illustrated in Figure 6.21. The local (position-dependent) density of states can vary significantly between the air and dielectric phases of a PhC. A structure made from an optically active material such as ZnO may behave differently than a structure that has been infiltrated with an emitting material. Kristensen *et al.* recently modeled the projected local DoS for a silicon inverse opal at several high symmetry points.[183] In this model, the highest

local DoS was achieved at a position where two air spheres meet, just inside the backbone material. The second factor is structural quality. To change the position of the QDs in the inverse opal structure, a two-step process was developed. An opal template was removed from the ALD after 20 cycles, infiltrated with QDs, and placed back in the ALD to complete the infiltration. By using partial infiltration, it was hoped that the QDs would become embedded in the ZnO backbone. There were several processing issues that prevented the realization of this structure. The partially-infiltrated opal had to be fired prior to QD infiltration, as the QDs are damaged at high temperatures. The precursors also had a deleterious effect on the QDs, as exposure to any of the precursors in the ALD caused some degree of emission quenching. Finally, since the structure was inverted, the second round of 80 ALD cycles began to fill in the air spheres (normally occupied by PS microspheres), changing the periodicity of the lattice and altering the band structure.

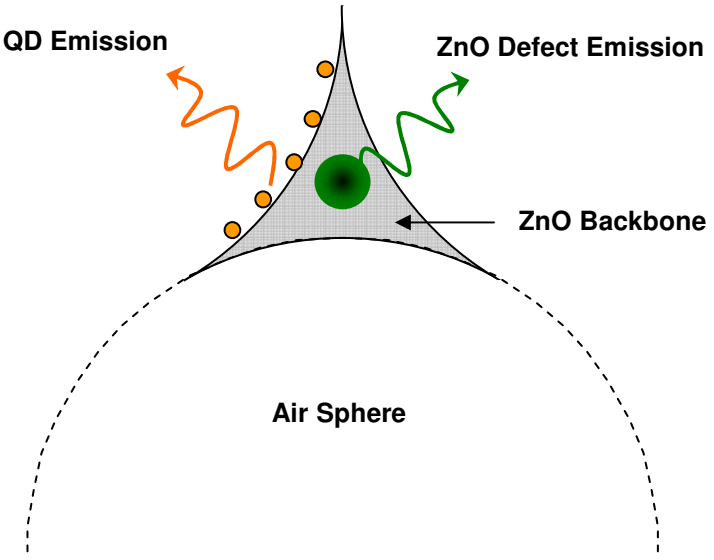

Figure 6.21: Schematic of QD position versus the ZnO backbone of a ZnO inverse opal.

6.7 Infiltration of Silver and Gold Nanoparticles into ZnO Inverse Opals

6.7.1 Solution-Based Synthesis of Silver and Gold Nanoparticles

Synthesized silver and gold nanoparticles (5 nm and 15 nm diameters, respectively) showed excellent monodispersity and batch-to-batch-reproducibility. STEM images of the particles are shown in

Figure 6.22a-b. The AuNPs average 15.9 nm in diameter and the AgNPs average 5.61 nm in diameter. The plasmon resonances for the nanoparticles appear as dips in the transmission spectra in Figure 6.19c. The plasmon resonances for the AuNPs and AgNPs are 520 nm and 410 nm, respectively.

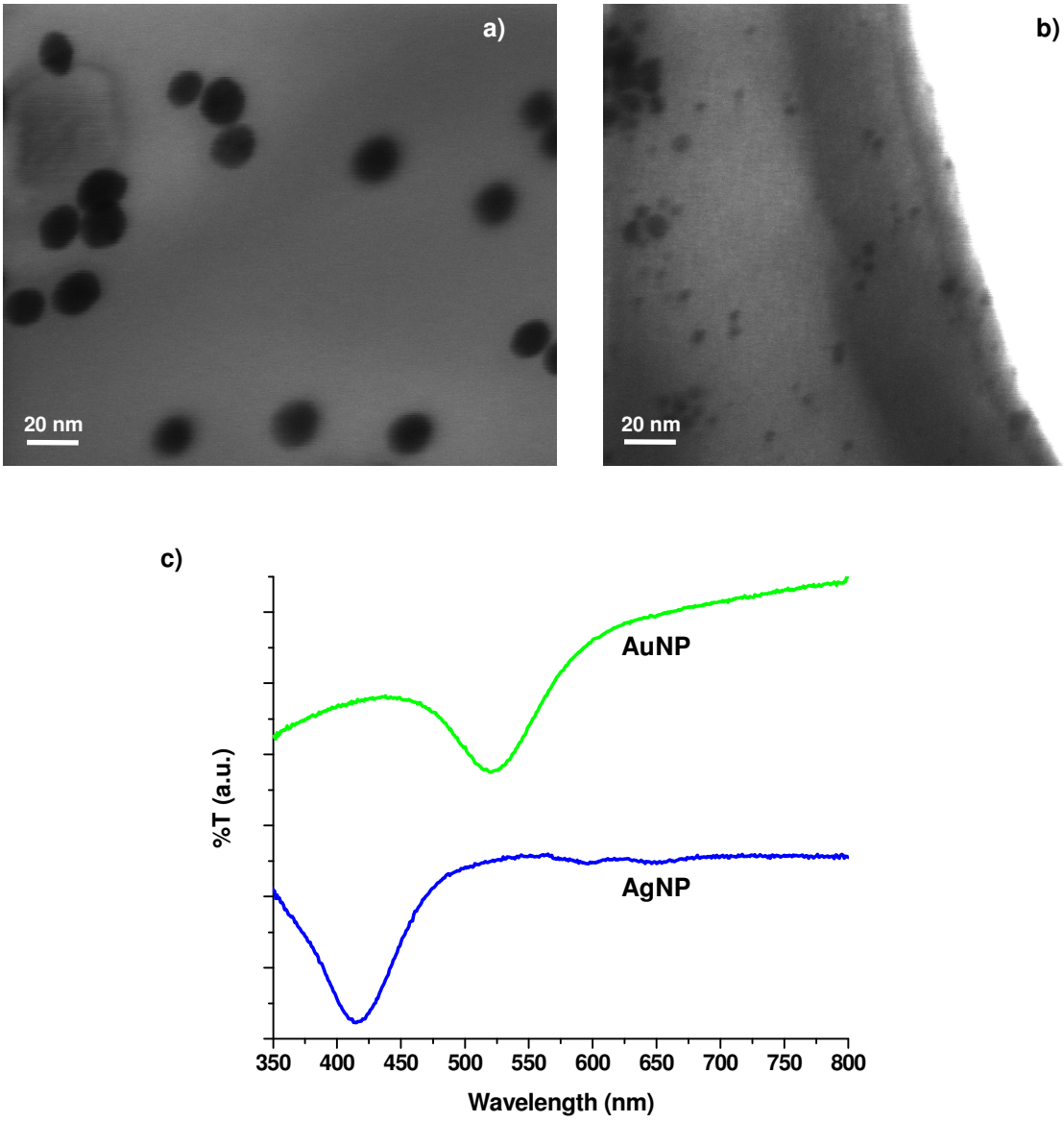

Figure 6.22: STEM images of a) 15 nm AuNPs and b) 5 nm AgNPs with c) their corresponding transmission spectra.

6.7.2 ZnO Inverse Opals Coated with Gold and Silver Nanoparticles

The desired result from the metallic nanoparticle infiltration was an inverse opal with a homogeneous distribution of nanoparticles throughout the structure. APTMS and PDDA were not necessary to trap metal nanoparticles in the inverse opal structure; rather, their role was to provide attachment sites within the structure to promote a dense, even coating. Reflectivity measurements of inverse opals functionalized with APTMS or PDDA showed a slight red shift (~5 nm) of the fundamental PBG due to the slight change in effective refractive index for the structure. The soak times in the metal nanoparticle solutions were limited to less than 4 hours to prevent excessive damage to the structure. ZnO is slightly soluble in water and can be attacked by excess citrate ions in the AuNP and AgNP solutions. Nanocrystalline ZnO films that had not been annealed were etched away completely within 30 minutes. Fired ZnO inverse opals had better crystallinity and were much more resistant to damage in the solution. The small size of the AgNPs made it difficult to image them by SEM. Additionally, the plasmon peak is near the ZnO band edge, and is often difficult to resolve from transmission spectra. The AgNPs were used as seeds to grow larger Ag particles in the inverse opals. The larger size was easier to image and the red-shifted plasmon peak was easier to detect. Figure 6.23 shows SEM images of AuNPs and AgNPs infiltrated into ZnO inverse opals.

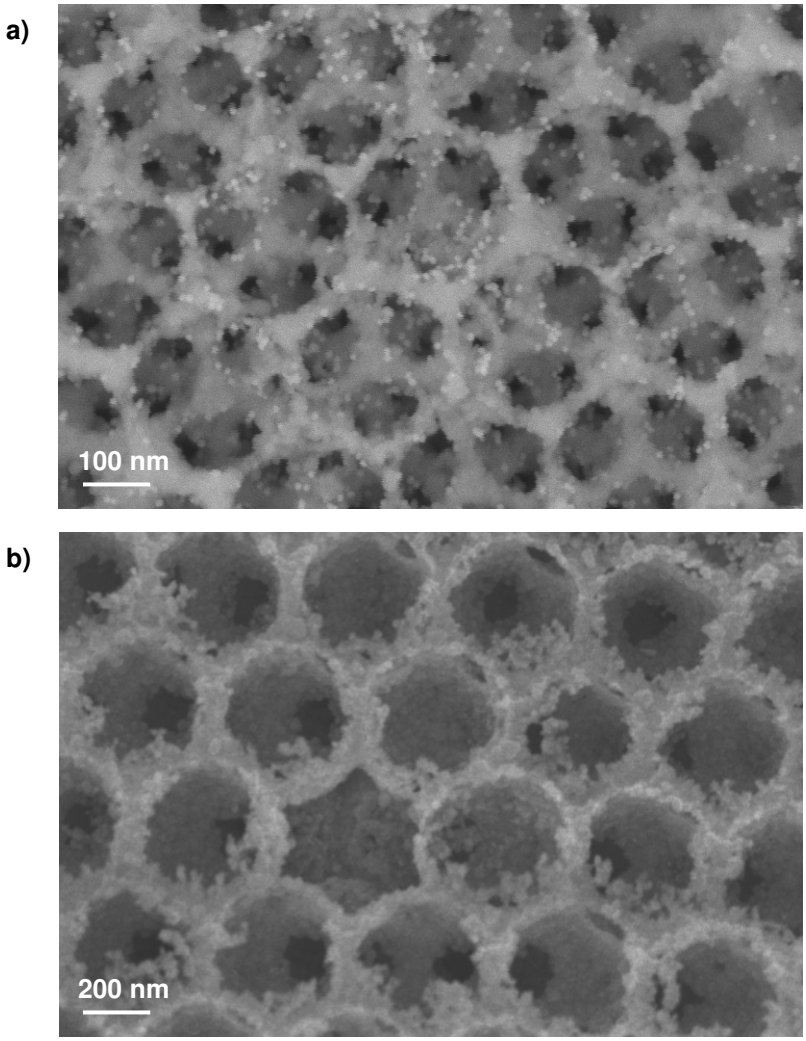

Figure 6.23: SEM images of a) AuNPs and b) grown AgNPs in ZnO inverse opals. The image in a) is a backscattered electron image showing increased Z contrast between AuNPs (bright dots) and the ZnO backbone.

The SEM image in Figure 6.23a is a backscattered electron image that provides good atomic number (Z) contrast between the AuNPs and the ZnO backbone. The additional growth of the AgNPs was achieved by soaking the infiltrated inverse opal in a concentrated (0.1 M) $AgNO_3$ solution. After soaking for 15 minutes, the inverse opal was removed and placed in a slow reducing solution (formaldehyde). The particles grew to 40 nm in diameter over the space of several minutes. Fast reducing agents (e.g. NH_4OH) resulted in excessive overgrowth of silver on the surface of the inverse opal. The maximum concentration of AuNPs and AgNPs inside the inverse opals should be limited by Coulomb repulsion from

the citrate ions attached to the metal nanoparticle surfaces.[184] Figure 6.24 shows the transmission spectra from inverse opals infiltrated with AuNPs and AgNPs. The AuNPs were infiltrated into a 311 nm inverse opal, which has a PBG near the plasmon resonance. The plasmon peak is seen as a broadening of the transmission dip on the low wavelength side. The AgNPs were infiltrated into a 183 nm inverse opal, which has a PBG in the UV spectrum. The plasmon peak for the AgNPs is red-shifted due to the increase in particle size during the growth process. This shift was also confirmed from transmission measurements of AgNPs attached and grown on a glass slide. AuNPs were also infiltrated into inverse opals with PBGs away from the plasmon resonance. These samples also had transmission spectra modified by the presence of plasmonic material. This technique provides a simple way to create a range of tunable plasmonic/photonic structures. Similar systems have been applied as biosensors[8] and refractive index sensors.[148]

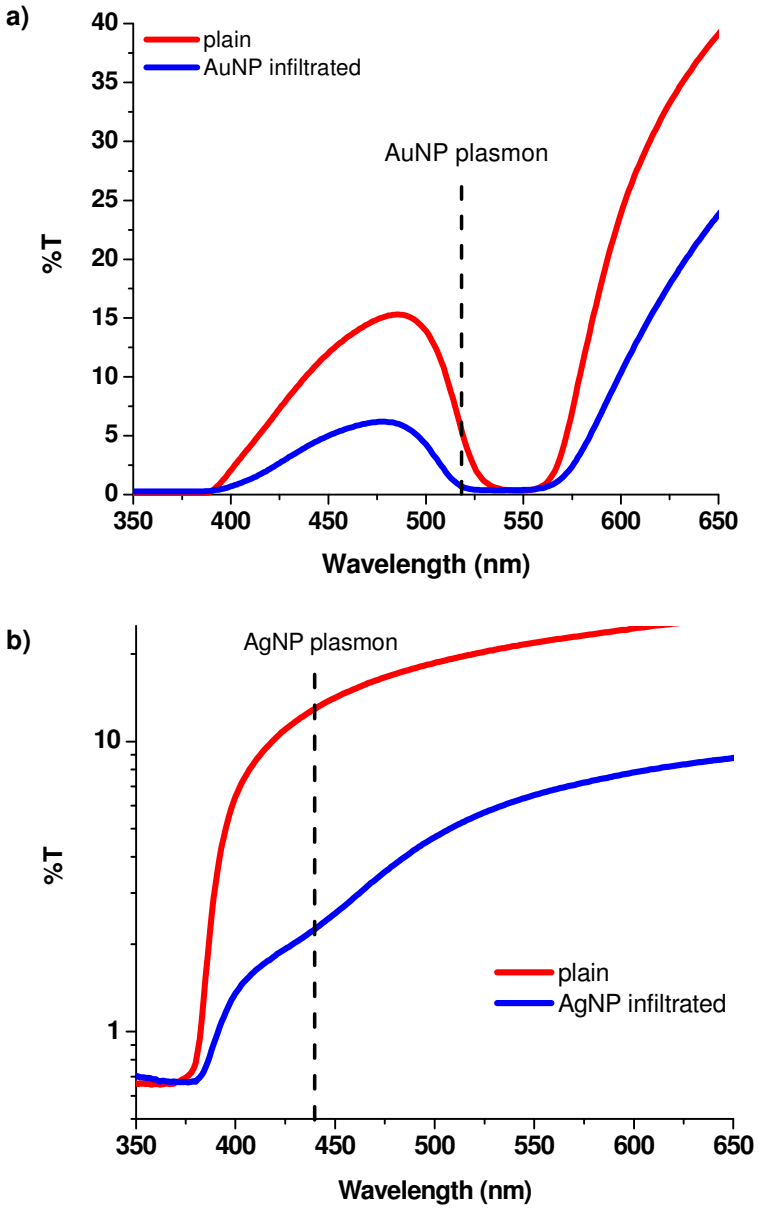

Figure 6.24: Transmission spectra of a) 311 nm ZnO inverse opal infiltrated with AuNPs and b) 183 nm ZnO inverse opal infiltrated with grown AgNPs. The dashed lines indicate the position of the plasmon resonance for each metal nanoparticle.

6.8 Conclusions

This work examined, in detail, a full fabrication process for ZnO inverse opal photonic crystals based on vertical convective self-assembly and atomic layer deposition. The impact of various fabrication steps on the optical properties was used to tailor a technique to produce the highest quality opals and

inverse opals possible. A range of photonic crystal sizes were self-assembled into opal templates that were sintered and infiltrated with ZnO in a custom-built ALD system. The low-temperature ALD process produced a nanocrystalline ZnO coating that becomes polycrystalline after firing. An RIE process was developed that efficiently removed the top surface of the inverse opals. This had a profound impact on the spontaneous emission response of ZnO inverse opals, reducing the defect emission and significantly enhancing the band edge emission.

The optical quality of ZnO inverse opals was characterized by reflectivity and transmission measurements. Angle- and polarization-dependent reflectivity characterized the behavior of the fundamental and higher order pseudogaps. A stationary inflection point in the band structure was found for *s*-polarized light. The spontaneous emission of the ZnO inverse opals was suppressed in the band gap region, and enhanced in the flat higher order bands, especially at the stationary inflection point. RIE-processed opals were infiltrated with a homogeneous distribution of QDs in an attempt to observe similar emission enhancement; however, such an effect remained elusive. A two-step process was developed to embed the QDs into the ZnO portions of the inverse opal, but was restricted by fabrication difficulties.

Gold and silver nanoparticles were successfully infiltrated into ZnO inverse opals. At moderate concentrations it was possible to observe the combined effects of the photonic band structure and plasmonic materials. Silver particles inside the inverse opal were grown into larger particles that exhibited a shifted plasmon resonance based on their size.

Conclusions and Future Work

The work presented in this thesis describes the fabrication of high quality material structures that are used to probe and understand the interactions of light and matter. Copper chloride is a model material for the study of excitons and biexcitons and their luminescent signatures. It is a direct gap semiconductor that is lattice-matched with silicon, providing numerous opportunities for the development of optoelectronic devices. The procedures developed in this work represent straightforward evaporation growth techniques for growing high quality films on several substrates. These films were used to study the nature of excitonic material generation and propagation in this unique system. Novel, non-resonant, two-photon excitation was discovered to exist in bulk CuCl but not in CuCl thin films. Nonlinear optical studies demonstrated that the second harmonic generation process in CuCl is highly dependent on the substrate and film orientation.

Despite its long, rich history there is still great potential for CuCl research. Recent models of interfacial superconductivity in CuCl/Si superlattices show that a method of controlled monolayer single crystal growth is needed to achieve the modeled structures.[27] Substrate-based single crystal growth has been reported and may warrant study as a potential technique for growing CuCl/Si superlattices. Further study of the nature of bipolariton propagation in CuCl films would be facilitated by the fabrication of a grating structure that would allow light to couple directly into the structure. Thus, excitons and biexcitons could be efficiently generated at one grating, propagate in the film and be collected at the other grating.

Zinc oxide inverse opal photonic crystals represent the other end of the spectrum, where structure, rather than material, primarily dictates how the interaction with light proceeds. This work tested and validated a process for fabricating high quality 3D photonic crystals that operate in the visible regime. The optical quality and the angle-dependent properties of the photonic band structure were probed with reflection and photoluminescence measurements. The spontaneous emission from ZnO was found to be either suppressed or enhanced by proximity to different band gaps in the structure. Quantum dots and plasmonically-active metal nanoparticles were successfully infiltrated into the inverse opal structure.

There are many applications for inverse opal photonic crystals, including solar cells, sensors, and high efficiency light sources.

Further research is needed in fabrication and photonic properties of the materials to determine how to effectively enhance light from QDs inside the structure. Detailed modeling of the local density of states would help determine the energy distribution in the structure. Recently, the ALD system described in this work was modified to include a titanium precursor. The higher index contrast of titanium dioxide would help improve the strength of the photonic band gaps, perhaps improving the chances of seeing an enhancement effect. Early experiments with infiltrating TiO_2 into opal templates have shown promise, displaying smoother coatings and stronger band gaps (from reflectivity spectra).

Plasmon-enhanced random lasing has been demonstrated for a suspension of silver nanoparticles in a gain medium (dye).[185] Reduced-threshold random lasing has been observed using ZnO inverse opals as a gain medium.[168] By loading a ZnO inverse opal with silver nanoparticles, a similar reduction may occur, giving a combined plasmonic/photonic enhancement effect. In their smallest size, AgNPs have a plasmon resonance of 410 nm, while the band edge emission from ZnO is near 380 nm. Indium is a potential dopant[186] that currently has a viable ALD precursor material.[187]

This thesis provides a starting point for developing high quality material structures that can interact with light on several levels. Characterization of the optical properties of CuCl thin films and ZnO inverse opal photonic crystals demonstrated the many phenomena and opportunities for both structures. Several new, exciting avenues for research on CuCl and inverse opal photonic crystals have been revealed and it is hoped that this work will inspire further study of these opportunities.

REFERENCES

[1] Tadashi Kawazoe, Kiyoshi Kobayashi, and Motoichi Ohtsu, "Optical nanofountain: A biomimetic device that concentrates optical energy in a nanometric region," Applied Physics Letters **86**, 1031021-1031023 (2005).

[2] M. Hasuo, T. Itoh, and A. Mysyrowicz, "Progress in the Bose-Einstein Condensation of Biexcitons in CuCl," Physical Review Letters **70** (9), 1303-1306 (1993).

[3] A. R. Hutson, "Piezoelectric Hypothesis for Interface Superconductivity in Cucl," Solid State Communications **33** (9), 969-972 (1980).

[4] K. Miyajimaa Y. Kagotania, G. Oohatab, S. Saitoc, M. Ashidaa, K. Edamatsub, T. Itoha, "Two-photon absorption and lasing due to biexciton in CuCl quantum dots," Journal of Luminescence **112**, 113-116 (2005).

[5] S. A. Rinne, F. Garcia-Santamaria, and P. V. Braun, "Embedded cavities and waveguides in three-dimensional silicon photonic crystals," Nature Photonics **2** (1), 52-56 (2008).

[6] C. Lopez, "Materials aspects of photonic crystals," Advanced Materials **15** (20), 1679-1704 (2003).

[7] L. J. Diguna, Q. Shen, J. Kobayashi et al., "High efficiency of CdSe quantum-dot-sensitized TiO2 inverse opal solar cells," Applied Physics Letters **91** (2), - (2007).

[8] H. H. Chen, H. Suzuki, O. Sato et al., "Biosensing capability of gold-nanoparticle-immobilized three-dimensionally ordered macroporous film," Applied Physics a-Materials Science & Processing **81** (6), 1127-1130 (2005).

[9] B. J. Taylor, "Photosensitive Film Formation on Copper," Journal of Photographic Science **22** (6), 305-306 (1974).

[10] S. Nikitine and Ringeiss.J, "Absorption Et Luminescence De Cucl Aux Basses Temperatures," Journal De Physique **26** (4), 171-& (1965).

[11] A. Brune and J. B. Wagner, "The Electrical-Conductivity of Single and Polycrystalline Copper(I) Chloride," Materials Research Bulletin **30** (5), 573-579 (1995).

[12] R. Moussa, L. Salomon, F. de-Fornel et al., "Photonic band gaps in highly ionic medium: CuCl, CuBr, CuI," Infrared Physics and Technology **44**, 27-34 (2003).

[13] L. O'Reilly, O. F. Lucas, P. J. McNally et al., "Room-temperature ultraviolet luminescence from gamma-CuCl grown on near lattice-matched silicon," Journal of Applied Physics **98** (11) (2005).

[14] R. M. Stevenson, R. J. Young, P. Atkinson et al., "A semiconductor source of triggered entangled photon pairs," Nature **439** (7073), 179-182 (2006).

[15] K. K. Bajaj, "Use of excitons in materials characterization of semiconductor system," Materials Science & Engineering R-Reports **34** (2), 59-120 (2001).

[16] B. P. Zhang A. Syouji, and Y. Segawa, J. Kishimoto, H. Ishihara, and K. Cho, "Interchange of the Quantum States of Confined Excitons Caused by Radiative Corrections in CuCl Films," Physical Review Letters **92** (25), 2574011-2574014 (2004).

[17] S. W. Koch, M. Kira, G. Khitrova et al., "Semiconductor excitons in new light," Nature Materials **5** (7), 523-531 (2006).

[18] T. Matsui and J. B. Wagner, "Ionic-Conductivity of Cuprous Chloride Containing Cuprous Sulfide," Journal of the Electrochemical Society **124** (4), 610-614 (1977).

[19] J. Bruce Wagner and Carl Wagner, "Electrical Conductivity Measurements on Cuprous Halides," The Journal of Chemical Physics **26** (6), 1597-1601 (1957).

[20] S. Hull, "Superionics: crystal structures and conduction processes," Reports on Progress in Physics **67** (7), 1233-1314 (2004).

[21] Eliezer Rapoport and Carl W.F.T. Pistorious, "Phase Diagrams of the Cuprous Halides to High Pressure," Physical Review **172** (3), 838-847 (1968).

[22] C. W. Chu, A. P. Rusakov, S. Huang et al., "Anomalies in Cuprous Chloride," Physical Review B **18** (5), 2116-2123 (1978).

[23] E.F. Skelton, A.W. Webb, F.J. Rachford et al., "Investigations of the pressure dependence of structural, chemical, electrical, and magnetic properties of cuprous chloride (CuCl)," Physical Review B **21** (11), 5289-5298 (1980).

[24] V.L. Ginzburg, "About the Nature of Superdiamagnetism in CuCl and CdS," Solid State Communications **39**, 991-992 (1981).

[25] B. L. Mattes, "Possible Interfacial Superconducting Transport in Cucl-Si," Physica C **162**, 554-555 (1989).

[26] B. Batlogg and J. P. Remeika, "Definite Experimental-Evidence against Intrinsic Electron-Hole Superconductivity in Pure Cucl," Physical Review Letters **45** (13), 1126-1129 (1980).

[27] S. H. Rhim, R. Saniz, J. Yu et al., "Interface electronic structure, two-dimensional metallicity, and possible interface superconductivity in CuCl/Si superlattices," Physical Review B **76** (18), - (2007).

[28] A. Gobel, T. Ruf, M. Cardona et al., "Effects of the isotopic composition on the fundamental gap of CuCl," Physical Review B **57** (24), 15183-15190 (1998).

[29] B. Amrani, T. Benmessabih, M. Tahiri et al., "First principles study of structural, elastic, electronic and optical properties of CuCl, CuBr and CuI compounds under hydrostatic pressure," Physica B-Condensed Matter **381** (1-2), 179-186 (2006).

[30] D. C. Haueisen and H. Mahr, "Nonlinear Electronic Dispersion in Cucl," Physical Review Letters **26** (14), 838-& (1971).

[31] Alex Zunger and Marvin L. Cohen, "Electronic structure of CuCl," Physical Review B **20** (3), 1189-1193 (1979).

[32] S. Kono, T. Ishii, T. Sagawa et al., "X-Ray Photoelectron Study of Valence Bands in Cuprous Halides," Physical Review B **8** (2), 795-803 (1973).

[33] A. Goldmann, J. Tejeda, N. J. Shevchik et al., "Density of Valence States of Cucl, Cubr, Cui, and Agi," Physical Review B **10** (10), 4388-4402 (1974).

[34] Anna-Maria Janner, University of Groningen, 1998.

[35] M. Cardona, "Optical Properties of Silver and Cuprous Halides," Physical Review **1** (1), 69-& (1963).

[36] M. Z. Martin, D. K. Shuh, R. S. Williams et al., "Transport-Properties and Infrared-Spectra of Cucl Thin-Films," Journal of Applied Physics **67** (6), 3097-3101 (1990).

[37] N. Peyghambarian, S. W. Koch, and A. Mysyrowicz, *Introduction to Semiconductor Optics*. (Prentice-Hall, Inc., Englewood Cliffs, New Jersey, 1993), p.485.

[38] S.A. Moskalenko and D.W. Snoke, *Bose-Einstein Condensation of Excitons and Biexcitons and Coherent Nonlinear Optics with Excitons*. (Cambridge University Press, Cambridge, UK, 2000), p.415.

[39] C. Klingshirn, *Semiconductor Optics*. (Springer, Heidelberg, Germany, 2005), p.797.

[40] Mysyrowi.A, J. B. Grun, R. Levy et al., "Excitonic Molecule in Cucl," Physics Letters A **A 26** (12), 615-& (1968).

[41] J. I. Jang, M. A. Anderson, J. B. Ketterson et al., "Anomalous Two-Photon Generation of Excitons in CuCl pellets," To be published (2007).

[42] G. D. Gilliland, "Photoluminescence spectroscopy of crystalline semiconductors," Materials Science & Engineering R-Reports **18** (3-6), 99-399 (1997).

[43] A. Goldmann, "Band-Structure and Optical-Properties of Tetrahedrally Coordinated Cu-Halides and Ag-Halides," Physica Status Solidi B-Basic Research **81** (1), 9-47 (1977).

[44] H. Ichida and H. Nishimura M. Nakayama, "Bound-biexciton photoluminescence in CuCl thin films grown by vacuum deposition," Journal of Physics: Condensed Matter **11**, 7653-7662 (1999).

[45] Haitao Zhang, Ph.D., Northwestern University, 2005.

[46] A. Mysyrowicz, J. B. Grun, R. Levy et al., "Excitonic Molecule in Cucl," Physics Letters A **A 26** (12), 615-& (1968).

[47] R. L. Sutherland, *Handbook of Nonlinear Optics*. (Marcel Dekker, Inc., New York, 2003), p.971.

[48] R. W. Boyd, *Nonlinear Optics*. (Academic Press, San Diego, 2003), p.578.

[49] A. M. Janner, H. T. Jonkman, and G. A. Sawatzky, "Second-harmonic generation spectroscopy: A technique for selectively probing excitons," Physical Review B **6308** (8), - (2001).

[50] R. C. Miller, W. A. Nordland, S. C. Abrahams et al., "Nonlinear Optical Properties of Cuprous Halides," Journal of Applied Physics **44** (8), 3700-3702 (1973).

[51] D. Chemla, P. Kupecek, C. Schwartz et al., "Nonlinear Properties of Cuprous Halides," Ieee Journal of Quantum Electronics **QE 7** (3), 126-& (1971).

[52] R. C. Miller, S. C. Abrahams, R. L. Barns et al., "Absolute Signs of Second Harmonic Generation, Electro-Optic, and Piezoelectric Coefficients of Cuc1 and Zns," Solid State Communications **9** (17), 1463-& (1971).

[53] B. F. Levine, "Bond-Charge Calculation of Nonlinear Optical Susceptibilities for Various Crystal-Structures," Physical Review B **7** (6), 2600-2626 (1973).

[54] D. Frohlich and C. Pahlkelerch, "Contribution of Longitudinal Excitons to 2nd-Harmonic Generation in Cucl," Solid State Communications **89** (10), 881-884 (1994).

[55] H. B. Chen, H. P. Xia, C. H. Zhu et al., "Second harmonic generation from electrically polarized CuCl-microcrystallite-doped glass," Materials Letters **50** (5-6), 333-336 (2001).

[56] Akihisa Yanase and Yusaburo Segawa, "Two different in-plane orientations in the growths of cuprous halides on MgO(001)," Surface Science **329**, 219-226 (1995).

[57] K. Edamatsu A. Kawamori, T. Itoh, "Growth of CuCl nanostructures on CaF2(1 1 1) substrates by MBE - their morphology and optical spectra," Journal of Crystal Growth **237-239**, 1615-1619 (2002).

[58] Y. Segawa A. Yanase, "Nucleation and morphology evolution in the epitaxial growth of CuCl on MgO(001) and CaF2(111)," Surface Science **357-358**, 885-890 (1996).

[59] Y. Segawa A. Yanase, "Stranski-Krastanov growth of CuCl on MgO(O01)," Surface Science **367**, L1-L7 (1996).

[60] W. Chen, M. Dumas, S. Ahsan et al., "Epitaxial growth and characterization of CuCl(110)/GaP(110)," Journal of Vacuum Science and Technology A **10** (4), 2071-2176 (1992).

[61] A. Kahn, S. Ahsan, W. Chen et al., "Determinants of Surface Atomic Geometry - the Cucl(110) Test Case," Physical Review Letters **68** (21), 3200-3203 (1992).

[62] G. Natarajan L. O'Reilly, P.J. McNally, D. Cameron, O.F. Lucas, M. Martinez-Rosa, L. Bradley, A. Reader, S. Daniels, "Growth and characterisation of wide-bandgap, I-VII optoelectronic materials on silicon," Journal of Materials Science: Materials in Electronics **16**, 415-419 (2005).

[63] C. T. Lin, E. Schonherr, A. Schmeding et al., "Growth of CuCl single crystals composed of pure isotopes," Journal of Crystal Growth **167** (3-4), 612-615 (1996).

[64] F.O. Lucas, L. O'Reilly, G. Natarajan et al., "Encapsulation of the heteroepitaxial growth of wide band gap γ-CuCl on silicon substrates," Journal of Crystal Growth **287**, 112-117 (2006).

[65] G. R. Olbright and N. Peyghambarian, "Epitaxial-Growth and X-Ray-Diffraction Analysis of Single-Crystal Thin-Films of Cucl," Solid State Communications **58** (6), 337-341 (1986).

[66] L. Gui Q. Guo , N. Wu, "CuCl growth on the reconstructed surface of (0001) haematite," Applied Surface Science **99**, 229-235 (1996).

[67] D.K. Shuh R.S. Williams, Y. Segawa, "Growth and luminescence spectroscopy of a CuCl quantum well structure," Journal of Vacuum Science and Technology A **6** (3), 1950-1952 (1988).

[68] D. K. Shuh, R. M. Charatan, R. S. Daley et al., "Growth and Reactivity of Cucl on Si(111)," Chemistry of Materials **2** (5), 492-494 (1990).

[69] T. Wake, K. Saiki, and A. Koma, "Epitaxial growth and surface structure of cuprous halide thin films," Journal of Vacuum Science & Technology a-Vacuum Surfaces and Films **18** (2), 536-542 (2000).

[70] G. Natarajan, S. Daniels, D. C. Cameron et al., "Growth of CuCl thin films by magnetron sputtering for ultraviolet optoelectronic applications," Journal of Applied Physics **100** (3), - (2006).

[71] B. L. Mattes and C. L. Foiles, "Large Diamagnetism and Paramagnetism Associated with a Cucl-Si Interface," Physica B & C **135** (1-3), 139-147 (1985).

[72] Atsuyoshi Shimamoto Masahiro Hasuo, Takeshi Fujiwara, and Atsushi Iwamae and Takashi Fujimoto Norihiro Okuda, "Free Z_3 Exciton Luminescence Spectra of Vapor-deposited CuCl Films," Journal of the Physical Society of Japan **74** (11), 3077-3081 (2005).

[73] K. Saiki N. Nishida, A. Koma, "Heteroepitaxy of CuCl on GaAs and Si substrates," Surface Science **324**, 149-158 (1995).

[74] Y. Kagotani, K. Miyajima, S. Saito et al., "Temporal behavior of biexciton luminescence under two-photon excitation in CuCl quantum dots," Journal of Luminescence **119**, 33-37 (2006).

[75] Yasuaki Masumoto, Tomohiro Kawamura, and Koh Era, "Biexciton lasing in CuCl quantum dots," Applied Physics Letters **62** (3), 225-227 (1993).

[76] A. Yanase Z.K. Tang, Y. Segawa, N. Matsuura, K. Cho, "Quantization of excitons in CuCl epitaxial thin films: Behavior between a two-dimensional quantum well and the bulk," Physical Review B **52** (4), 2640-2648 (1995).

[77] D. M. Soares, S. Wasle, K. Doblhofer et al., "Quartz crystal microbalance expanded capability for studying CuCl crystal formation on copper surfaces," Chemphyschem **3** (9), 817-+ (2002).

[78] M. Shao Q. Li, G. Yu, J. Wu, F. Lia, Y. Qian, "A solvent-reduction approach to tetrapod-like copper(I) chloride crystallites," Journal of Materials Chemistry **13**, 424-427 (2003).

[79] C. Schwab and A. Goltzene, "Cuprous Halides," Progress in Crystal Growth and Characterization of Materials **5** (3), 233-276 (1982).

[80] N. Nakayama S. Watanabe, T. Ito, "Homogeneous hydrogen-terminated Si(111) surface formed using aqueous HF solution and water," Applied Physics Letters **59** (12), 1458-1460 (1991).

[81] R. S. Becker G. S. Higashi, Y. J. Chabal, A. J. Becker, "Comparison of Si(111) surfaces prepared using aqueous solutions of NH_4F versus HF," Applied Physics Letters **58** (15), 1656-1658 (1991).

[82] W. P. Dow, H. S. Huang, and Z. Lin, "Interactions between brightener and chloride ions on copper electroplating for laser-drilled via-hole filling," Electrochemical and Solid State Letters **6** (9), C134-C136 (2003).

[83] M. Y. Yen, C. W. Chiu, F. R. Chen et al., "Convergent electron beam induced growth of copper nanostructures: Evidence of the importance of a soft template," Langmuir **20** (2), 279-281 (2004).

[84] J Jerphagnon and S. K. Kurtz, "Maker Fringes - a Detailed Comparison of Theory and Experiment for Isotropic and Uniaxial Crystals," Journal of Applied Physics **41** (4), 1667-& (1970).

[85] W. N. Herman and L. M. Hayden, "Maker Fringes Revisited - 2nd-Harmonic Generation from Birefringent or Absorbing Materials," Journal of the Optical Society of America B-Optical Physics **12** (3), 416-427 (1995).

[86] J. Acker, S. Köther, K.M. Lewis et al., "The reactivity in the system CuCl-Si related to the activation of silicon in the Direct Synthesis," Silicon Chemistry **2**, 195-206 (2003).

[87] R.S. Williams D.K. Shuh, Y. Segawa, J. Kusano, Y. Aoyagi, S. Namba, "Line-shape and lifetime studies of exciton luminescence from confined CuCl thin films," Physical Review B **44** (11), 5827-5833 (1991).

[88] E. Hanamura, "Giant 2-Photon Absorption Due to Excitonic Molecule," Solid State Communications **12** (9), 951-953 (1973).

[89] A. L. Ivanov and H. Haug, "Self-Consistent Theory of the Biexciton Optical Nonlinearity," Physical Review B **48** (3), 1490-1504 (1993).

[90] J. I. Jang, J. B. Ketterson, M. A. Anderson et al., "Evidence for two-photon generation of propagating bipolaritons in CuCl," Physical Review B **76** (23), - (2007).

[91] J. I. Jang, M. A. Anderson, J. B. Ketterson et al., "Anomalous two-photon generation of excitons in CuCl pellets," Applied Physics Letters **92** (5), - (2008).

[92] J. I. Jang, J. B. Ketterson, M. A. Anderson et al., "Nonresonant two-photon generation of excitonic matter in a CuCl pellet," Journal of Luminescence **128** (10), 1738-1744 (2008).

[93] G. Wang, G. T. Kiehne, G. K. L. Wong et al., "Large second harmonic response in ZnO thin films," Applied Physics Letters **80** (3), 401-403 (2002).

[94] P. Lodahl, A. F. van Driel, I. S. Nikolaev et al., "Controlling the dynamics of spontaneous emission from quantum dots by photonic crystals," Nature **430** (7000), 654-657 (2004).

[95] A. F. Koenderink, L. Bechger, A. Lagendijk et al., "An experimental study of strongly modified emission in inverse opal photonic crystals," Physica Status Solidi a-Applied Research **197** (3), 648-661 (2003).

[96] M. Barth, R. Schuster, A. Gruber et al., "Imaging single quantum dots in three-dimensional photonic crystals," Physical Review Letters **96** (24), - (2006).

[97] P. D. Garcia, A. Blanco, A. Shavel et al., "Quantum dot thin layers templated on ZnO inverse opals," Advanced Materials **18** (20), 2768-+ (2006).

[98] E. Yablonovitch, "Inhibited Spontaneous Emission in Solid-State Physics and Electronics," Physical Review Letters **58** (20), 2059-2062 (1987).

[99] S. John, "Strong Localization of Photons in Certain Disordered Dielectric Superlattices," Physical Review Letters **58** (23), 2486-2489 (1987).

[100] P. Russell, "Photonic crystal fibers," Science **299** (5605), 358-362 (2003).

[101] E. Yablonovitch, T. J. Gmitter, and K. M. Leung, "Photonic Band-Structure - the Face-Centered-Cubic Case Employing Nonspherical Atoms," Physical Review Letters **67** (17), 2295-2298 (1991).

[102] M. Scharrer, PhD Thesis, Northwestern University, 2007.

[103] K. M. Ho, C. T. Chan, and C. M. Soukoulis, "Existence of a Photonic Gap in Periodic Dielectric Structures," Physical Review Letters **65** (25), 3152-3155 (1990).

[104] J.D. Joannopoulos, *Photonic Crystals: Molding the Flow of Light*, Second ed. (Princeton University Press, Princeton, NJ, 2008).

[105] C. Lopez, "Three-dimensional photonic bandgap materials: semiconductors for light," Journal of Optics a-Pure and Applied Optics **8** (5), R1-R14 (2006).

[106] K. Busch and S. John, "Photonic band gap formation in certain self-organizing systems," Physical Review E **58** (3), 3896-3908 (1998).

[107] A. Chelnokov, K. Wang, S. Rowson et al., "Near-infrared Yablonovite-like photonic crystals by focused-ion-beam etching of macroporous silicon," Applied Physics Letters **77** (19), 2943-2945 (2000).

[108] S. Y. Lin, J. G. Fleming, D. L. Hetherington et al., "A three-dimensional photonic crystal operating at infrared wavelengths," Nature **394** (6690), 251-253 (1998).

[109] E. Ozbay, E. Michel, G. Tuttle et al., "Micromachined Millimeter-Wave Photonic Band-Gap Crystals," Applied Physics Letters **64** (16), 2059-2061 (1994).

[110] J. V. Sanders, "Close-Packed Structures of Spheres of 2 Different Sizes .1. Observations on Natural Opal," Philosophical Magazine a-Physics of Condensed Matter Structure Defects and Mechanical Properties **42** (6), 705-720 (1980).

[111] R. Mayoral, J. Requena, J. S. Moya et al., "3D long-range ordering in an SiO2 submicrometer-sphere sintered superstructure," Advanced Materials **9** (3), 257-& (1997).

[112] S. H. Park, D. Qin, and Y. Xia, "Crystallization of mesoscale particles over large areas," Advanced Materials **10** (13), 1028-+ (1998).

[113] M. Bardosova, P. Hodge, V. Smatko et al., "A new method of forming synthetic opals," Acta Physica Slovaca **54** (4), 409-415 (2004).

[114] P. Jiang, J. F. Bertone, K. S. Hwang et al., "Single-crystal colloidal multilayers of controlled thickness," Chemistry of Materials **11** (8), 2132-2140 (1999).

[115] L. V. Woodcock, "Entropy difference between the face-centred cubic and hexagonal close-packed crystal structures," Nature **385** (6612), 141-143 (1997).

[116] D. J. Norris, E. G. Arlinghaus, L. L. Meng et al., "Opaline photonic crystals: How does self-assembly work?," Advanced Materials **16** (16), 1393-1399 (2004).

[117] Y. G. Ko and D. H. Shin, "Effects of liquid bridge between colloidal spheres and evaporation temperature on fabrication of colloidal multilayers," Journal of Physical Chemistry B **111** (7), 1545-1551 (2007).

[118] R. G. Shimmin, A. J. DiMauro, and P. V. Braun, "Slow vertical deposition of colloidal crystals: A Langmuir-Blodgett process?," Langmuir **22** (15), 6507-6513 (2006).

[119] Z. C. Zhou and X. S. Zhao, "Flow-controlled vertical deposition method for the fabrication of photonic crystals," Langmuir **20** (4), 1524-1526 (2004).

[120] Z. Y. Zheng, X. Z. Liu, Y. H. Luo et al., "Pressure controlled self-assembly of high quality three-dimensional colloidal photonic crystals," Applied Physics Letters **90** (5), - (2007).

[121] M. H. Kim, S. H. Im, and O. O. Park, "Rapid fabrication of two- and three-dimensional colloidal crystal films via confined convective assembly," Advanced Functional Materials **15** (8), 1329-1335 (2005).

[122] L. B. Zhang and Y. Y. Xiong, "Rapid self-assembly of submicrospheres at liquid surface by controlling evaporation and its mechanism," Journal of Colloid and Interface Science **306** (2), 428-432 (2007).

[123] Z. Z. Gu, A. Fujishima, and O. Sato, "Fabrication of high-quality opal films with controllable thickness," Chemistry of Materials **14** (2), 760-765 (2002).

[124] J. S. King, E. Graugnard, and C. J. Summers, "TiO2 inverse opals fabricated using low-temperature atomic layer deposition," Advanced Materials **17** (8), 1010-+ (2005).

[125] M. Scharrer, X. Wu, A. Yamilov et al., "Fabrication of inverted opal ZnO photonic crystals by atomic layer deposition," Applied Physics Letters **86** (15), - (2005).

[126] J. S. King, D. Heineman, E. Graugnard et al., "Atomic layer deposition in porous structures: 3D photonic crystals," Applied Surface Science **244** (1-4), 511-516 (2005).

[127] R. V. Nair and R. Vijaya, "Infiltration of ZnO in polymeric photonic crystal by the sol-gel process," Journal of Physics D-Applied Physics **40** (4), 990-997 (2007).

[128] D. Y. Wang, J. S. Li, C. T. Chan et al., "Optical properties of nanoparticle-based metallodielectric inverse opals," Small **1** (1), 122-130 (2005).

[129] L. K. Teh, K. H. Yeo, and C. C. Wong, "Effective photonic pseudogap of a two-phase composite opaline photonic crystal," Applied Physics B-Lasers and Optics **87** (2), 297-300 (2007).

[130] B. H. Juarez, P. D. Garcia, D. Golmayo et al., "ZnO inverse opals by chemical vapor deposition," Advanced Materials **17** (22), 2761-+ (2005).

[131] R. L. Puurunen, "Surface chemistry of atomic layer deposition: A case study for the trimethylaluminum/water process," Journal of Applied Physics **97** (12), - (2005).

[132] T. Suntola and J. Hyvarinen, "Atomic Layer Epitaxy," Annual Review of Materials Science **15**, 177-195 (1985).

[133] L. Niinisto, J. Paivasaari, J. Niinisto et al., "Advanced electronic and optoelectronic materials by Atomic Layer Deposition: An overview with special emphasis on recent progress in processing of high-k dielectrics and other oxide materials," Physica Status Solidi a-Applied Research **201** (7), 1443-1452 (2004).

[134] M. Leskela and M. Ritala, "Atomic layer deposition (ALD): from precursors to thin film structures," Thin Solid Films **409** (1), 138-146 (2002).

[135] A. W. Ott and R. P. H. Chang, "Atomic layer-controlled growth of transparent conducting ZnO on plastic substrates," Materials Chemistry and Physics **58** (2), 132-138 (1999).

[136] I. M. Povey, M. Bardosova, F. Chalvet et al., "Atomic layer deposition for the fabrication of 3D photonic crystals structures: Growth of Al2O3 and VO2 photonic crystal systems," Surface & Coatings Technology **201** (22-23), 9345-9348 (2007).

[137] J. S. King, D. P. Gaillot, E. Graugnard et al., "Conformally back-filled, non-close-packed inverse-opal photonic crystals," Advanced Materials **18** (8), 1063-+ (2006).

[138] D. Gaillot, T. Yamashita, and C. J. Summers, "Photonic band gaps in highly conformal inverse-opal based photonic crystals," Physical Review B **72** (20), - (2005).

[139] H.A. Atwater, "The Promise of PLASMONICS," Scientific American, 56-63 (2007).

[140] Y. N. Xia and N. J. Halas, "Shape-controlled synthesis and surface plasmonic properties of metallic nanostructures," Mrs Bulletin **30** (5), 338-344 (2005).

[141] Y. Chen, K. Munechika, I. J. L. Plante et al., "Excitation enhancement of CdSe quantum dots by single metal nanoparticles," Applied Physics Letters **93** (5), - (2008).

[142] J. Seidel, S. Grafstrom, and L. Eng, "Stimulated emission of surface plasmons at the interface between a silver film and an optically pumped dye solution," Physical Review Letters **94** (17), - (2005).

[143] I. Niki K. Okamoto, A. Shvartser, Y. Narukawa, T. Mukai, A. Scherer, "Surface-plasmon-enhanced light emitters based on InGaN quantum wells," Nature **3**, 601-605 (2004).

[144] D.J. Griffiths, *Introduction to Quantum Mechanics*. (Pearson Education, Inc., Upper Saddle River, 2005), p.468.

[145] V. Morandi, F. Marabelli, V. Amendola et al., "Colloidal photonic crystals doped with gold nanoparticles: Spectroscopy and optical switching properties," Advanced Functional Materials **17** (15), 2779-2786 (2007).

[146] S. G. Romanov, "Direct and indirect control upon the photonic band gap dispersion in opals coated with gold nanoparticles," Fullerenes Nanotubes and Carbon Nanostructures **13**, 319-329 (2005).

[147] Y. Tan, W. P. Qian, S. H. Ding et al., "Gold-nanoparticle-infiltrated polystyrene inverse opals: A three-dimensional platform for generating combined optical properties," Chemistry of Materials **18** (15), 3385-3389 (2006).

[148] Z. Z. Gu, R. Horie, S. Kubo et al., "Fabrication of a metal-coated three-dimensionally ordered macroporous film and its application as a refractive index sensor," Angewandte Chemie-International Edition **41** (7), 1153-+ (2002).

[149] S. G. Romanov, A. S. Susha, C. M. S. Torres et al., "Surface plasmon resonance in gold nanoparticle infiltrated dielectric opals," Journal of Applied Physics **97** (8), - (2005).

[150] J. H. Lee, Q. Wu, and W. Park, "Fabrication and optical characterizations of gold nanoshell opal," Journal of Materials Research **21** (12), 3215-3221 (2006).

[151] G. J. Ding, G. D. Qian, Z. Y. Wang et al., "Fabrication and properties of multilayer-coated core-shell structural monodisperse spheres and close-packed structure," Materials Letters **60** (28), 3335-3338 (2006).

[152] A. Moroz, "Three-dimensional complete photonic-band-gap structures in the visible," Physical Review Letters **83** (25), 5274-5277 (1999).

[153] Larry Aagesen, Masters Thesis, Northwestern University, 2007.

[154] Q. X. Guo, N. Uesugi, T. Tanaka et al., "Reactive ion etching of zinc oxide using methane and hydrogen," Japanese Journal of Applied Physics Part 1-Regular Papers Brief Communications & Review Papers **45** (11), 8597-8599 (2006).

[155] H. Noh, M. Scharrer, M. A. Anderson et al., "Photoluminescence modification by a high-order photonic band with abnormal dispersion in ZnO inverse opal," Physical Review B **77** (11), - (2008).

[156] R. C. Jin, Y. C. Cao, E. C. Hao et al., "Controlling anisotropic nanoparticle growth through plasmon excitation," Nature **425** (6957), 487-490 (2003).

[157] S. D. Solomon, M. Bahadory, A. V. Jeyarajasingam et al., "Synthesis and Study of Silver Nanoparticles," Journal of Chemical Education **84** (2), 322-325 (2007).

[158] A. D. McFarland, C. L. Haynes, C. A. Mirkin et al., "Color My Nanoworld," Journal of Chemical Education **81** (4), 544A-544B (2004).

[159] D. G. Duff, A. Baiker, and P. P. Edwards, "A New Hydrosol of Gold Clusters .1. Formation and Particle-Size Variation," Langmuir **9** (9), 2301-2309 (1993).

[160] S. J. Oldenburg, R. D. Averitt, S. L. Westcott et al., "Nanoengineering of optical resonances," Chemical Physics Letters **288** (2-4), 243-247 (1998).

[161] R. C. Jin, Y. W. Cao, C. A. Mirkin et al., "Photoinduced conversion of silver nanospheres to nanoprisms," Science **294** (5548), 1901-1903 (2001).

[162] F. Grasset, N. Saito, D. Li et al., "Surface modification of zinc oxide nanoparticles by aminopropyltriethoxysilane," Journal of Alloys and Compounds **360** (1-2), 298-311 (2003).

[163] K. R. Brown and M. J. Natan, "Hydroxylamine seeding of colloidal Au nanoparticles in solution and on surfaces," Langmuir **14** (4), 726-728 (1998).

[164] H. Wang, F. Tam, N. K. Grady et al., "Cu nanoshells: Effects of interband transitions on the nanoparticle plasmon resonance," Journal of Physical Chemistry B **109** (39), 18218-18222 (2005).

[165] J. B. Jackson and N. J. Halas, "Silver nanoshells: Variations in morphologies and optical properties," Journal of Physical Chemistry B **105** (14), 2743-2746 (2001).

[166] M. A. McLachlan, N. P. Johnson, R. De La Rue et al., "Domain size and thickness control of thin film photonic crystals," Journal of Materials Chemistry **15** (3), 369-371 (2005).

[167] L. M. Goldenberg, B. D. Jung, J. Wagner et al., "Preparation of ordered arrays of layer-by-layer modified latex particles," Langmuir **19** (1), 205-207 (2003).

[168] M. Scharrer, A. Yamilov, X. H. Wu et al., "Ultraviolet lasing in high-order bands of three-dimensional ZnO photonic crystals," Applied Physics Letters **88** (20), - (2006).

[169] K. H. Tam, C. K. Cheung, Y. H. Leung et al., "Defects in ZnO nanorods prepared by a hydrothermal method," Journal of Physical Chemistry B **110** (42), 20865-20871 (2006).

[170] Y. Hu and H. J. Chen, "Origin of green luminescence of ZnO powders reacted with carbon black," Journal of Applied Physics **101** (12), - (2007).

[171] A. B. Djurisic and Y. H. Leung, "Optical properties of ZnO nanostructures," Small **2** (8-9), 944-961 (2006).

[172] T. Sasaki, A. Shimizu, T. H. Mourey et al., "Glass transition of small polystyrene spheres in aqueous suspensions," Journal of Chemical Physics **119** (16), 8730-8735 (2003).

[173] C. G. Van de Walle, "Hydrogen as a cause of doping in zinc oxide," Physical Review Letters **85** (5), 1012-1015 (2000).

[174] N. Ohashi, T. Ishigaki, N. Okada et al., "Effect of hydrogen doping on ultraviolet emission spectra of various types of ZnO," Applied Physics Letters **80** (16), 2869-2871 (2002).

[175] J. Yoo, W. I. Park, and G. C. Yi, "Electrical and optical characteristics of hydrogen-plasma treated ZnO nanoneedles," Journal of Vacuum Science & Technology B **23** (5), 1970-1974 (2005).

[176] C. C. Lin, H. P. Chen, H. C. Liao et al., "Enhanced luminescent and electrical properties of hydrogen-plasma ZnO nanorods grown on wafer-scale flexible substrates," Applied Physics Letters **86** (18), - (2005).

[177] J. M. Lim, K. C. Shin, H. W. Kim et al., "Photoluminescence Studies of ZnO thin films grown by atomic layer epitaxy," Journal of Luminescence **109** (3-4), 181-185 (2004).

[178] M. D. McCluskey, S. J. Jokela, and W. M. H. Oo, "Hydrogen in bulk and nanoscale ZnO," Physica B-Condensed Matter **376**, 690-693 (2006).

[179] C. F. Windisch, G. J. Exarhos, C. H. Yao et al., "Raman study of the influence of hydrogen on defects in ZnO," Journal of Applied Physics **101** (12), - (2007).

[180] F. Garcia-Santamaria, E. C. Nelson, and P. V. Braun, "Optical surface resonance may render photonic crystals ineffective," Physical Review B **76** (7), - (2007).

[181] I. S. Nikolaev, P. Lodahl, and W. L. Vos, "Quantitative analysis of directional spontaneous emission spectra from light sources in photonic crystals," Physical Review A **71** (5), - (2005).

[182] J. F. Li, B. H. Jia, G. Y. Zhou et al., "Spectral redistribution in spontaneous emission from quantum-dot-infiltrated 3D woodpile photonic crystals for telecommunications," Advanced Materials **19** (20), 3276-+ (2007).

[183] P. Kristensen, A. F. Koenderink, P. Lodahl et al., "Fractional decay of quantum dots in real photonic crystals," Optics Letters **33** (14), 1557-1559 (2008).

[184] O. P. Khatri, K. Murase, and H. Sugimura, "Structural organization of gold nanoparticles onto the ITO surface and its optical properties as a function of ensemble size," Langmuir **24** (8), 3787-3793 (2008).

[185] G. D. Dice, S. Mujumdar, and A. Y. Elezzabi, "Plasmonically enhanced diffusive and subdiffusive metal nanoparticle-dye random laser," Applied Physics Letters **86** (13), - (2005).

[186] T. Minami, "New n-type transparent conducting oxides," Mrs Bulletin **25** (8), 38-44 (2000).

[187] A. W. Ott, J. M. Johnson, J. W. Klaus et al., "Surface chemistry of In2O3 deposition using In(CH3)(3) and H2O in a binary reaction sequence," Applied Surface Science **112**, 205-215 (1997).